

# **IMPROVED MODELING AND PREDICTION OF SURFACE WAVE AMPLITUDES**

**Jeffry L. Stevens, et al.**

**Leidos  
10260 Campus Point Drive  
San Diego, CA 92121**

**31 May 2017**

**Final Report**

**APPROVED FOR PUBLIC RELEASE; DISTRIBUTION IS UNLIMITED.**



**AIR FORCE RESEARCH LABORATORY  
Space Vehicles Directorate  
3550 Aberdeen Ave SE  
AIR FORCE MATERIEL COMMAND  
KIRTLAND AIR FORCE BASE, NM 87117-5776**

## DTIC COPY

### NOTICE AND SIGNATURE PAGE

Using Government drawings, specifications, or other data included in this document for any purpose other than Government procurement does not in any way obligate the U.S. Government. The fact that the Government formulated or supplied the drawings, specifications, or other data does not license the holder or any other person or corporation; or convey any rights or permission to manufacture, use, or sell any patented invention that may relate to them.

This report was cleared for public release by the RD/RV Communications Office and is available to the general public, including foreign nationals. Copies may be obtained from the Defense Technical Information Center (DTIC) (<http://www.dtic.mil>).

AFRL-RV-PS-TR-2017-0162 HAS BEEN REVIEWED AND IS APPROVED FOR PUBLICATION IN ACCORDANCE WITH ASSIGNED DISTRIBUTION STATEMENT.

//SIGNED//

---

Dr. Frederick Schult  
Program Manager, AFRL/RVBYE

//SIGNED//

---

Dr. Thomas R. Caudill, Acting Chief  
AFRL Battlespace Environment Division

This report is published in the interest of scientific and technical information exchange, and its publication does not constitute the Government's approval or disapproval of its ideas or findings.

REPORT DOCUMENTATION PAGE				Form Approved OMB No. 0704-0188	
Public reporting burden for this collection of information is estimated to average 1 hour per response, including the time for reviewing instructions, searching existing data sources, gathering and maintaining the data needed, and completing and reviewing this collection of information. Send comments regarding this burden estimate or any other aspect of this collection of information, including suggestions for reducing this burden to Department of Defense, Washington Headquarters Services, Directorate for Information Operations and Reports (0704-0188), 1215 Jefferson Davis Highway, Suite 1204, Arlington, VA 22202-4302. Respondents should be aware that notwithstanding any other provision of law, no person shall be subject to any penalty for failing to comply with a collection of information if it does not display a currently valid OMB control number. <b>PLEASE DO NOT RETURN YOUR FORM TO THE ABOVE ADDRESS.</b>					
1. REPORT DATE (DD-MM-YYYY) 31-05-2017		2. REPORT TYPE Final Report		3. DATES COVERED (From - To) 01 May 2014 - 30 Apr 2017	
4. TITLE AND SUBTITLE Improved Modeling and Prediction of Surface Wave Amplitudes				5a. CONTRACT NUMBER FA9453-14-C-0225	
				5b. GRANT NUMBER	
				5c. PROGRAM ELEMENT NUMBER 62601F	
6. AUTHOR(S) Jeffry L. Stevens, Jeffrey W. Given, Thomas W. Thompson, and Michael O'Brien				5d. PROJECT NUMBER 1010	
				5e. TASK NUMBER PPM00016515	
				5f. WORK UNIT NUMBER EF127064	
7. PERFORMING ORGANIZATION NAME(S) AND ADDRESS(ES) Leidos 10260 Campus Point Drive San Diego, CA 92121				8. PERFORMING ORGANIZATION REPORT NUMBER	
9. SPONSORING / MONITORING AGENCY NAME(S) AND ADDRESS(ES) Air Force Research Laboratory Space Vehicles Directorate 3550 Aberdeen Avenue SE Kirtland AFB, NM 87117-5776				10. SPONSOR/MONITOR'S ACRONYM(S) AFRL/RVBYE	
				11. SPONSOR/MONITOR'S REPORT NUMBER(S) AFRL-RV-PS-TR-2017-0162	
12. DISTRIBUTION / AVAILABILITY STATEMENT  Approved for public release; distribution is unlimited. (RDMX-17-14756 dtd 20 Mar 2018)					
13. SUPPLEMENTARY NOTES					
14. ABSTRACT We develop a membrane surface wave code named SurfMembrane for the purpose of predicting surface wave amplitudes in heterogeneous structures. The code models diffraction and scattering in heterogeneous structures and runs orders of magnitude faster than a corresponding 3D finite difference calculation. We compared the membrane calculations with a finite difference calculation for the same complex structure and found good agreement in amplitude variations. SurfMembrane also has the capability to calculate sensitivity kernels. We ran SurfMembrane for 73 earthquakes recorded on the US Array using the CMT solutions for those events to generate the source, and compared the calculations with data. We found that while the membrane calculations produced amplitude variations comparable to those observed, the detailed results are very sensitive to small errors in both the earth model and source radiation pattern. We inverted a large Eurasian data set for Q structure. The Eurasian data set retrieved from IRIS consisted of 59,000 waveforms from 1850 Eurasian and African earthquakes, all with CMT solutions. The data were subjected to an intensive quality control procedure to remove bad or questionable data, deep events and events with inaccurate CMT solutions. The final data set contained 23,148 waveforms from 998 events. There is a band of high attenuation stretching across the Middle East from the Mediterranean Sea to India. Together with this report, we are delivering SurfMembrane 3.0, together with test cases that can be run to ensure the program is working correctly. The program manual, which includes instructions for running the program and descriptions of all file formats, is given in the appendices to this report. We are also delivering the earth structures and derived attenuation coefficients from the Eurasian Q inversion study.					
15. SUBJECT TERMS nuclear explosion monitoring, surface waves, membrane surface waves					
16. SECURITY CLASSIFICATION OF:			17. LIMITATION OF ABSTRACT	18. NUMBER OF PAGES	19a. NAME OF RESPONSIBLE PERSON
a. REPORT Unclassified	b. ABSTRACT Unclassified	c. THIS PAGE Unclassified			Dr. Frederick Schult
			Unlimited	88	19b. TELEPHONE NUMBER (include area code)

This page is intentionally left blank.



## Table of Contents

1. Summary .....	1
2. Introduction.....	2
3. Technical Approach .....	3
3.1 Surface Wave Data Set .....	3
3.2 Measurement of Surface Wave Amplitudes .....	5
3.3 Earth Models .....	5
3.4 Membrane Surface Wave Method .....	6
4. Results and Discussion .....	7
4.1 Implementation of SurfMembrane.....	7
4.2 Test of SurfMembrane on Embedded Tarim Basin Structure .....	8
4.3 Calculation and Evaluation of Membrane Surface Wave Finite Frequency Sensitivity Kernels .....	10
4.3.1 Calculation of sensitivity kernels .....	10
4.3.2 Comparison of sensitivity kernels with ray theory .....	12
4.3.3 Limitations of sensitivity kernels.....	15
4.4 Test of SurfMembrane on KNET Structure.....	19
4.5 SurfMembrane Simulation of US Array Data .....	24
4.6 Inversion of Eurasian Attenuation Data for Q Structure .....	31
4.6.1 Data used in the Q Inversion.....	33
4.6.2 Q Inversion Results.....	34
4.7 Application of SurfMembrane to Eurasian events.....	37
4.7.1 $M_S$ Estimation in Heterogeneous Structures .....	40
4.7.2 Comparison of Data and Model Variability in Eurasia .....	50
5. Conclusions.....	54
References.....	56
Appendix A. SurfMembrane Description and User Manual .....	57
A.1 Input to SurfMembrane.....	58
A.2 SurfMembrane File Formats .....	60
A.2.1 Phase Velocity File (input) cvelfilename. Fortran direct access binary file. ...	60
A.2.2 Output File outfile (output). Fortran direct access binary file.....	61
A.2.3 Station Location File (input) stalocfilename. Ascii file. ....	62
A.2.4 Station Data File (output) stadatafilename. Ascii file.....	63
A.2.5 Initial State File (input) initstatefilename. Fortran direct access binary file...	64
A.2.6 Drive File (input) drivefilename. Ascii file. ....	65
A.2.7 Forcing File (input) forcefilename. Ascii file .....	66
A.2.8 Sensitivity Kernel (output) File Format .....	67
Appendix B. SurfMembrane Code and Data Deliverable .....	68
B.1 Data Deliverable.....	69
B.2 MATLAB Scripts .....	70
B.3 Test Case .....	71
Appendix C. Surface Wave Q Inversion Data Deliverable .....	76
List of Symbols, Abbreviations, and Acronyms .....	77

## List of Figures

Figure 1. Events (triangles) that occurred while the US Array was passing over them and were large enough to have Centroid Moment Tensor (CMT) solutions are shown as solid triangles.....	3
Figure 2. Eurasian and African GSN data used in this project. ....	4
Figure 3. Left: Leidos 1-degree phase velocity model of the Western United States at 10 seconds period. Right: CU ¼-degree phase velocity model of the same area at 10 seconds.....	5
Figure 4. Membrane surface wave calculation from Tanimoto (1990). ....	6
Figure 5. Left: Initial motion from a strike-slip earthquake on a closed square around the source. Right: motion at 170 seconds showing that the radiation pattern is preserved. ....	7
Figure 6. Left: Radiation pattern of event with strike slip and dip slip components using the full Hankel function equations for the source. Right: same using the asymptotic approximation. ....	8
Figure 7. Left: 3D finite difference calculation of vertical velocity from an explosion propagating past a low velocity inclusion (marked with square) modeled after the Tarim Basin (from Stevens et al, 2008). Right: Same calculation with membrane surface wave code for 10 second period. Axes show distance east and north in km.....	9
Figure 8. Left: Sensitivity kernel calculated between the source (black circle) and station (yellow circle) in a uniform structure. ....	13
Figure 9. Comparison of travel times calculated by ray theory and kernel integral across each patch shown on the left. ....	13
Figure 10. Calculations were performed with low velocity perturbations in the 3 regions shown above.....	14
Figure 11. Top left: waveform just before station arrival from the structure with the central perturbation. Top right: same with the offset perturbation. Right: Hilbert transformed cross-correlation waveforms showing travel time differences. ....	14
Figure 12. Waveforms for the 1,2,5,10 and 15% negative perturbation located in a small central area, as shown in (earlier) Figure. Top panel shows the calculated waveforms; the bottom panel shows the waveforms correlated with the unperturbed signal. ....	16
Figure 13. Waveforms for the 1, 2, 5, 10 and 15% negative perturbation located in an area offset from the direct ray path. (Top panel shows the calculated waveforms; the bottom panel shows the waveforms correlated with the unperturbed signal.....	16
Figure 14. Snapshots of wave field for small central area with negative velocity perturbation of 15%. The source is located at x=100 km, y=1200 km. The snapshot is at the arrival time for a receiver at x=1700 km, y=1200 km. ....	17
Figure 15. Snapshots of wavefield for small offset area with negative velocity perturbation of 15%. Snapshot parameters as in Figure 4. ....	17
Figure 16. Homogeneous layered model. Numbers show Vp, Vs and density. Trailing zeros indicate infinite Q. ....	19
Figure 17. Heterogeneous model vertical profile of Vp (left) and Vs (right) at about 42N.....	19
Figure 18. 10 second phase velocity map calculated from KNET earth model. ....	20

Figure 19. 3D finite difference calculation of vertical ground motion from an explosion at Lop Nor .....	20
Figure 20. Membrane surface wave calculated at 120 seconds and 240 seconds using the 10 second phase velocity map.....	20
Figure 21. $\ln(\text{amplification})$ at 10 seconds. Left: FD, Right: membrane. “Amplification” is the ratio of amplitude in the heterogeneous structure to the homogeneous structure. ....	21
Figure 22. $\ln(\text{amplification})$ at 20 seconds. Left:FD, Right: membrane.....	21
Figure 23. Filtered waveforms at a single point for the heterogeneous (top) and homogeneous (bottom) structures, calculated with membrane surface waves (left) and 3D finite difference (right).....	22
Figure 24. Histograms of log amplitude distribution in the finite difference calculation (left), and in the finite difference calculation corrected with the membrane surface wave calculation (see text). ....	23
Figure 25. SurfMembrane calculation of waveforms from the Anza earthquake propagating through the CU (left) and Leidos (right) models. ....	24
Figure 26. Ms station corrections derived from Leidos and WUS structures for all events analyzed that were recorded on US Array stations. Left: 10 seconds; right: 20 seconds. Top: CMT sources. Bottom: Explosion sources. ....	25
Figure 27. Mean and standard deviation of station corrections as a function of range for Leidos structures (top) and WUS structures (bottom). Left: 10s; right: 20s. ....	26
Figure 28. Calculated and observed 20 second surface wave amplitudes for 6 events recorded on the US Array. ....	27
Figure 29. Calculated and observed 10 second surface wave amplitudes for 6 events recorded on the US Array. ....	27
Figure 30. Histogram of 20 second surface wave amplitudes for one event. Left: Uncorrected; Middle: Corrected with CMT derived correction; Right: Corrected with explosion derived correction.....	28
Figure 31. Histogram of 10 second surface wave amplitudes for one event. Left: Uncorrected; Middle: Corrected with CMT derived correction; Right: Corrected with explosion derived correction.....	28
Figure 32. Predicted and observed station magnitudes for event 21. ....	29
Figure 33. Top: amplitudes at 7 stations close to 50 degree azimuth. Bottom: waveforms at station I16A (left) at 850 km and H17A (right) at 942 km band-pass filtered at 10 seconds.....	30
Figure 34. Left: Map showing location of all rays used in the inversion. Right: histogram of path lengths used in the inversion.....	33
Figure 35. Left: Adjustments to moments in the CMT data set. Right: average gamma data over all paths, together with average gamma after moment adjustments and weighting.....	34
Figure 36. Gamma data and inversion results compared with starting model over several distance ranges. Upper left: all data; upper right: 300-2000 km; lower left: 1000-5000 km; lower right: 5000-10000 km. ....	35
Figure 37. Left: Attenuation maps at four frequencies. From top to bottom: 0.02 Hz (50 seconds period), 0.05 Hz (20 seconds), 0.067 Hz (15 seconds), 0.1 Hz (10 seconds). Right: histograms of gamma values for each frequency.....	36
Figure 38. Example phase velocity map for event 20300.....	37

Figure 39. Surface waves from two events at 10 seconds (top) and 20 seconds (bottom) showing strong diffraction, especially for 10 seconds waves crossing oceanic boundaries. ....	38
Figure 40. Log surface wave peak amplitudes at each point for event 20300 at 10 seconds period (left) and 20 seconds (right). ....	39
Figure 41. Log ratio of surface wave amplitudes in heterogeneous to homogeneous structure for the two events shown in Figure 39. Top: 10 seconds. Bottom: 20 seconds. ....	40
Figure 42. Source locations for the 88 surface membrane calculations distributed throughout Eurasia and parts of Africa. ....	41
Figure 43. Left panel: Phase velocity map on a 1-degree grid of longitude and latitude. Right panel: Projection of the map in the left panel to a Northing-Easting (x-y) coordinate system using the local distance/bearing. ....	42
Figure 44. Top panels: Fractional difference in the WUSA and Leidos phase velocity maps at 19, 20, and 21 s periods. Bottom panels: Distribution of differences, which are approximately Gaussian with standard deviation of about 2.6%. ....	42
Figure 45. Left panel: Average fractional difference in the WUSA and Leidos phase velocity maps in the 17-23 s band. Right panel: Example of phase velocity map fractional perturbation that is applied to the Leidos Earth model. ....	43
Figure 46. Examples of three instances of perturbed phase velocity maps at 20-second period. ....	43
Figure 47. Examples of surface wave amplitudes (dB) produced by separate perturbation instances applied to the same nominal phase velocity map. ....	44
Figure 48. Ms uncertainty map generated by calculating the standard deviation of Ms over an ensemble of 25 perturbation instances. ....	44
Figure 49. Ms corrections (bottom) and projected nominal 20-second phase velocity maps (top) for source locations 1-30. ....	45
Figure 50. Ms corrections (bottom) and projected nominal 20-second phase velocity maps (top) for source locations 31-60. ....	46
Figure 51. Ms corrections (bottom) and projected nominal 20-second phase velocity maps (top) for source locations 61-88. ....	47
Figure 52. Map of the gradient of the 20-second phase velocity spanning Eurasia and most of Africa and Australia. ....	48
Figure 53. Blue curve: Root-mean-squared magnitude of the Ms corrections (dB), averaged over all angles and source locations, as a function of range. Green curve: Average uncertainty in the Ms corrections, estimated from the standard deviation of the Ms corrections over an ensemble of 25 trials for each source location. ....	49
Figure 54. Left: Map of 20-s Rayleigh wave phase velocity around a source located in Kyrgyzstan. Right: log of the amplitude ratio of the maximum amplitude of the membrane waves computed for an explosion source and the model shown in (a) to the maximum amplitude of the membrane waves computed for an averaged, uniform model. ....	50
Figure 55. Top Left: smoothed Leidos model centered on a specific event. Top Right: Surface wave amplitude variations in the smoothed model (compare with Figure 54). Right: Difference in amplification between rough and smooth models. ....	51
Figure 56. Log amplitude ratio with numerator the amplitude of an explosion source propagated using the membrane calculation with velocity taken from the Leidos Eurasian	

earth model and the denominator the amplitude of an explosion source propagated on a uniform membrane.....	52
Figure 57. Variation of magnitude measurements relative to their associated network averaged magnitude. ....	53

## **List of Tables**

Table 1. Asian Shield earth model .....	8
Table 2. Tarim Basin earth model .....	8
Table 3. Measured and predicted travel time variations for low velocity perturbations (seconds) .....	15
Table 4. Phase delays for kernel and direct ray test cases.....	18

## 1. Summary

We develop a membrane surface wave code named SurfMembrane for the purpose of predicting surface wave amplitudes in heterogeneous structures. The code models diffraction and scattering in heterogeneous structures and runs orders of magnitude faster than a corresponding 3D finite difference calculation. The main limitation of the membrane calculation is that it is restricted to a narrow frequency band, small enough that the frequency dependence of phase velocity can be ignored. We compared the membrane calculations with a finite difference calculation for the same complex structure and found good agreement in amplitude variations.

We ran SurfMembrane for 73 earthquakes recorded on the US Array using the CMT solutions for those events to generate the source, and compared the calculations with data. We found that while the membrane calculations produced amplitude variations comparable to those observed, the detailed results are very sensitive to small errors in both the earth model and source radiation pattern, so it was not possible to generate predicted amplitude changes sufficiently accurate to correct amplitudes at a specific location.

We added to SurfMembrane the capability to calculate sensitivity kernels which predict variations in travel time as a function of earth structure, and we compared the results from the sensitivity kernels to ray theory predictions. The sensitivity kernels can predict changes due to off-axis structural variations that cannot be modeled by ray theory, however for most cases we found that predictions from ray theory along great circle paths gave more accurate predictions than the sensitivity kernels. This is most likely due to the Born approximation used in calculation of sensitivity kernels, which is only valid for small perturbations.

We inverted a large Eurasian and northern African data set for Q structure. The data set retrieved from IRIS consisted of 59,000 waveforms from 1850 Eurasian and African earthquakes, all with CMT solutions. These were added to the smaller data set used in the Stevens et al (2008) study. Both the new and the old data sets were subjected to an intensive quality control procedure to remove bad or questionable data, deep events and events with inaccurate CMT solutions. The final data set contained 23,148 waveforms from 998 events. Inversion results are similar to the 2008 study and cover a larger region of Eurasia. There is a band of high attenuation stretching across the Middle East from the Mediterranean Sea to India.

We ran SurfMembrane calculations for 88 well-distributed earthquakes from the Eurasian data set and compared the results with data. We find that the SurfMembrane calculations can be used to correct  $M_s$  for diffraction out to distances of about 2000 km, however at greater distances diffraction is too sensitive to small variations in earth structure to allow reliable predictions.

Together with this report, we are delivering SurfMembrane 3.0, together with test cases that can be run to ensure the program is working correctly. The program manual, which includes instructions for running the program and descriptions of all file formats, is given in the appendices to this report. We are also delivering the earth structures and derived attenuation coefficients from the Eurasian Q inversion study.

## 2. Introduction

The objective of this project is to improve modeling and prediction of surface wave amplitudes at short periods (8-20 seconds) for nuclear monitoring purposes. This follows previous projects which developed global surface wave dispersion maps on a one degree grid (Stevens et al, 2005), and inverted surface wave data in Eurasia for attenuation (Stevens et al, 2008). The second project showed that attenuation inversions were strongly affected by amplitude variations caused by earth structure, and so in this project we are implementing and testing a new procedure based on membrane surface waves to correct for structural variations in amplitude, and perform comparisons with both finite difference calculations and data to see if these structural effects can be predicted and removed.

We developed a membrane surface wave code named “SurfMembrane.” As a first test, SurfMembrane calculations were compared with the results of a 3D finite difference calculation corresponding to the complex region between Lop Nor and KNET (Stevens et al, 2008). Phase velocities for several frequencies were derived from the KNET model of velocity and density vs. depth at each point in the 3D grid. SurfMembrane was run for each frequency and compared with results from the 3D calculation filtered in approximately the same frequency band. Amplitude corrections derived from the SurfMembrane calculations significantly improved the consistency of the results. This shows that if the source and structure are well-defined, SurfMembrane can be used to generate structural amplitude corrections.

SurfMembrane was then applied to US Array data and Eurasian surface wave data, using the best available phase velocity models for each and calculating surface waves for events with known CMT solutions. As discussed in the following sections, the SurfMembrane calculations generally predict the magnitude of the expected variability, but there is too much sensitivity to the details of the earth structure to make point by point predictions. For earthquakes, we also find that small errors in radiation pattern derived from CMT solutions cause amplitude variations that dominate over the diffraction effects.

We also use SurfMembrane to calculate sensitivity kernels, which predict the change in travel time as a function of variations in earth structure, including variations on earth structure that do not lie along the great circle path. We perform a detailed comparison of the predictions from the sensitivity kernels with the predictions from ray theory along great circle paths.

We extend the inversion of surface wave attenuation for Q structure that was performed in 2008, adding much more data and extending the range into northern Africa. we retrieved 59,000 waveforms from 1850 Eurasian and African events. We also retrieved the locations, depths and origin times for all of these events from the International Seismological Center (ISC), and replaced the CMT origins and depths with the better ISC origins. These data were then combined with the data set from the 2008 study and put through an aggressive data quality procedure to prune out bad or noisy data, and deep events or data with bad depths or focal mechanisms. This resulted in a high quality data set of 23,148 spectra from 998 events. There were an average of 14.8 spectral data points for each waveform, leading to a total data set of 343,322 data points.

Appendix A is a User Manual for the SurfMembrane code, and Appendix B and C are a description of the code and data delivered together with this report.



### 3. Technical Approach

#### 3.1 Surface Wave Data Set

We assembled two large data sets of surface waves, all from events large enough to have CMT solutions:

1. Areas in the continental United States where most of the source to receiver path is covered by the US Array. There were 73 such events, each recorded by up to 500 US Array stations (Figure 1).

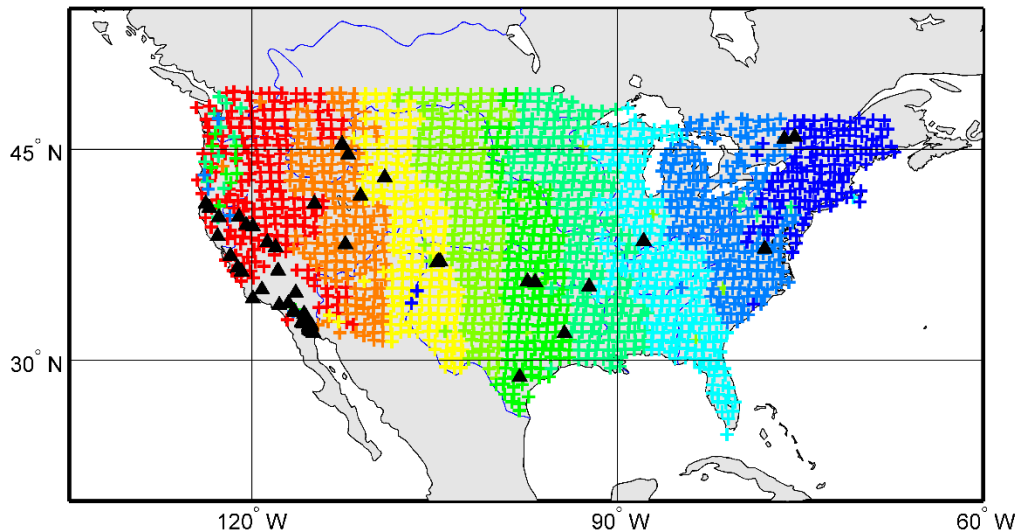


**Figure 1.** Events (triangles) that occurred while the US Array was passing over them and were large enough to have Centroid Moment Tensor (CMT) solutions are shown as solid triangles. *US Array stations are shown as + symbols, colored to show stations that were operating at the same time.*

2. Eurasian and North African earthquakes recorded on GSN stations. We collected 59,000 waveforms from 1850 Eurasian and African events (Figure 2). Measurements made from this data set were added to the data set used in the previous project, and an extensive quality control procedure was applied to the entire data set (see section 4.6).

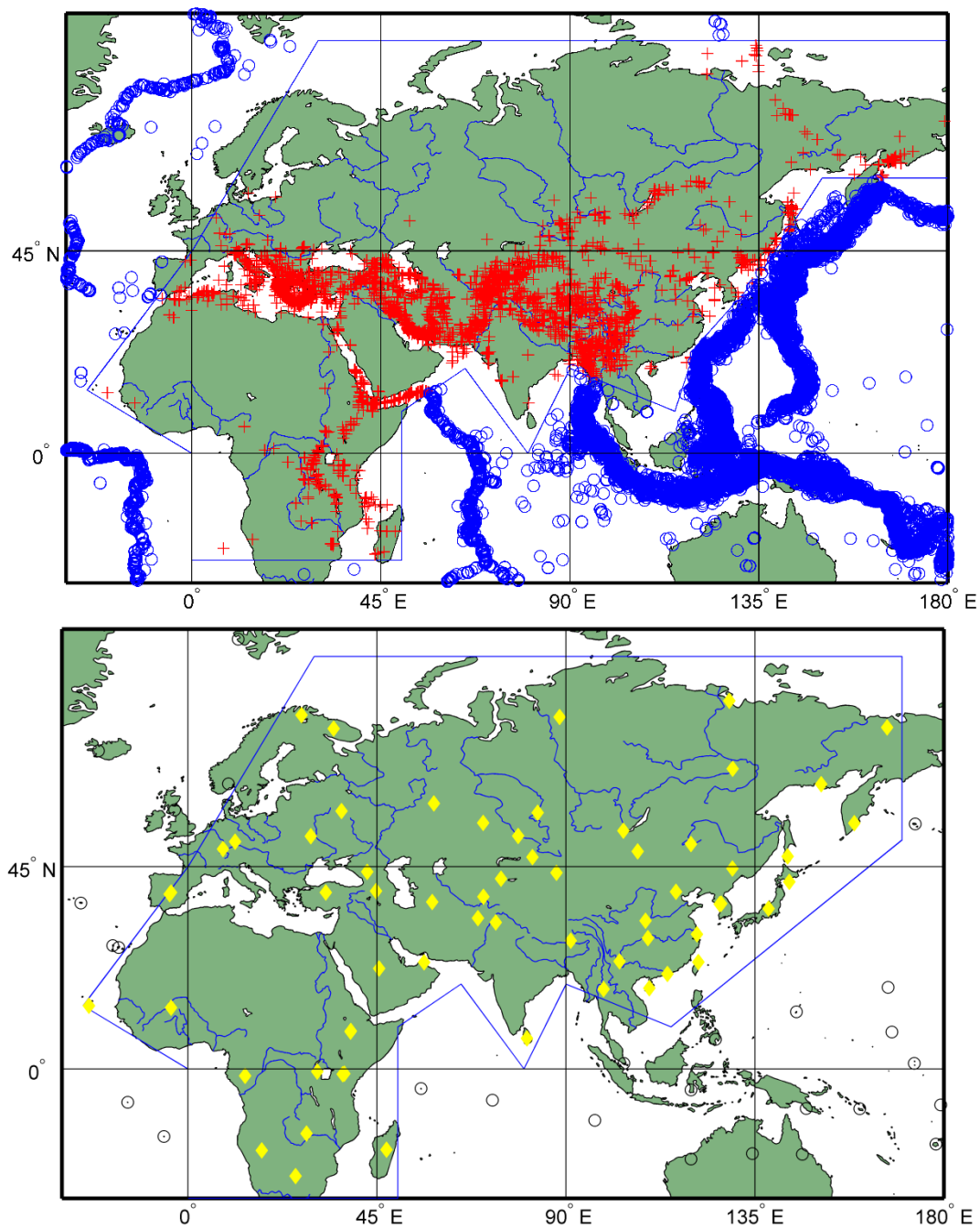


**Figure 2.** Eurasian and African GSN data used in this project. *Top: Red events are in the region of interest with predominately continental paths; blue events are outside the region of interest. Bottom: GSN stations that recorded these events. Yellow stations are within the region of interest.*

### 3.2 Measurement of Surface Wave Amplitudes

All new data for this project was retrieved from the Incorporated Research Institutions for Seismology (IRIS) using the Matlab irisFetch routine. Two types of measurements were made:

1. Data was band-pass filtered with a 3 pole two-pass Butterworth filter over a frequency band of  $f \pm 0.1f$ , for a range of frequencies,  $f$ , corresponding to periods from 8 to 25 seconds. Amplitudes were measured from the peak of the envelope function derived from the Hilbert transform of the waveform. Amplitudes were corrected for instrument response using the instrument responses also retrieved from IRIS.
2. A phase-matched filter was constructed using a synthetic seismogram calculated using the CMT solution and structure and attenuation models from Stevens et al (2008). Phase match filtered seismograms were windowed at  $\pm 100$  seconds, Fourier transformed and corrected for instrument response. Smoothed spectra were then used for Q inversion (section 4.5).

### 3.3 Earth Models

We are using two sets of earth models: 1) Leidos global models developed using surface waves on a 1 degree grid (Stevens et al, 2005); and 2) a higher resolution model (1/4 degree) for the Western United States (WUS) from the University of Colorado developed from ambient noise and earthquake data (Shen et al, 2013). Phase velocity maps at 10 seconds over the Western United States are shown in Figure 3.

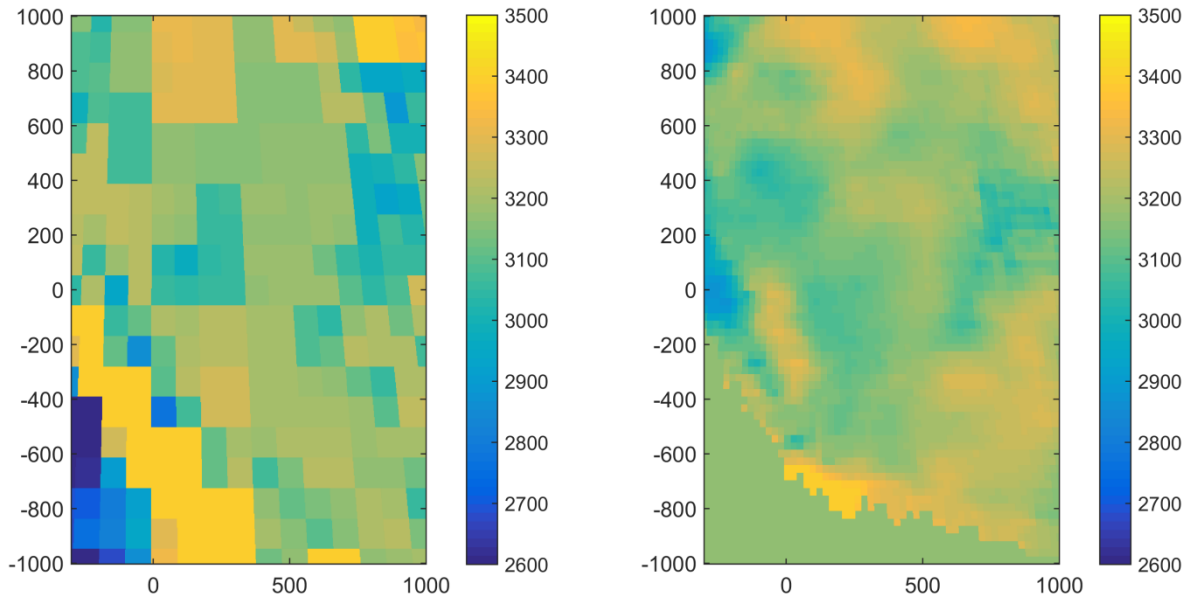


**Figure 3. Left: Leidos 1-degree phase velocity model of the Western United States at 10 seconds period. Right: CU 1/4-degree phase velocity model of the same area at 10 seconds. Distances are in km, phase velocity in m/s. Point (0,0) corresponds to an event near Reno, NV at Lat 39.520, Lon -119.930.**

### 3.4 Membrane Surface Wave Method

The membrane surface wave technique was first developed by Tanimoto (1990), and used to model the complex propagation of surface waves from the Whittier earthquake (Figure 4). The membrane surface wave technique reduces a 3-dimensional elastic problem to a two-dimensional scalar wave problem, with the surface wave modeled as a wave traveling through a surface with variable phase velocity. Since phase-velocity is frequency dependent, the technique is only expected to be valid over a narrow enough frequency band that the phase velocity does not change significantly. The advantages of the membrane surface wave technique are that 1) it is orders of magnitude faster than 3-dimensional finite-difference; and 2) it accurately handles diffraction and scattering along a complex travel path.

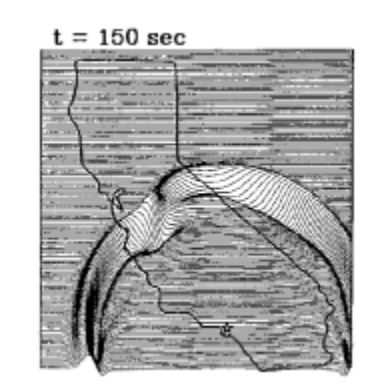


**Figure 4. Membrane surface wave calculation from Tanimoto (1990).**

## 4. Results and Discussion

### 4.1 Implementation of SurfMembrane

We developed a membrane surface wave code named “SurfMembrane” using a finite difference equation solver (Tape, 2003) and absorbing boundaries (Clayton and Engquist, 1977). The membrane surface wave technique can be applied to either a planar or spherical surface. Here, we have applied it to a planar surface. In either case, we need to solve the wave equation:

$$\frac{1}{c^2} \frac{\partial^2 u}{\partial t^2} - \nabla^2 u = f \quad (1)$$

where phase velocity  $c = c(x, y)$ , wave field  $u = u(x, y, t)$ , forcing function  $f = f(x, y, t)$ , and

$\nabla^2 u = \frac{\partial^2 u}{\partial x^2} + \frac{\partial^2 u}{\partial y^2}$  is the Laplacian of  $u$ . The second-order leap-frog finite-difference approximation

of the wave equation given explicitly in Tape (2003) is remarkably simple and straightforward to implement. The Clayton and Enquist (1977) absorbing boundaries do an excellent job of removing any reflected waves from the boundaries.

The wave field can be initiated with either a forcing function, an initial wave field or by specifying the wave field on a closed surface (in the latter case, the wave field is only valid outside the closed surface). Since we want to simulate the motion of a surface wave from an explosion or earthquake, we developed an initialization procedure that accurately reproduces the surface wave by calculating a fundamental mode surface wave in the structure close to the source at a number of points a few km away from and encircling the source point. We then drive the membrane solver with the motion defined at these points, band-pass filtered so that the frequency corresponds closely to the frequency used in the phase velocity map. To model a particular event with a CMT solution, the surface wave is generated from the CMT solution for the event.

An example is shown in Figure 5 for a strike slip earthquake at a depth of 10 km. Surface wave motion was calculated using a modal code at 40 points on a square 20 km across centered on the source and then narrow-band filtered near 10 seconds period. SurfMembrane successfully propagated that motion and preserved the initial radiation pattern.

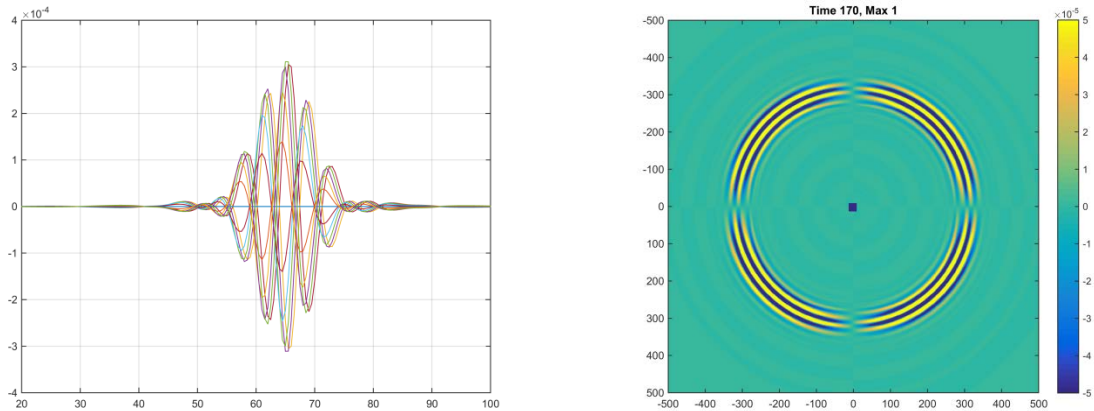


**Figure 5. Left: Initial motion from a strike-slip earthquake on a closed square around the source. Right: motion at 170 seconds showing that the radiation pattern is preserved.**

We found that it is necessary to calculate the exact values of the Hankel functions in generating the surface wave drive functions (See Harkrider et al, 1994, equation 51). Use of the asymptotic form of the Hankel functions, which is common in surface wave codes, introduces an inaccurate source phase that leads to some very odd radiation patterns, particularly when there are both dip-slip and strike-slip components to the source (See Figure 6).

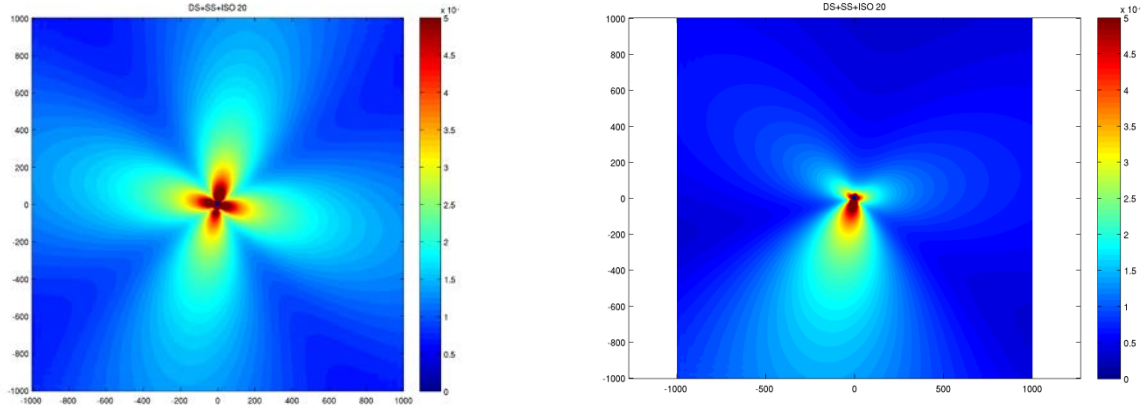


**Figure 6.** Left: Radiation pattern of event with strike slip and dip slip components using the full Hankel function equations for the source. Right: same using the asymptotic approximation. *Both calculations are at 20 seconds.*

## 4.2 Test of SurfMembrane on Embedded Tarim Basin Structure

SurfMembrane was tested by comparison with a 3D finite difference calculation of propagation of explosion-generated wave motion across the Tarim Basin (Stevens et al, 2008). The earth model has a rectangular region with the Tarim Basin structure (Table 2) embedded in a Eurasian Shield structure (Table 1). Both models are derived from the global earth models of Stevens et al (2005).

**Table 1. Asian Shield earth model**

Depth (km)	Vp (km/s)	Vs (km/s)	Density (g/cm <sup>3</sup> )
10.5	6.148	3.451	2.643
20.5	6.224	3.494	2.671
50.0	6.800	3.817	2.881
66.7	8.042	4.514	3.334
83.3	8.042	4.514	3.334
100	8.247	4.629	3.409
∞	8.404	4.717	3.466

**Table 2. Tarim Basin earth model**

Depth (km)	Vp (km/s)	Vs (km/s)	Density (g/cm <sup>3</sup> )
6.5	4.600	2.550	2.480
10.0	5.396	3.029	2.369
20.0	5.496	3.085	2.405
30.0	6.428	3.608	2.745
40.0	6.802	3.818	2.882
50.0	7.349	4.125	3.081
68.7	7.576	4.253	3.164
83.3	8.042	4.514	3.334
100	8.247	4.629	3.409
∞	8.404	4.717	3.466

While the finite difference calculation uses the full 3D structures, the membrane surface wave calculation uses only the phase velocity at a particular period. At 10 seconds period, the phase velocities are 3.264 km/s and 2.688 km/s for the Eurasian and Tarim Basin structures, respectively. A snapshot of the vertical velocity at 240 seconds is shown in Figure 7. The results are very similar, showing strong diffraction around the inclusion in both cases.

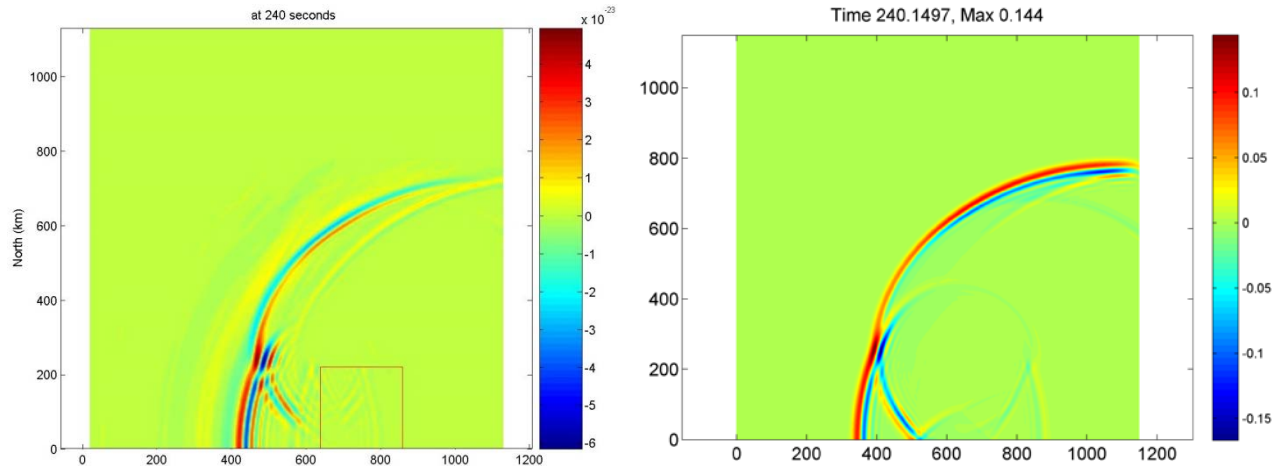


**Figure 7. Left: 3D finite difference calculation of vertical velocity from an explosion propagating past a low velocity inclusion (marked with square) modeled after the Tarim Basin (from Stevens et al, 2008). Right: Same calculation with membrane surface wave code for 10 second period. Axes show distance east and north in km. The explosion source is at North 0, East 1150.**

### 4.3 Calculation and Evaluation of Membrane Surface Wave Finite Frequency Sensitivity Kernels

Finite-frequency sensitivity kernels (e.g. Tromp et al. 2005, Chen et al 2007) give an estimate of the change in an observable, such as arrival time, due to a change in an earth model. A great deal of research has been performed over the past two decades on the construction of such kernels and their use in inversion for 2D and 3D earth structure. In 3D elastic structures, these kernels can be quite expensive and time consuming to calculate, but for membrane surface waves they can be calculated very quickly.

Our interests here are to 1) show how membrane sensitivity kernels can be calculated using the SurfMembrane code, and 2) assess their usefulness relative to traditional ray theory tomography for performing inversions for earth structure. In ray theory tomography, travel times are determined by integrating along a great circle (or modified great circle) path, while in finite-frequency tomography, travel times are determined by integrating over the earth's surface.

#### 4.3.1 Calculation of sensitivity kernels

The derivation below closely follows Peter et al (2007), and also follows Tape et al (2007) and Tromp et al (2005). The membrane surface wave technique solves the wave equation:

$$\frac{1}{c^2} \frac{\partial^2 u}{\partial t^2} - \nabla^2 u = f \quad (2)$$

where phase velocity  $c = c(x, y)$ , wave field  $u = u(x, y, t)$  and forcing function  $f = f(x, y, t)$  and  $\nabla^2 u = \frac{\partial^2 u}{\partial x^2} + \frac{\partial^2 u}{\partial y^2}$  is the Laplacian of  $u$ . The Green's function is defined as the solution to:

$$\left[ \frac{1}{c^2} \frac{\partial^2}{\partial t^2} - \nabla^2 \right] G(\bar{x}, \bar{x}'; t, t') = \delta(\bar{x} - \bar{x}') \delta(t - t') \quad (3)$$

The variation in the waveform  $u$  due to a perturbation in the phase velocity  $c$  is given by:

$$\delta u(\bar{x}, t) = \int_0^t \int_{\Omega} \frac{2}{c^2(\bar{x}')} G(\bar{x}, \bar{x}'; t - t') \frac{\partial^2 u(\bar{x}', t')}{\partial t'^2} \frac{\delta c(\bar{x}')}{c(\bar{x}')} d\bar{x}' dt' \quad (4)$$

The variation in travel time to a receiver at  $\bar{x}_r$  is given by:

$$\delta T = \frac{1}{N_r} \int_0^T w(t) \frac{\partial u(\bar{x}_r, t)}{\partial t} \delta u(\bar{x}_r, t) dt \quad (5)$$

Where  $w(t)$  is a windowing function and the receiver dependent normalization  $N$  is:

$$N_r = \int_0^T w(t) \frac{\partial^2 u(\bar{x}_r, t)}{\partial t^2} u(\bar{x}_r, t) dt \quad (6)$$

Note that  $N_r$  will always be negative. Combining (4) with (5):



$$\delta T = \frac{1}{N_r} \int_0^T w(t) \frac{\partial u(\bar{x}_r, t)}{\partial t} \int_0^t \int_{\Omega} \frac{2}{c^2(\bar{x}')} G(\bar{x}_r, \bar{x}'; t - t') \frac{\partial^2 u(\bar{x}', t')}{\partial t^2} \frac{\delta c(\bar{x}')}{c(\bar{x}')} d\bar{x}' dt' dt \quad (7)$$

which can be written:

$$\delta T = \int_{\Omega} \frac{1}{N_r} \int_0^T \frac{2}{c^2(\bar{x}')} \frac{\partial^2 u(\bar{x}', t')}{\partial t^2} \frac{\delta c(\bar{x}')}{c(\bar{x}')} \int_0^{T-t'} G(\bar{x}', \bar{x}_r; T - t - t') w(T - t') \frac{\partial u(\bar{x}_r, T - t')}{\partial t} d\bar{x}' dt' dt \quad (8)$$

The last integral corresponds to a field generated by a disturbance at the receiver point, so we define this “adjoint field” as:

$$u^{\dagger}(\bar{x}, \bar{x}_r; T - t) = \frac{1}{N_r} \int_0^{T-t} G(\bar{x}, \bar{x}_r; T - t - t') w(T - t') \frac{\partial u(\bar{x}_r, T - t')}{\partial t} dt' \quad (9)$$

Which reduces equation 8 to:

$$\delta T = \int_{\Omega} \int_0^T \frac{2}{c^2(\bar{x}')} \frac{\partial^2 u(\bar{x}', t)}{\partial t^2} \frac{\delta c(\bar{x}')}{c(\bar{x}')} u^{\dagger}(\bar{x}', \bar{x}_r; T - t) d\bar{x}' dt \quad (10)$$

Where  $u^{\dagger}$  is the adjoint field generated by the “adjoint source”:

$$f^{\dagger}(\bar{x}, t) = \frac{1}{N_r} w(T - t) \frac{\partial u(\bar{x}_r, T - t)}{\partial t} \delta(\bar{x} - \bar{x}_r) \quad (11)$$

We define the sensitivity kernel as:

$$K(\bar{x}, \bar{x}_r) = \frac{2}{c^2(\bar{x})} \int_0^T u^{\dagger}(\bar{x}, \bar{x}_r; T - t) \frac{\partial^2 u(\bar{x}, t)}{\partial t^2} dt \quad (12)$$

And so:

$$\delta T = \int_{\Omega} \frac{\delta c(\bar{x})}{c(\bar{x})} K(\bar{x}, \bar{x}_r) d\bar{x} \quad (13)$$

Note that we have chosen the sign convention that  $\delta T = T_{obs} - T_{calc}$  so the time residual is positive for a later than predicted arrival time.

There is one remaining problem: delta functions do not exist in the real world and so we cannot implement equation 11 directly. Instead, we integrate equation 11 over the grid cell containing the receiver with area  $A_r$  and define the alternate quantities (Peter et al. refer to these as “discretized” quantities):

$$\bar{f}^{\dagger}(\bar{x}, t) = \frac{1}{N_r} w(T - t) \frac{\partial u(\bar{x}_r, T - t)}{\partial t} \quad (14)$$

$$\bar{u}^{\dagger}(\bar{x}, \bar{x}_r; T - t) = \frac{A_r}{N_r} \int_0^{T-t} G(\bar{x}, \bar{x}_r; T - t - t') w(T - t') \frac{\partial u(\bar{x}_r, T - t')}{\partial t} dt' \quad (15)$$

Then:

$$K(\bar{x}, \bar{x}_r) = \frac{2}{c^2(\bar{x}) A_r} \int_0^T \bar{u}^\dagger(\bar{x}, \bar{x}_r; T-t) \frac{\partial^2 u(\bar{x}, t)}{\partial t^2} dt \quad (16)$$

A similar analysis from Tape et al (2007) expresses the kernel in terms of spatial gradients:

$$K(\bar{x}, \bar{x}_r) = \frac{-2}{A_r} \int_0^T \nabla \bar{u}^\dagger(\bar{x}, \bar{x}_r; T-t) \nabla u(\bar{x}, t) dt \quad (17)$$

Equations 16 and 17 give identical results.

$\bar{u}^\dagger$  is the quantity calculated by the membrane code in response to the force in equation 14, and the sensitivity kernel is then calculated from equation 16. The adjoint force (14) is derived from the time reversed displacement at the receiver, which is then reversed in time again to calculate the kernel (16).

SurfMembrane has been modified to do this entire calculation. To calculate the kernel using SurfMembrane, run the forward calculation saving the displacement at receiver points, set the flag “kernel\_from\_stadata” and the output file “kernelfilename”. SurfMembrane first runs through the forward calculation and calculates the displacement at receiver points. It then differentiates and normalizes the receiver displacements and reverses the resulting velocity in time (equation 14). It then runs a forward calculation for each receiver point, calculating the displacement field  $\bar{u}^\dagger(x, x_r; t)$ , which is then numerically integrated with the initial acceleration field (read back from the initial calculation and double differentiated) to calculate the kernel using equation 16. Note that the entire field for all times must be saved for the initial source, but it is not necessary to save the calculation for the adjoint source as this is calculated and integrated on the fly.

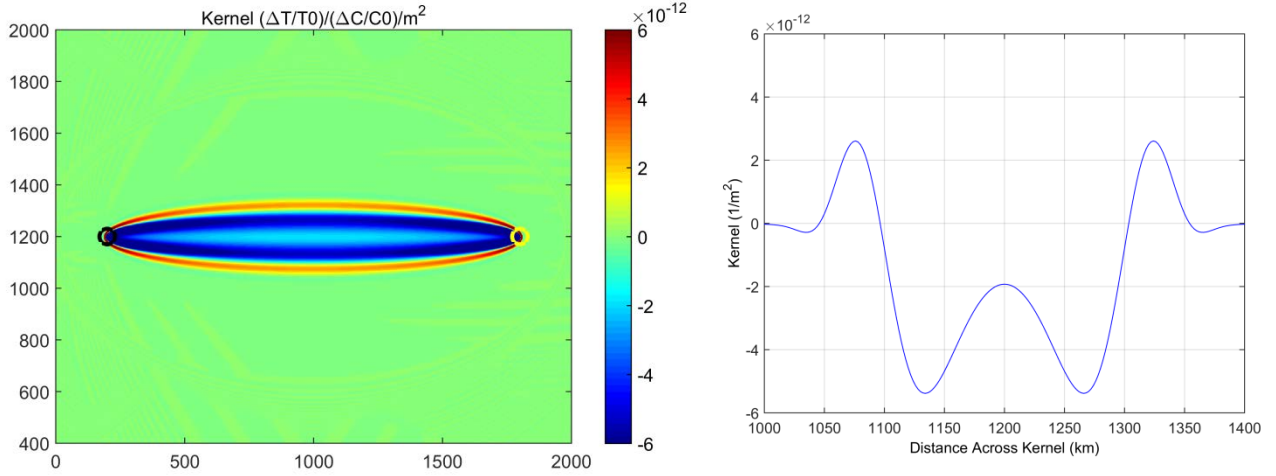
### 4.3.2 Comparison of sensitivity kernels with ray theory

For comparison, ray theory only considers variations in velocity along the ray path between the source and receiver. In that case the variation in travel time (for small perturbations) is given by:

$$\Delta T = -\frac{\Delta r}{c} \frac{\Delta c}{c} \quad (18)$$

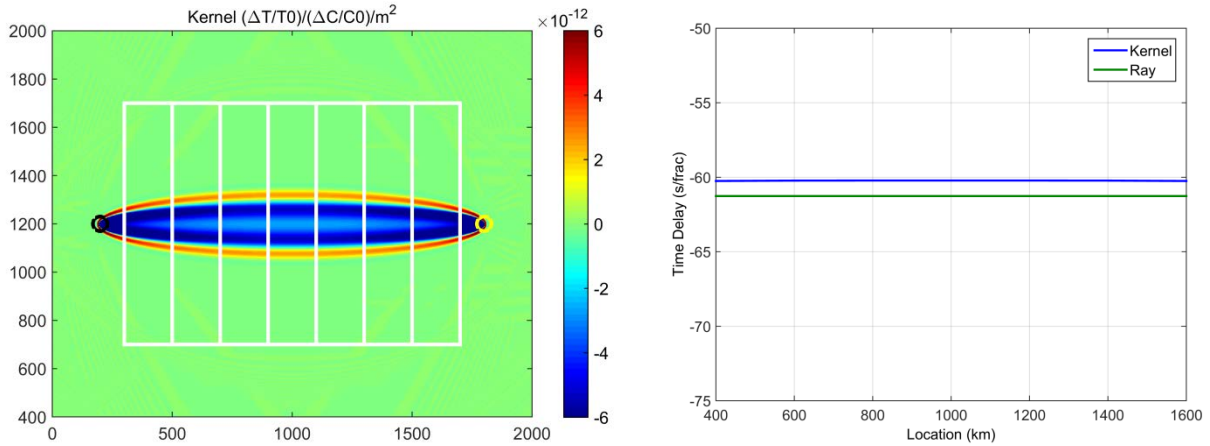
where  $\Delta r$  is the linear distance over which the perturbation occurs and  $\Delta c/c$  is the fractional perturbation in phase velocity. This compares with equation 13, in which the variation in travel time is related to a surface integral with the kernel.

Figure 8 shows the 10 second period sensitivity kernel calculated for a structure with a uniform velocity of 3264 m/s, between a source and receiver separated by 1600 km. Note that although the great circle path between the source and receiver shows an increase in travel time with a decrease in velocity, consistent with ray theory, a perturbation 120 km off axis produces a change of the opposite sign, so a low velocity zone at this location is predicted to cause a decrease in travel time.



**Figure 8.** Left: Sensitivity kernel calculated between the source (black circle) and station (yellow circle) in a uniform structure. *The kernel is calculated at a period of 10 seconds with units of  $m^{-2}$  corresponding to the change in fractional travel time per change in fractional phase velocity per square meter. Grid units are km.* Right: Cross section across the center of the kernel.

To compare with ray theory directly, we calculated the change in travel time for vertical strips across this kernel, calculating equation 13 with the kernel above and equation 18 for ray theory. The strips used and the resulting travel time changes are shown in Figure 9. The results for the kernel area integral and ray line integral are almost identical in this case, except that the ray theory time delay is 1.7% longer.



**Figure 9.** Comparison of travel times calculated by ray theory and kernel integral across each patch shown on the left. *Time delay units are seconds per phase velocity fraction, so a 1% change in phase velocity in a patch results in 1% of the time delay shown above.*

To further check the accuracy of these predictions, we ran three test cases with perturbations at the locations shown in Figure 10. In each case the perturbation was a region with a low velocity of 2688 m/s (-17.6% perturbation). The three cases correspond to 1) a small region along the direct path between the source and receiver; 2) a small region in the area expected to produce a travel time change of the opposite sign from the direct path; and 3) a region completely crossing the kernel.

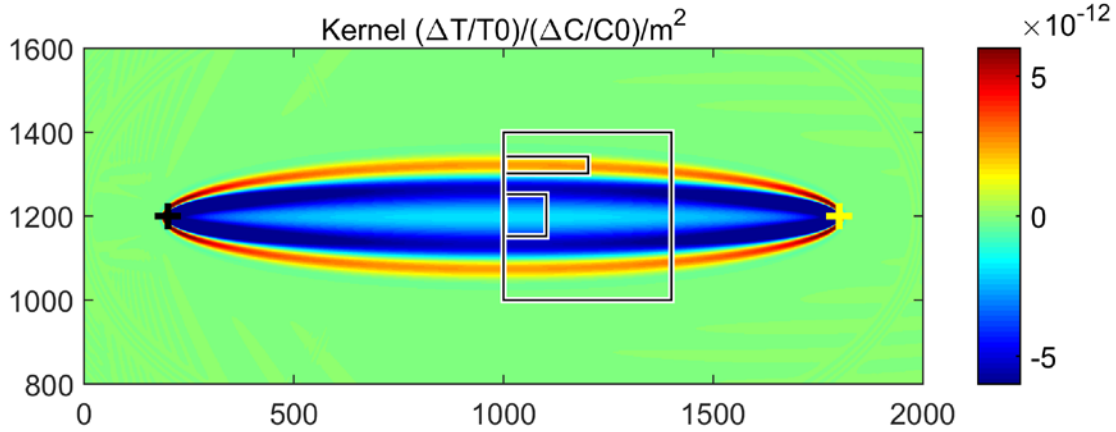


**Figure 10.** Calculations were performed with low velocity perturbations in the 3 regions shown above.

To calculate the change in travel time, the waveforms from the perturbed cases were cross-correlated with the waveform from the uniform structure and then Hilbert transformed to find the peak arrival time (Figure 11). Note that both of these perturbations produce a strong diffracted wave that interferes with the direct wave and produces a secondary arrival. Travel times are derived from the first arrivals.

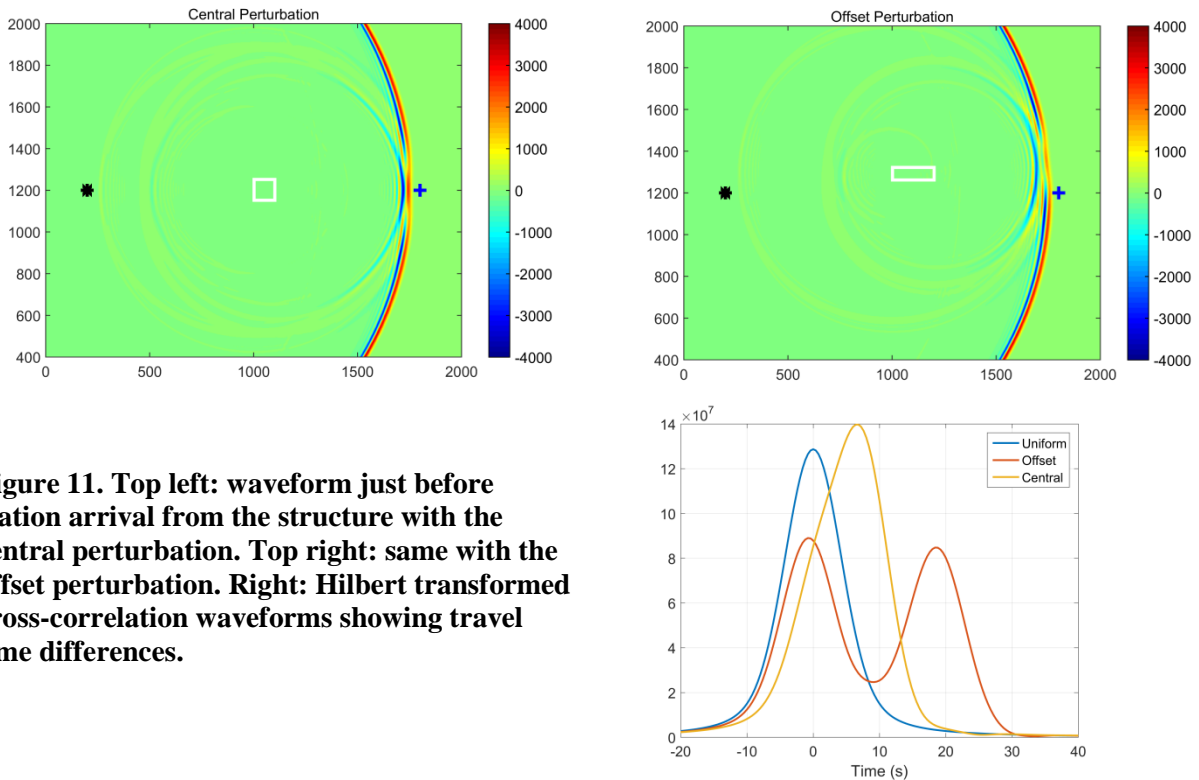


**Figure 11.** Top left: waveform just before station arrival from the structure with the central perturbation. Top right: same with the offset perturbation. Right: Hilbert transformed cross-correlation waveforms showing travel time differences.

Measurements of the travel times from the cross-correlated waveforms shown in Figure 11 are compared with the predictions from ray theory and from using the kernel above for the three cases in Table 3. The offset perturbation does cause a decrease in arrival time as predicted by the kernel, although the predicted decrease is larger than measured. For the central and large perturbations,

ray theory is considerably more accurate than the kernel integral. This is probably because the Born approximation used in equation 4 is valid only for small perturbations, and the velocity change here is large enough that it may exceed the range of validity. Note that for ray theory in Table 3 we have used the exact relation for travel time:  $\Delta T = r/c - r/c_0$  instead of the approximate equation 18, which gives 21.6 seconds, a result more similar to the kernel for the large case.

**Table 3. Measured and predicted travel time variations for low velocity perturbations (seconds)**

<b>Perturbation</b>	<b>Measured</b>	<b>Ray Theory</b>	<b>Kernel</b>
<b>Central</b>	6.63	6.56	2.72
<b>Offset</b>	-0.68	0	-1.25
<b>Large</b>	27.0	26.26	20.26

### 4.3.3 Limitations of sensitivity kernels

We investigate the extent to which the phase delay is linearly related to perturbation in phase velocity through the sensitivity kernels calculated using the membrane model. We ran three test cases with perturbations at the locations shown in Figure 10. In each case, we computed the propagation for velocity perturbations of -1, -2, -5, -10, and -15% in a background phase velocity of 3200 m/s. (i.e. low velocity regions of 3168, 3136, 3040, 2880, and 2720 m/s). The location of the perturbation in the three cases correspond to 1) a small region along the direct path between the source and receiver; 2) a small region in the “first Fresnel zone” predicted by the kernel to produce a phase advance from the direct path; and 3) a region completely crossing the kernel through the 1<sup>st</sup> Fresnel zone.

Waveforms for the small central perturbation are shown in Figure 12. As expected, the phase delay increases with the increasingly negative velocity perturbation. Waveforms for the offset perturbation are in the following Figure 13. The phase differences in this second case are subtle, but the modeling results in a waveform that has the predicted phase advance for a negative velocity perturbation. Figure 14 and Figure 15 show snapshots of the wave-field at the time of arrival at the station for the membrane model with the 15% negative velocity perturbation centered and offset. In both cases a diffracted waveform is apparent. It is the interference of the diffracted wave and the direct wave that results in the phase advance and delay.

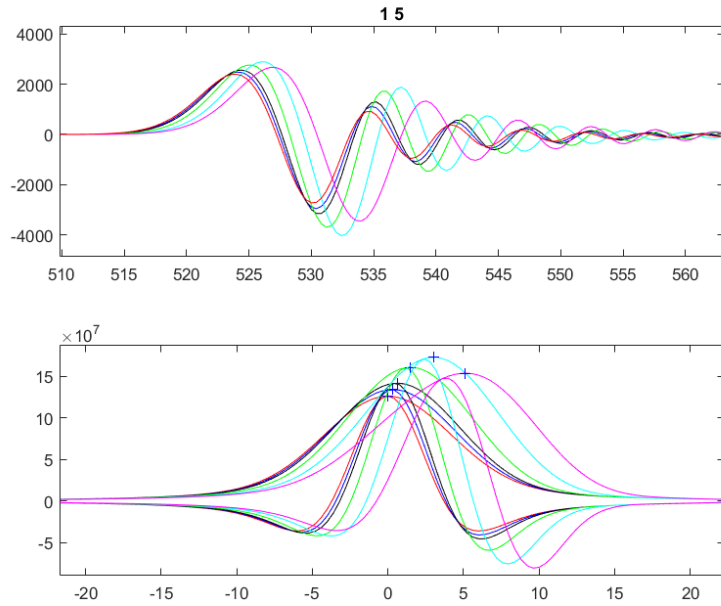


**Figure 12.** Waveforms for the 1,2,5,10 and 15% negative perturbation located in a small central area, as shown in (earlier) Figure. Top panel shows the calculated waveforms; the bottom panel shows the waveforms correlated with the unperturbed signal. *A consistent phase delay is introduced for each of the perturbation cases, along with a signal distortion.*

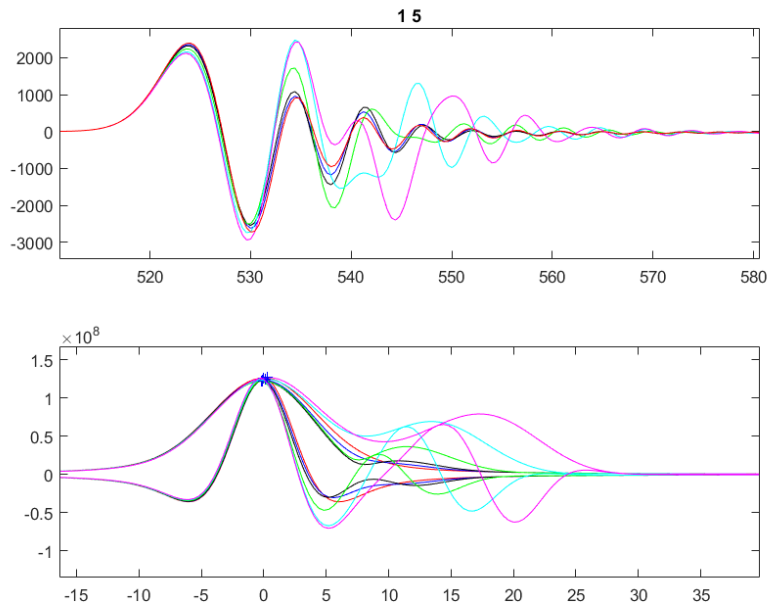


**Figure 13.** Waveforms for the 1, 2, 5, 10 and 15% negative perturbation located in an area offset from the direct ray path. Top panel shows the calculated waveforms; the bottom panel shows the waveforms correlated with the unperturbed signal. *This time, a phase advance appears for the perturbation cases, 1, 2, and 5%, along with an increasing signal distortion caused by diffraction.*

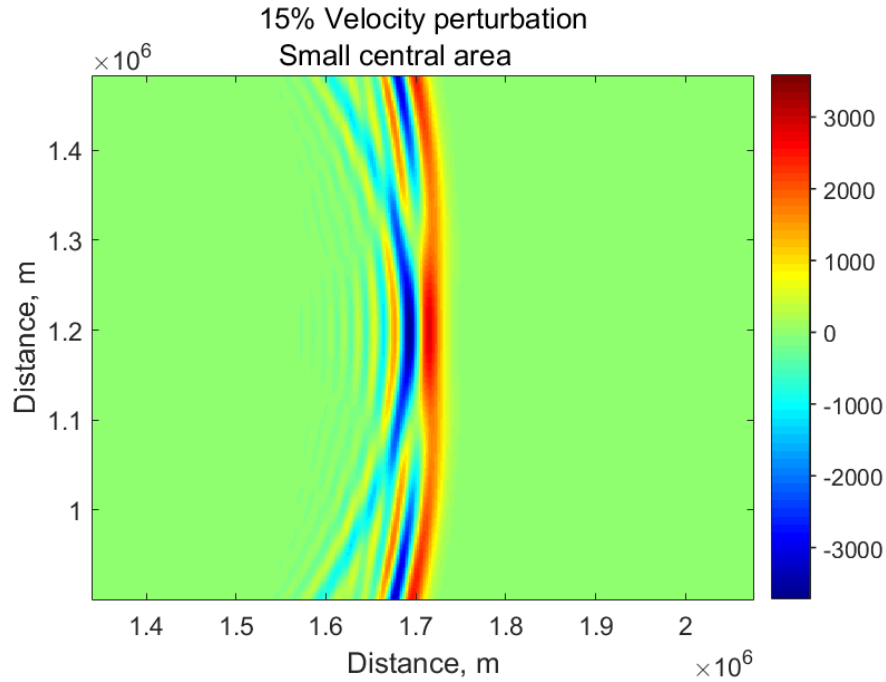


**Figure 14. Snapshots of wave field for small central area with negative velocity perturbation of 15%. The source is located at  $x=100$  km,  $y=1200$  km. The snapshot is at the arrival time for a receiver at  $x=1700$  km,  $y=1200$  km**

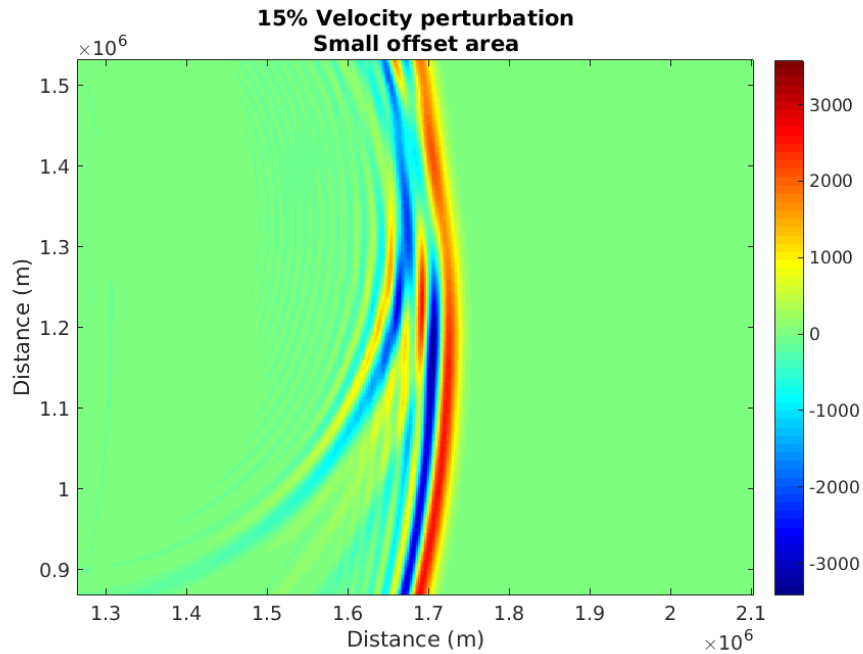


**Figure 15. Snapshots of wavefield for small offset area with negative velocity perturbation of 15%. Snapshot parameters as in Figure 4.**

The phase delays for the various cases are presented in the following Table 4. For the central perturbations, ray theory and the model agree for small perturbations, with the model calculation showing increasingly faster at the larger perturbations. This agrees with the idea that the

narrowband membrane waves are seeing an average velocity over a broad region outside that of the perturbation.

For the offset perturbation, the kernel predicted phase advance for a negative velocity perturbation is roughly of the correct size for the smallest perturbations. However for larger perturbations, the predicted phase advance does not agree well with the measured phase arrival times.

**Table 4. Phase delays for kernel and direct ray test cases.**

Perturbation	1%	2%	5%	10%	15%
Area					
Small Central Model	0.320	0.625	1.500	3.024	5.122
Small Central Kernel	0.1898	0.380	0.949	1.898	2.847
Small Central; Direct ray	0.316	0.638	1.645	3.472	5.515
Offset Model	-0.094	-0.132	-0.060	0.173	0.324
Offset Kernel	-0.0798	-0.160	-0.399	-0.798	-1.197
Large Central Model	1.318	2.665	6.878	14.4	22.4
Large Central Kernel	1.226	2.445	6.113	12.26	18.339
Large Central Ray	1.2626	2.551	6.579	13.889	22.059

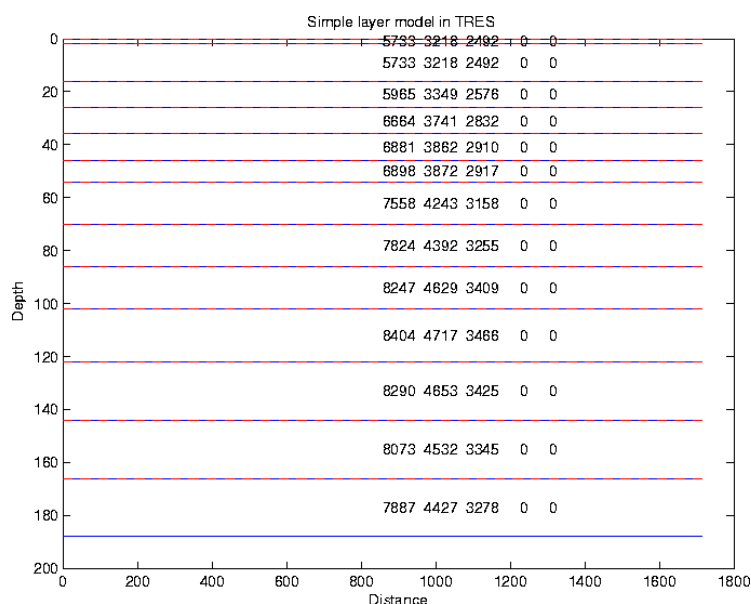


#### 4.4 Test of SurfMembrane on KNET Structure

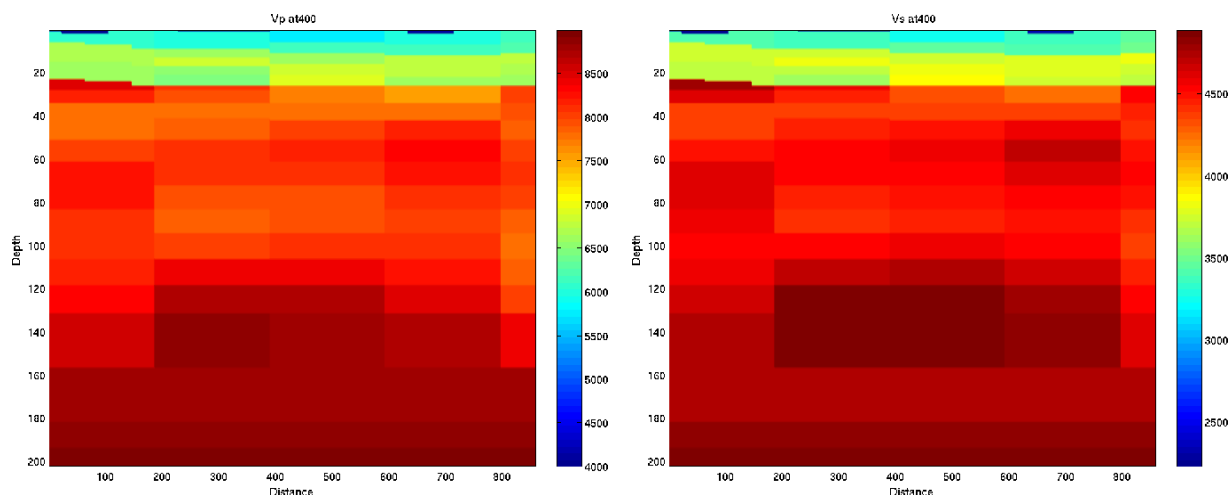
Stevens et al (2008) performed a 3D calculation of propagation of seismic waves from Lop Nor to KNET, and used this for comparison with a Born approximation of surface waves passing through the same structure. We now do the same comparison using membrane surface waves.

We used the 3D elastic finite difference code TRES3D to calculate wave propagation in an earth model corresponding to the region between Lop Nor and KNET. The numerical grid size is 678 (North) X 858 (East) X 202 (Depth) covering an area of approximately (36-48N) and (71.5-92.5E). The grid spacing in each dimension is 2km and time step is 0.12s.

The heterogeneous grid model is generated from the 1° x 1° global model of Stevens et al. (2005) and the homogeneous model is obtained at the LopNor (41.55N,88.70E) source site. No attenuation is included in the numerical calculations. The homogenous model is shown in Figure 16 and a slice through the heterogeneous model is shown in Figure 17.

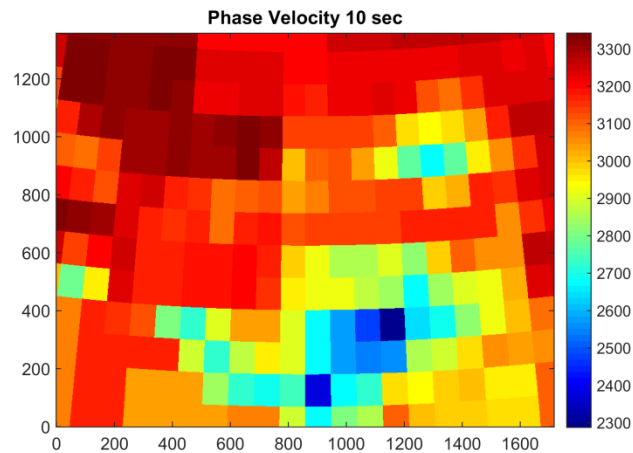


**Figure 16. Homogeneous layered model. Numbers show Vp, Vs and density. Trailing zeros indicate infinite Q.**

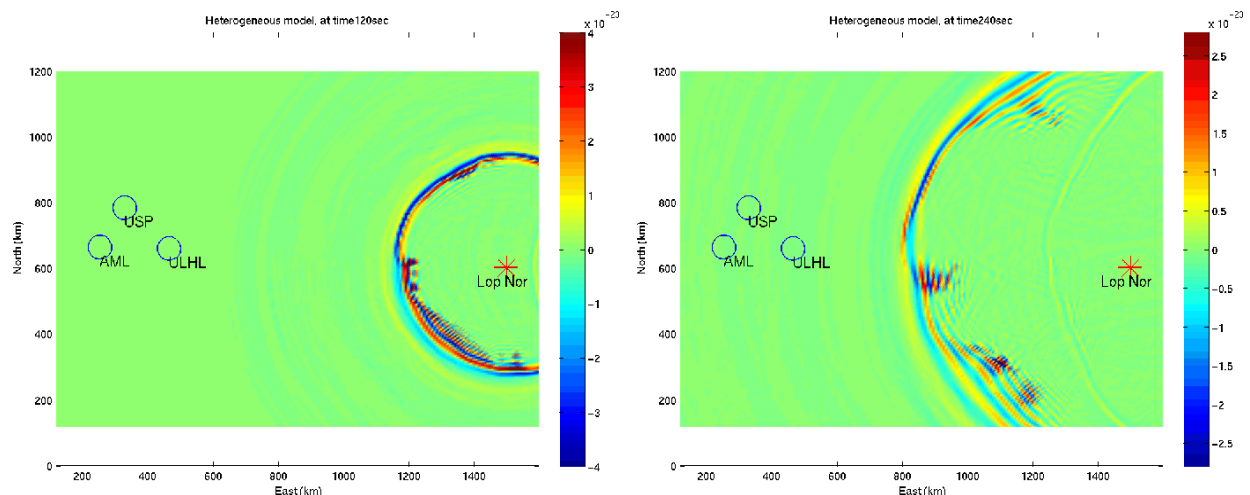


**Figure 17. Heterogeneous model vertical profile of Vp (left) and Vs (right) at about 42N.**

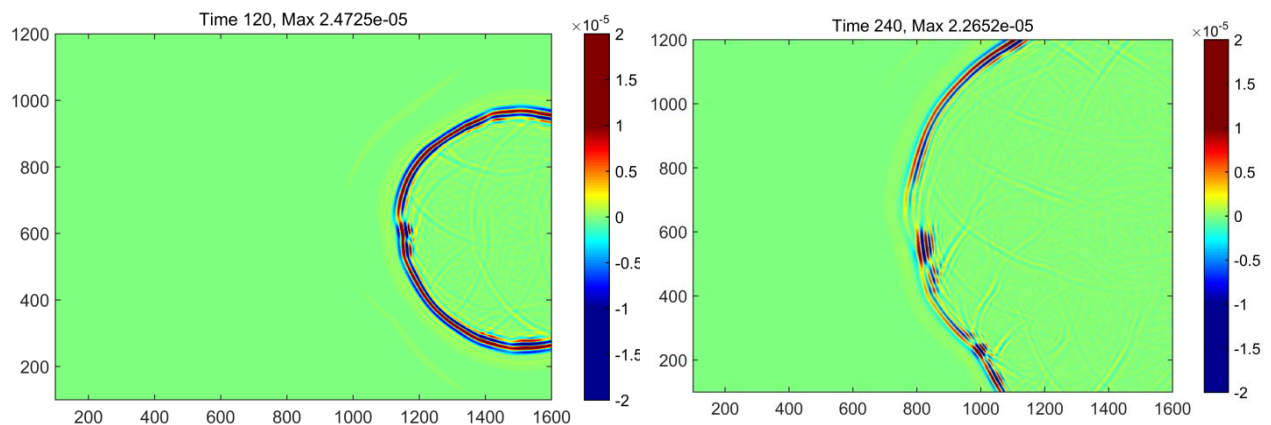
Figure 18 shows the 10 second phase velocity map calculated from this model. Figure 19 shows the vertical ground motion calculated at two times from the finite difference calculation, and Figure 20 shows the 10 second membrane surface wave calculation at the same times.



**Figure 18. 10 second phase velocity map calculated from KNET earth model.**

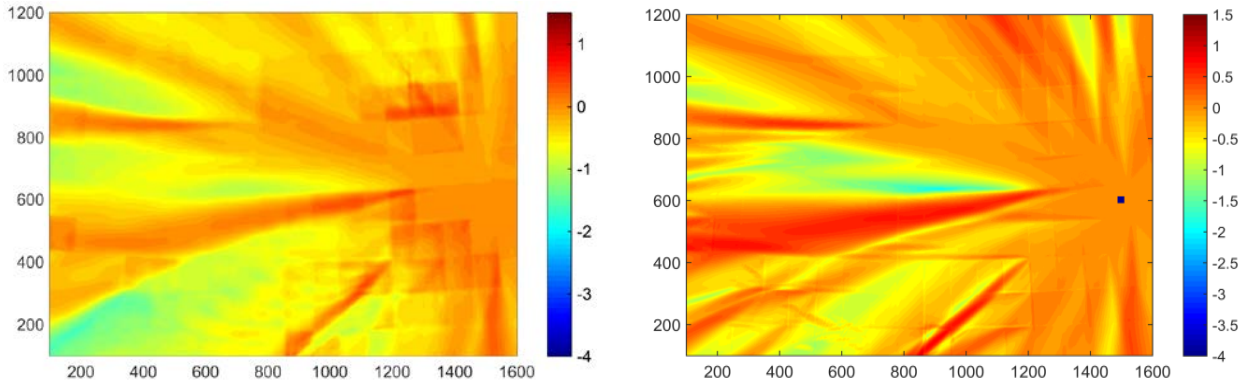


**Figure 19. 3D finite difference calculation of vertical ground motion from an explosion at Lop Nor.**

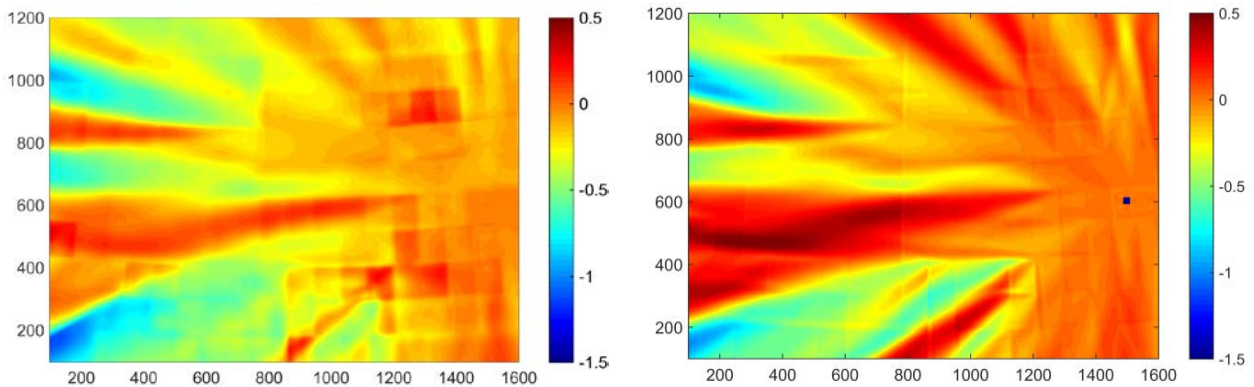


**Figure 20. Membrane surface wave calculated at 120 seconds and 240 seconds using the 10 second phase velocity map.**

Figure 21 and Figure 22 show the amplification at 10 and 20 seconds of the maximum amplitude at each point in the complex structure relative to the maximum amplitude in a uniform structure. The finite difference and membrane surface wave calculations give very similar results, both showing strong diffraction by heterogeneous structures. They are not identical, however, since the membrane surface wave calculation is limited to 10 seconds period while the finite difference calculation is broadband. Because the variations are due to diffraction, small differences in frequency band can change the diffraction patterns substantially. Our main interest is in assessing whether membrane surface waves provide a practical technique for calculating amplitude variations in heterogeneous structure, so we look at that question in more detail.

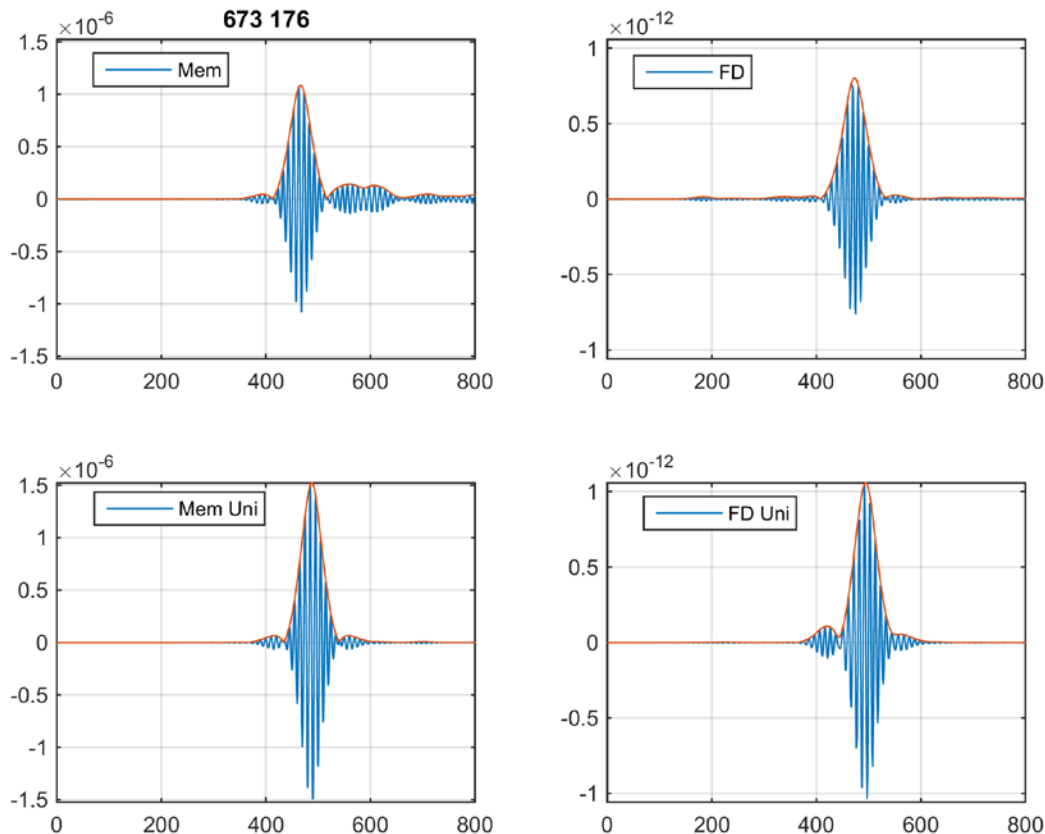


**Figure 21.  $\ln(\text{amplification})$  at 10 seconds. Left: FD, Right: membrane. “Amplification” is the ratio of amplitude in the heterogeneous structure to the homogeneous structure.**



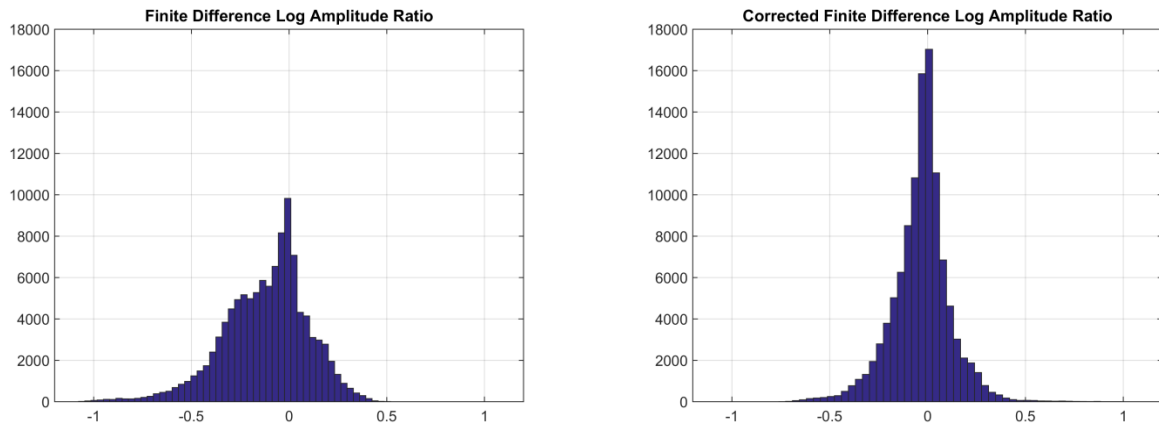
**Figure 22.  $\ln(\text{amplification})$  at 20 seconds. Left:FD, Right: membrane.**

We calculated the ratio of the maximum amplitude of the waves in heterogeneous to homogeneous structure, band-pass filtering close to 10 seconds period (0.09 to 0.11 Hz) for all points in the calculation. An example of the filtered waveforms is shown in Figure 23. We want to assess how well the membrane surface wave calculations can be used to correct amplitude variations from a 3D structure. That is, we would like to be able to calculate the amplification using SurfMembrane to generate an amplitude correction at each point that can be subtracted from the data (in this case the 3D calculation) to produce the amplitudes for the same event in a homogeneous structure.



**Figure 23. Filtered waveforms at a single point for the heterogeneous (top) and homogeneous (bottom) structures, calculated with membrane surface waves (left) and 3D finite difference (right). Both show a similar amplitude reduction in the complex structure.**

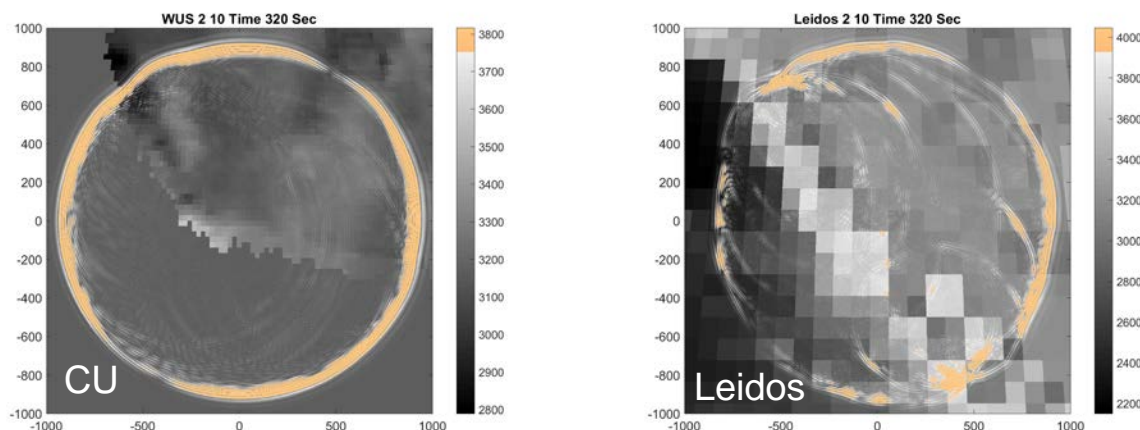
We used the membrane surface wave calculation to “correct” the heterogeneous finite difference calculation. For each point we calculated the ratio of the heterogeneous to homogeneous membrane surface wave calculation, and divided the heterogeneous finite difference ratio by this value. If the correction were perfect and the variation generated by SurfMembrane exactly equaled the variation in the 3D finite difference calculation, then this ratio would be one at every point. The results displayed as a histogram are shown in Figure 24. While not every point is improved, the amplitude distribution is substantially narrowed, and the correction appears to be particularly effective for low amplitudes, which are largely removed in the corrected data set. The standard deviation in the amplitude ratios is reduced from 0.22 to 0.15. This could probably be improved by varying the filter parameters, and this shows that if the earth structure is known well enough, the membrane calculation can be used to correct surface wave amplitudes.



**Figure 24. Histograms of log amplitude distribution in the finite difference calculation (left), and in the finite difference calculation corrected with the membrane surface wave calculation (see text). *The spread is substantially reduced, and low amplitudes in particular are greatly improved.***

## 4.5 SurfMembrane Simulation of US Array Data

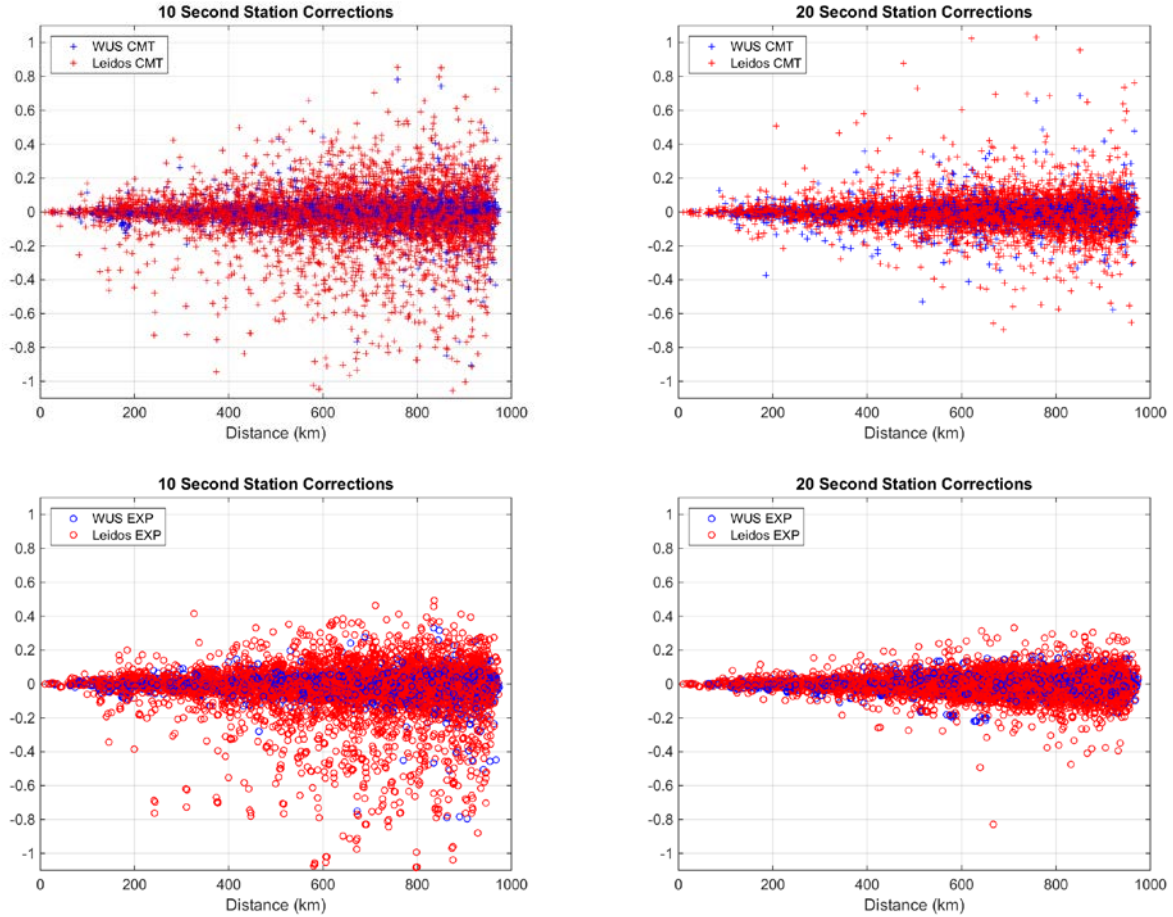
SurfMembrane was run for all 73 events recorded by the US Array discussed earlier. All were run with the Leidos models, and events in the western US were also run with the CU models. An example is shown in Figure 25 for the 2005/06/12 M 5.2 Anza earthquake, for 10 second period waves. Both calculations show effects of diffraction during propagation. The CU model does not include the ocean, so the effects of reflection and scattering from the Ocean/continent boundary are seen only in the Leidos model.



**Figure 25. SurfMembrane calculation of waveforms from the Anza earthquake propagating through the CU (left) and Leidos (right) models.**

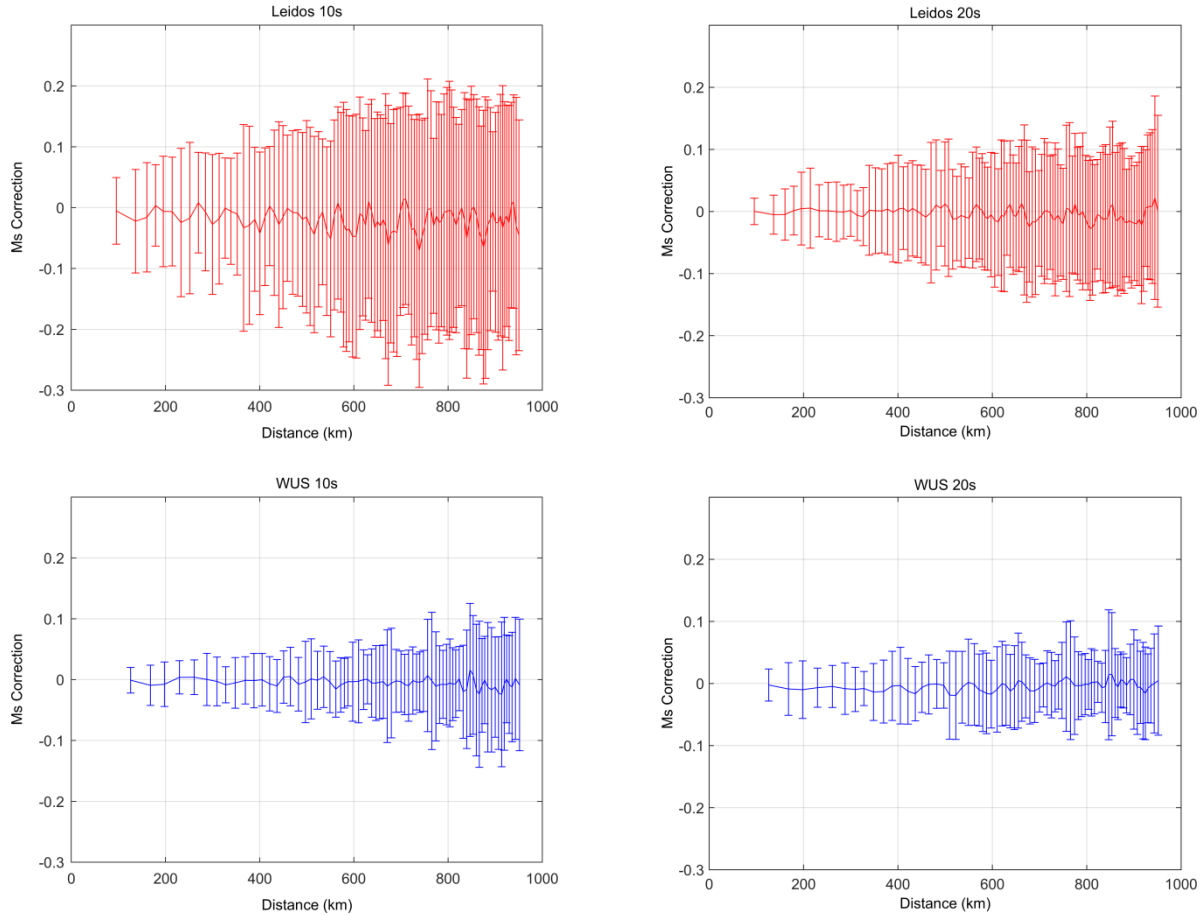
Path dependent station corrections were derived for all events described in section 3 that were recorded on US Array stations. The purpose of the station corrections is to remove the effects of the heterogeneous structure so that the amplitudes correspond to a common uniform structure. Station corrections were derived using two different sets of sources. In both cases, the approach was to run SurfMembrane for the heterogeneous structure and a homogeneous structure, and then subtract the logarithm of the homogenous amplitude from the logarithm of the heterogeneous amplitude. This gives a station residual for the effect of heterogeneity that can be used as a station correction. The first set of sources corresponded to the known CMT solutions for each source. The second set used point explosion sources at 0.5 km depth. Although the CMT sources should more accurately reproduce the observed signals from each event, they have two disadvantages: 1) in the general case when we want to apply station corrections, in most cases we will not have a CMT solution; and 2) station corrections may be anomalously large or small near nodes. The station corrections for all paths are shown in Figure 26.





**Figure 26.** Ms station corrections derived from Leidos and WUS structures for all events analyzed that were recorded on US Array stations. Left: 10 seconds; right: 20 seconds. Top: CMT sources. Bottom: Explosion sources. *Variation is larger for CMT sources because differences are amplified near nodes.*

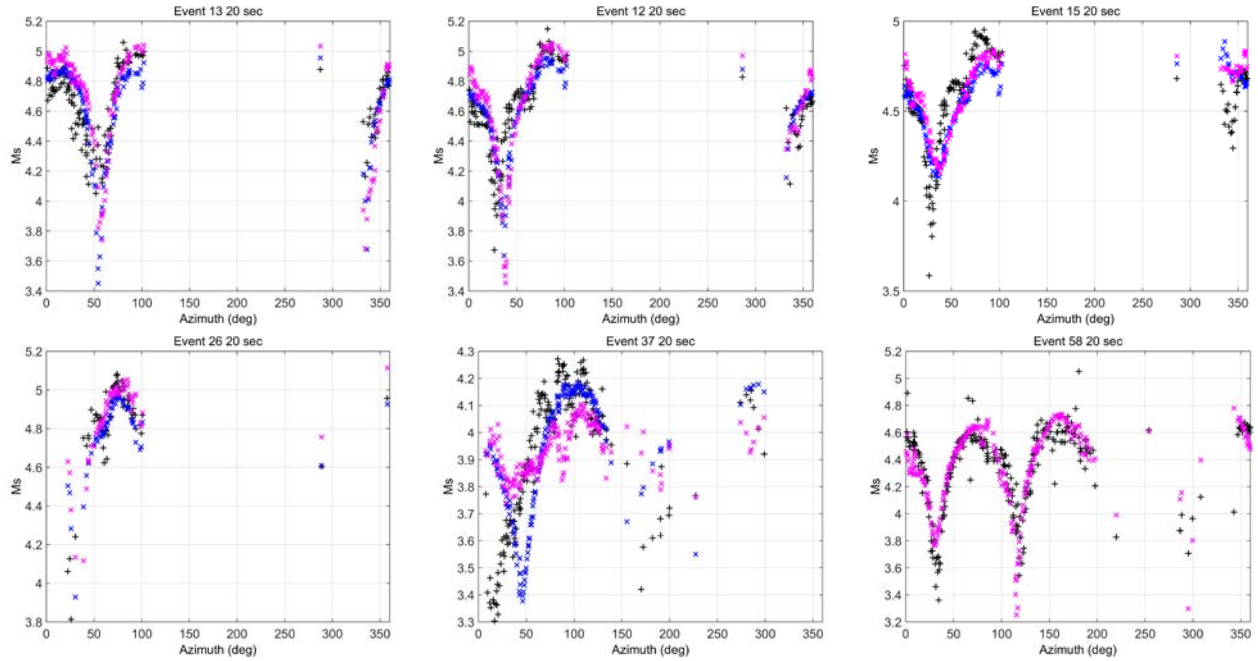
We expect the explosion sources to generate the same focusing/defocusing and diffraction effects as the CMT sources and to be more robust against nodal anomalies, so in general we expect them to be the better choice for application of station corrections. The mean and standard deviation of the station corrections as a function of range is shown in Figure 27. As can be seen in both Figure 26 and Figure 27 there is more variability at 10 seconds than at 20. There is also more variability in the station corrections derived from the Leidos structures than in the station corrections derived from the WUS structures, most likely due to the Leidos structures having sharper boundaries.



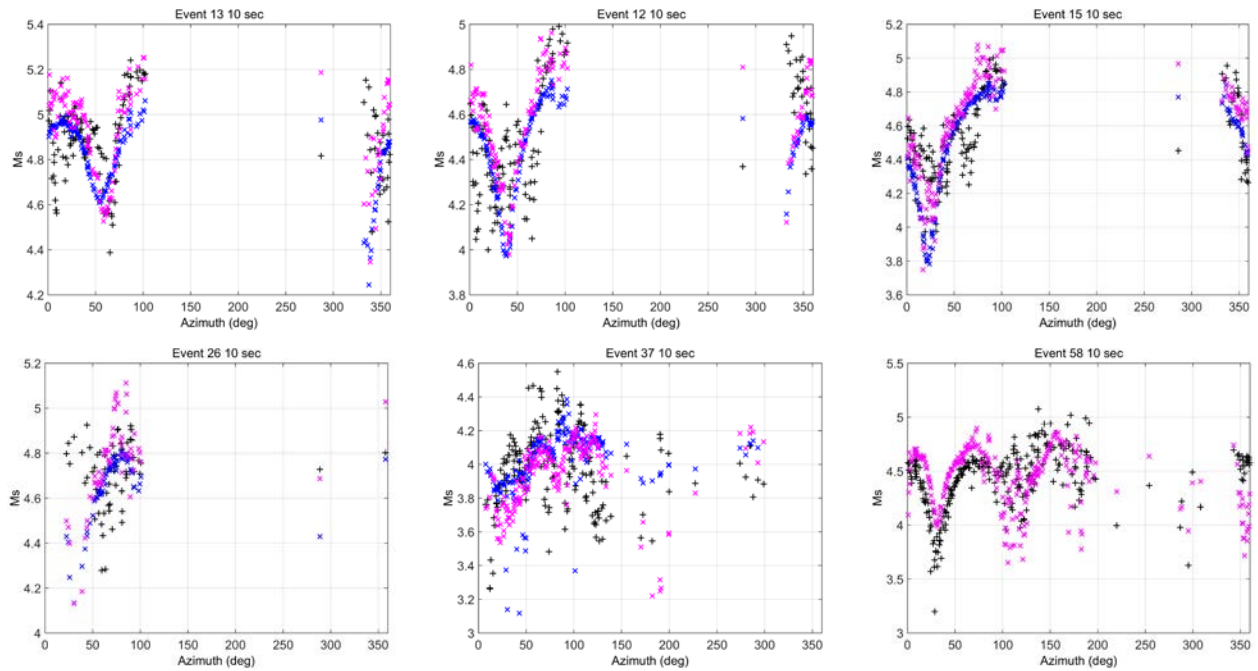
**Figure 27. Mean and standard deviation of station corrections as a function of range for Leidos structures (top) and WUS structures (bottom). Left: 10s; right: 20s.**

Figure 28 and Figure 29 show comparisons of observed and calculated amplitudes for 6 events at 20 and 10 seconds period, respectively. Calculations are shown for both the WUS and Leidos structures. Although the calculated and observed amplitudes agree fairly well, it is clear that almost all of the amplitude variation is due to radiation pattern rather than structural effects. Furthermore, the comparison is very sensitive to accurate CMT solutions. For event 37 in particular, the difference between observed and calculated amplitudes is very large at some azimuths due to errors in the predicted radiation pattern. The observed and calculated data have very similar shapes for that event, but they are shifted by about 30 degrees. Both the calculated and observed variability due to structure are small at 20 seconds (remember that all paths are less than 1000 km).





**Figure 28. Calculated and observed 20 second surface wave amplitudes for 6 events recorded on the US Array. Black: observations; Blue: calculations with WUS  $\frac{1}{4}^\circ$  structures; Magenta: calculations with Leidos  $1^\circ$  structures.**



**Figure 29. Calculated and observed 10 second surface wave amplitudes for 6 events recorded on the US Array. Black: observations; Blue: calculations with WUS  $\frac{1}{4}^\circ$  structures; Magenta: calculations with Leidos  $1^\circ$  structures.**

There is considerably more structural variability at 10 seconds, and the amount of variability in the observed and calculated data is comparable, however there is not good agreement between calculated and observed amplitude variations at individual stations.

Figure 30 and Figure 31 show histograms of surface wave amplitudes at 20 and 10 seconds, respectively, for one event. Two types of corrections are used, derived from SurfMembrane calculations using CMT and explosion sources as described above. We cannot expect a large reduction in amplitude variability, because most of the amplitude variability is due to radiation pattern. With the CMT-derived corrections the variability is actually increased. With the explosion-derived corrections we do get a small improvement. At 20 seconds the standard deviation is reduced from 0.280 to 0.266, and at 10 seconds from 0.187 to 0.181. The 10 second variability is smaller than the 20 second variability because structural effects wash out some of the highs and (particularly) lows in the radiation pattern in both the calculated and observed data.

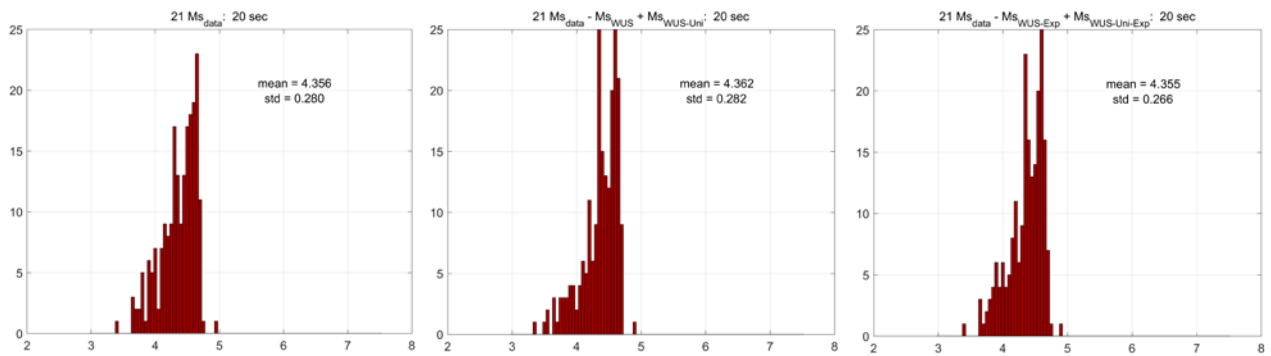


**Figure 30. Histogram of 20 second surface wave amplitudes for one event. Left: Uncorrected; Middle: Corrected with CMT derived correction; Right: Corrected with explosion derived correction.**

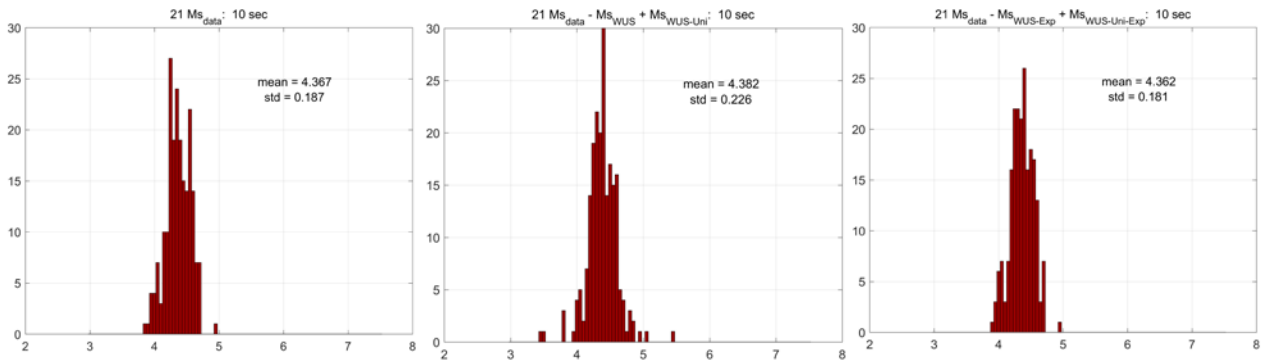


**Figure 31. Histogram of 10 second surface wave amplitudes for one event. Left: Uncorrected; Middle: Corrected with CMT derived correction; Right: Corrected with explosion derived correction.**

For some events and some stations there is additional variability in the data that is not easily explained by either radiation pattern or structure. Figure 32 shows the measured amplitudes (shown as magnitudes calculated from the amplitudes) for one event and the amplitudes calculated with the two sets of structures. The calculations reproduce the observed radiation pattern quite well, especially at 20 seconds, however there is still a substantial amount of unexplained variability in the data including high observed amplitudes right at the node.

We took a closer look at the station with the highest amplitude, which is located very close to the node. It would take an extreme structural variation to cause this type of effect. That station is H17A, which is located just west of Yellowstone Lake and event 21 is just west of Reno, NV. The path does have some significant complexity, but the earth model we are using does not have enough variability to cause an effect of that magnitude. However, Lou and van der Lee (2014) show a very large S-wave travel time anomaly at exactly the same location, so there may be a large structural anomaly that is not captured by our current models.

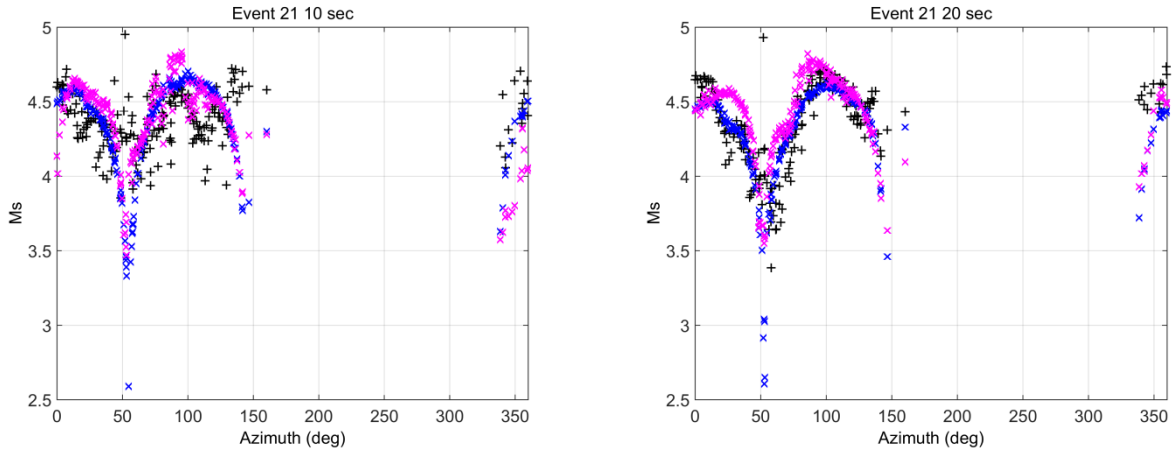


**Figure 32. Predicted and observed station magnitudes for event 21. Black crosses are observed magnitudes, blue x are WUS calculations, magenta x are Leidos calculations. Calculations used the CMT solution for each source. Left: 10s, right: 20s.**

Figure 33 shows amplitude vs. distance for stations close to the direction of H17A and although there is some increase in amplitude for the two next most distant stations, this station is clearly an outlier. Figure 33 also shows waveforms from H17A and I16A, which is in the same direction, but 100 km closer to the source and has only 20% of the amplitude. Both waveforms look normal and show no evidence of data problems such as a noise spike. It is possible there is a calibration error at this station, however a comparison of several other events also recorded at this station show considerable variation but not a persistent high anomaly.

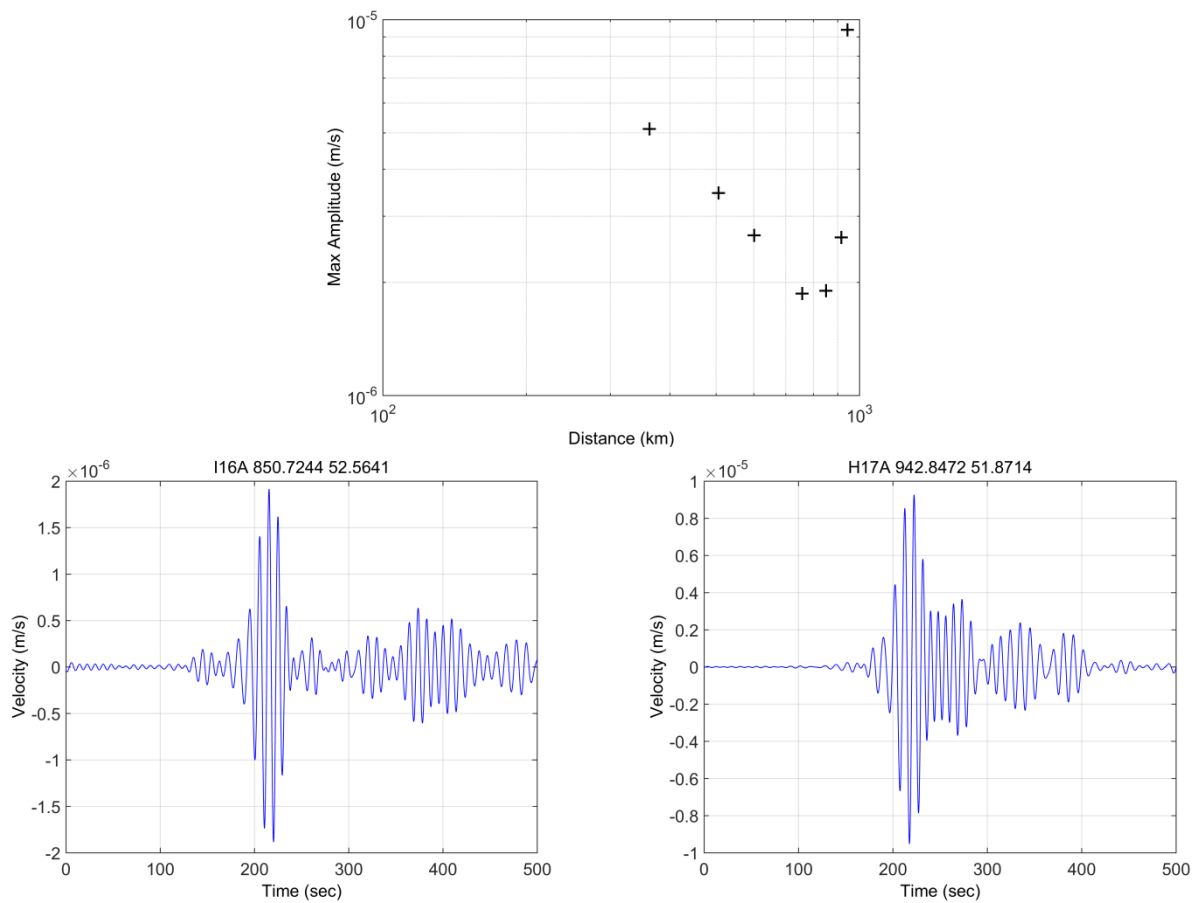


**Figure 33. Top: amplitudes at 7 stations close to 50 degree azimuth. Bottom: waveforms at station I16A (left) at 850 km and H17A (right) at 942 km band-pass filtered at 10 seconds. *The amplitude increases by a factor of 5 between the two stations.***

## 4.6 Inversion of Eurasian Attenuation Data for Q Structure

Inversion of the Eurasian attenuation data set follows the same procedure used by Stevens et al (2008), which is summarized here. Inversion of attenuation data for Q structure is accomplished by solving equation 19 using the LSQR algorithm (Nolet, 1987).

$$\begin{pmatrix} A \\ sH \\ \lambda I \end{pmatrix} \Delta \mathbf{x} = \begin{pmatrix} \Delta \mathbf{d} \\ -sH\mathbf{x} \\ \lambda(\mathbf{x}_c - \mathbf{x}) \end{pmatrix} + \boldsymbol{\varepsilon} \quad (19)$$

where:

1. The data  $\Delta \mathbf{d}$  are attenuation residuals. Attenuation estimates are derived from an existing Q model, and the differences between those and the observations are the data used in the inversion.
2. The matrix  $\mathbf{A}$  is derived from partial derivatives of the attenuation coefficients with respect to model Q in each layer for the path-averaged inversion. The velocities and densities used to calculate partial derivatives correspond to the final models from Stevens et al (2005).
3. The starting model  $\mathbf{x}$  and constraining model  $\mathbf{x}_c$  are the same, and are derived from PREM for depths greater than 100 km, and Swanger's Law ( $Q=100 \beta$ , with  $\beta$  in km/s) for shallower depths. The values derived from PREM are  $Q=18 \beta$  for depths between 100 km and 220 km,  $Q=30 \beta$  at greater depths. There are discontinuities at 100 km and 220 km and a smoothness criterion is applied to layers above and below 100 km. The inversion is performed for layers shallower than 220 km. Q is fixed to  $18 \beta$  at 220 km depth and to  $30 \beta$  below this depth.
4.  $\mathbf{H}$  is a difference operator that applies to vertically neighboring layers and has the effect of constraining the vertical smoothness of Q profile.  $\mathbf{H}$  applies to layers in the crust and upper mantle, but has explicit discontinuities as described above.  $\mathbf{s}$  is the weighting of the smoothness constraint and can be a diagonal matrix (for variably weighted smoothing) or a scalar (constant smoothing).  $\mathbf{I}$  is the identity matrix and  $\lambda$  weights the damping which constrains the norm of the difference between final Q structures and constraining model  $\mathbf{x}_c$ .  $\lambda$  can be a scalar for constant damping, or a diagonal matrix for variable damping.
5. The model vector  $\Delta \mathbf{x}$  consists of  $\beta/Q$  for each layer that is free to change in each structure, and optionally can include the change in moment of each event. That is, for attenuation residuals that were derived using spectra with a fixed model moment, the moment for each event can be corrected as part of the inversion.
6.  $\boldsymbol{\varepsilon}$  is the vector of residuals that remain after inversion (the inversion minimizes  $|\boldsymbol{\varepsilon}|$ ).

Unlike inversion for shear velocity, inversion for Q is linear, so only a single iteration is necessary, although multiple inversions are done with different damping and smoothing parameters to generate realistic models.

Surface wave propagation in a heterogeneous, anelastic structure takes the following form, separating source, path and receiver (notation follows Harkrider et al, 1994):

$$u_z(\omega, r, \varphi) = \frac{1}{\sqrt{a_e \sin(r/a_e)}} \sqrt{\frac{2A_{R_1}}{\pi\omega c_1^2}} \sqrt{c_2 A_{R_2}} \exp\left[i\left(\pi/4 - \omega r / c_p - \gamma_p r\right)\right] F_s(\omega, \varphi, h) \quad (20)$$

where  $\omega$  is angular frequency,  $r$  is source to receiver distance,  $h$  is source depth,  $a_e$  is the radius of the earth,  $\varphi$  is azimuth,  $A_R$  is the Rayleigh wave amplitude function,  $c$  is phase velocity,  $\gamma$  is the attenuation coefficient, and the subscripts 1, 2, and  $p$  refer to parameters derived from the source region structure, parameters derived from the receiver region structure, and parameters which are defined by path averages, respectively. All source properties are contained in the function  $F_s$ .

Collecting the distance independent terms, equation 20 can be written in the form:

$$|u_z(\omega, r)| = M_0 \frac{S(\omega)A(\omega)\exp[-\gamma_p(\omega)r]}{\sqrt{a_e \sin(r/a_e)}} \quad (21)$$

where  $M_0$  is the source moment and  $S(\omega)$  the source function (important for large events),  $A(\omega)$  is a frequency dependent function that depends on source and receiver structure and focal mechanism. We assume that  $A(\omega)$  can be predicted well enough from the background earth structure and the source mechanism which is usually defined by a CMT moment tensor. While the inversion program has the capability to allow an amplitude scale factor for each path, which would allow variations in explosion amplitude due to tectonic release, and variations in earthquake amplitude due to errors in source mechanism, in the inversions that follow we only allowed the moment to vary, which is a constant factor for all paths for a single event. In equation 21,  $M_0$  and  $\gamma_p$  are derived from a starting source mechanism and background earth model, and allowed to vary in the inversion while the other factors are held fixed.  $S(\omega)$  is derived for a triangular function with rise time (half-duration)  $T$ . Since this is approximate, points where  $fT > 0.5$ , which corresponds to an amplitude reduction of 0.4, are zero weighted. The observed data can then be written:

$$|u_z^o(\omega, r)| = M_0^o \frac{S(\omega)A(\omega)\exp[-\gamma_p^o(\omega)r]}{\sqrt{a_e \sin(r/a_e)}} \quad (22)$$

And the log ratio of observed to predicted spectra has the form:

$$\ln \left| \frac{u_z^o(\omega, r)}{u_z(\omega, r)} \right| = \ln \frac{M_0^o}{M_0} + [\gamma_p(\omega)r - \gamma_p^o(\omega)r] = \Delta \ln M_0 + r\Delta\gamma \quad (23)$$

$\Delta\gamma$  can be further expanded into a sum over Q structure in each structure traversed by the ray along the source to receiver point multiplied by the fraction of ray over each structure. So we can rewrite equation 23 as:

$$\frac{1}{r_{ik}} \ln \left| \frac{u_z^o(\omega, r)}{u_z(\omega, r)} \right|_{ik} = \frac{1}{r_{ik}} \Delta \ln M_0^k + \sum_{l=1}^L \frac{\Delta r_{lik}}{r_{ik}} \sum_{j=1}^J G_{lj} \Delta \left( \frac{\beta}{Q} \right)_{lj} \quad (24)$$

The subscript k refers to an event, i refers to a single path for event k, l refers to each model type traversed by the ray and  $\Delta r_{lik}/r_{ik}$  is the fraction of the path that the ray spends in each model. The subscript j refers to layer number in each model. L is the total number of model types traversed and J is the total number of layers allowed to change in each model. So the data in the inversion is the left hand side of equation 24, the spectral ratio divided by the distance for multiple frequencies,

and the inversion is performed for the quantities  $\Delta \ln M_0^k$ , the change in moment of each event, and  $\Delta(\beta/Q)_{ij}$ , the ratio of shear velocity to  $Q$  in each layer of each model. The function  $G_{ij}$  gives the change in  $\gamma$  with respect to change in  $\beta/Q$  and can be written assuming no bulk attenuation in terms of partial derivatives of phase velocity with respect to material velocities as:

$$G_{ij} = \frac{\partial c_l}{\partial \beta_{ij}} + \frac{4}{3} \frac{\beta_{ij}}{\alpha_{ij}} \frac{\partial c_l}{\partial \alpha_{ij}} \quad (25)$$

The inversions described below all invert data of the form described above. We also compare with interstation attenuation estimates. Using equation 23 again at two or more stations at distances  $r_n$ , we get a set of equations of the form:

$$\ln \left| \frac{u_z^o(\omega, r_n)}{u_z(\omega, r_n)} \right| = \Delta \ln M_0 + r_n \Delta \gamma \quad (26)$$

The equations define a line with slope  $\Delta \gamma$  and intercept  $\Delta \ln M_0$  so this can be used as a check on the inversion by finding the average change in attenuation over all or a subset of paths for each event, and the change in moment.

#### 4.6.1 Data used in the Q Inversion

As discussed in section 3, we retrieved 59,000 waveforms from 1850 Eurasian and African events. We also retrieved the locations, depths and origin times for all of these events from the International Seismological Center (ISC), and replaced the CMT origins and depths with the better ISC origins. We then derived phase-matched filters from the CMT moment tensors of each event, applied these to the data, and assembled a data set of smoothed, instrument corrected spectra. These measured spectra were then divided by the theoretical calculated spectral amplitudes and saved at a set of frequencies corresponding to periods between 8 and 50 seconds.

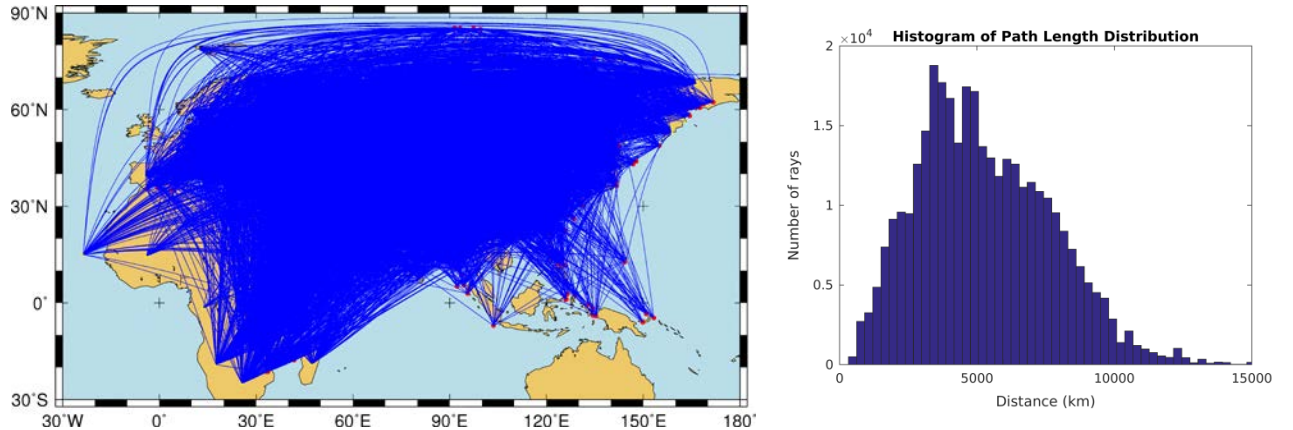


**Figure 34. Left: Map showing location of all rays used in the inversion. Right: histogram of path lengths used in the inversion.**

These formed the data on the left hand side of equation 26. These data were then combined with the data set from the 2008 study and put through an aggressive data quality procedure to prune out bad or noisy data, and deep events or data with bad depths or focal mechanisms. This resulted in a high quality data set of 23,148 spectra from 998 events. There were an average of 14.8 spectral data points for each waveform, leading to a total data set of 343,322 data points. Figure 34 shows

a map of all of the ray paths used in the inversion, and the distribution of path lengths in the data set.

#### 4.6.2 Q Inversion Results

The result of the inversion is adjustments to Q structure in each model layer and adjustments to the moment of each event. Figure 35 shows the adjustment in moments (equation 26) that were output from the inversion. Figure 35 also shows the mean and mean  $\pm$  standard deviation of the raw data, the data after weighting (derived from quality control procedure) was applied, and after moment adjustments were applied.

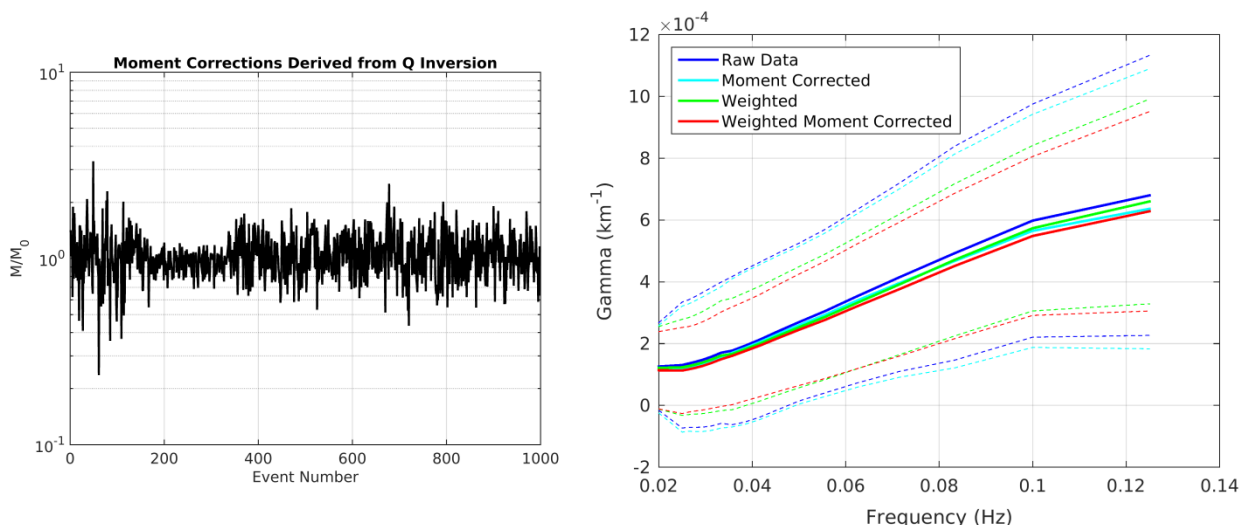


**Figure 35. Left: Adjustments to moments in the CMT data set. Right: average gamma data over all paths, together with average gamma after moment adjustments and weighting.**

Figure 36 shows a comparison of inversion results with the data and with the starting model. As we also found in the 2008 study, the data and inversion results show considerably more attenuation than the starting model, and much more variability. The standard deviations are larger at the closer ranges because variations due to structure are larger relative to variations due to attenuation at short distances.



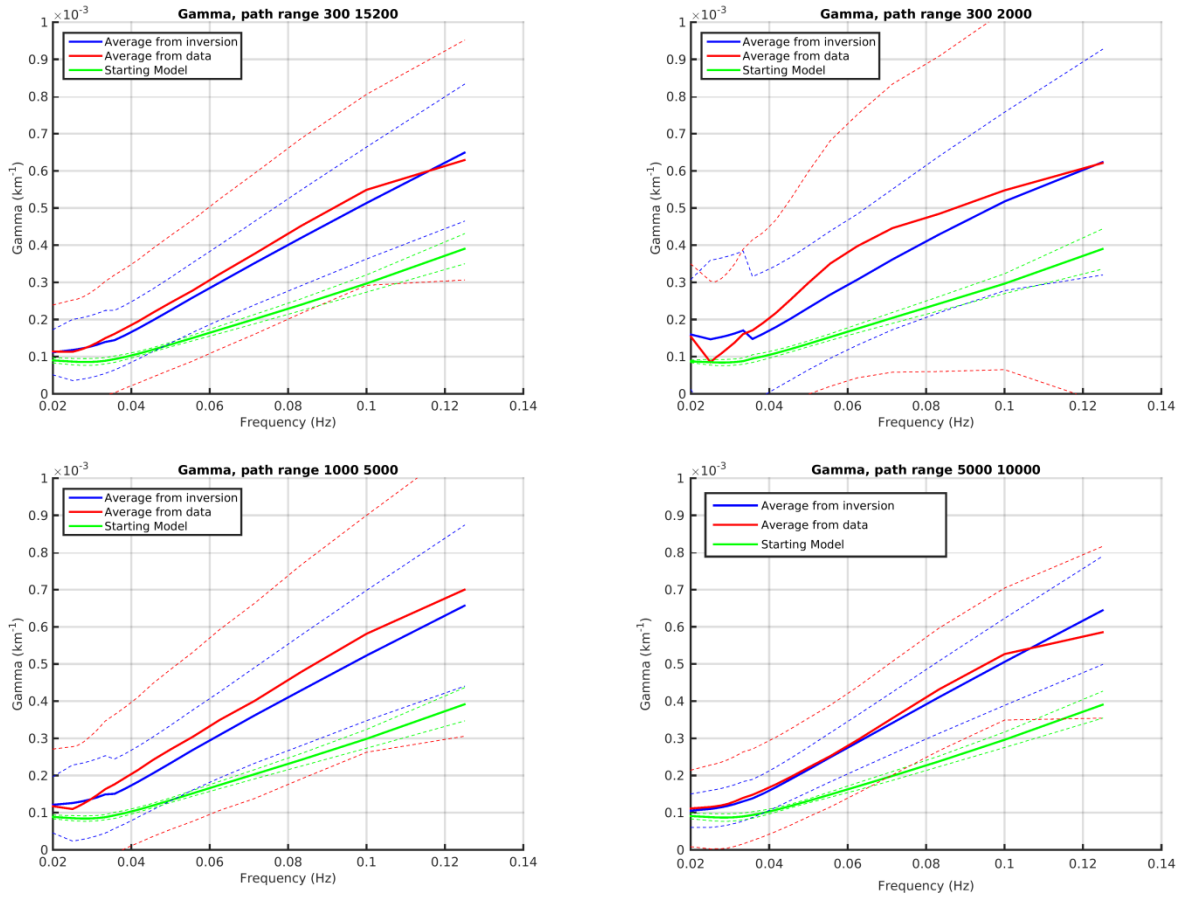


**Figure 36. Gamma data and inversion results compared with starting model over several distance ranges. Upper left: all data; upper right: 300-2000 km; lower left: 1000-5000 km; lower right: 5000-10000 km. Solid lines are mean; dashed lines mean  $\pm$  standard deviation. Numbers in the titles are distance ranges.**

Figure 37 shows the results of the inversion plotted on a map of Eurasia and Africa. There is a band of high surface wave attenuation that stretches across the Middle East from the Mediterranean Sea to India. This is also consistent with the 2008 results, although there is much more data in this inversion than the 2008 inversion.

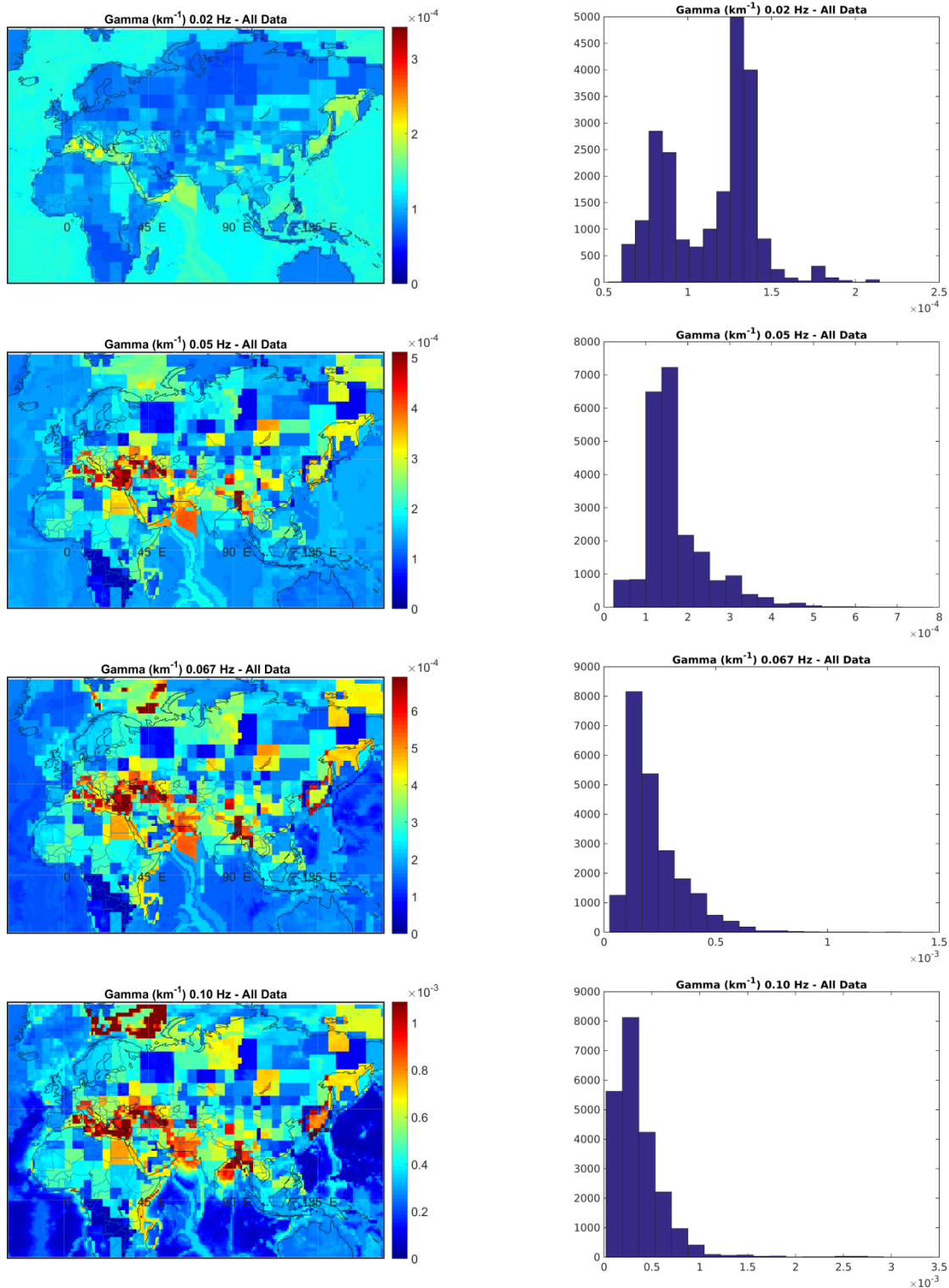


**Figure 37. Left: Attenuation maps at four frequencies. From top to bottom: 0.02 Hz (50 seconds period), 0.05 Hz (20 seconds), 0.067 Hz (15 seconds), 0.1 Hz (10 seconds). Right: histograms of gamma values for each frequency.**

## 4.7 Application of SurfMembrane to Eurasian events

Surface wave membrane calculations require considerably more computation time for the Eurasian events because paths are much longer, averaging about 5,000 km. Calculations take approximately one hour to complete, still much less than a corresponding 3D finite difference calculation. For these calculations, we derived phase velocity maps centered on each event (Figure 38), and we ran four calculations for each event: a calculation using the CMT solution with the heterogeneous structure and a calculation using the CMT solution with a homogeneous structure, and explosion calculations in the heterogeneous and homogeneous structures.

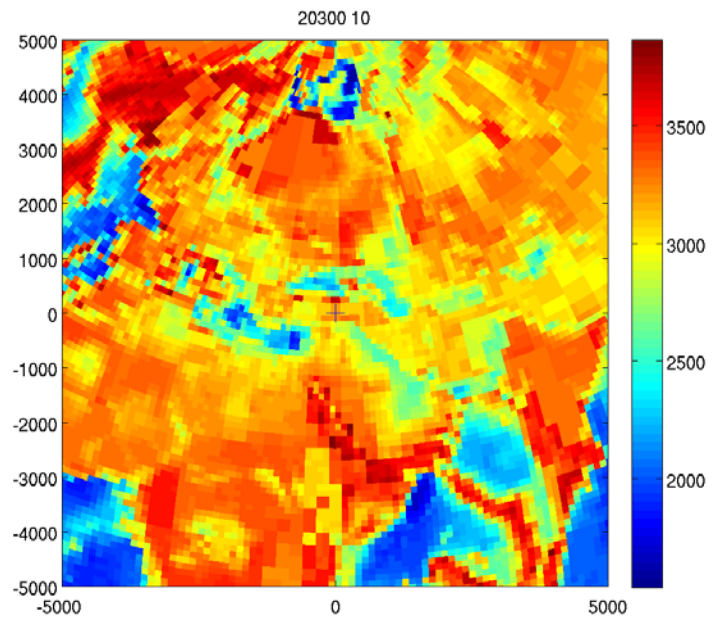


**Figure 38. Example phase velocity map for event 20300.**

Membrane calculations in heterogeneous structures generated surface waves with much more variability than uniform structures. Figure 39 shows the surface waves for two calculations at 10 and 20 second periods after 650 time steps at which time they have propagated to about 4000 km from the source. All show strong signs of diffraction and the surface waves seem to break up where they cross strong boundaries such as at boundaries with oceanic structures, particularly at 10 seconds. Figure 40 shows the peak amplitudes at each point from the homogeneous and heterogeneous calculations for one of these events.

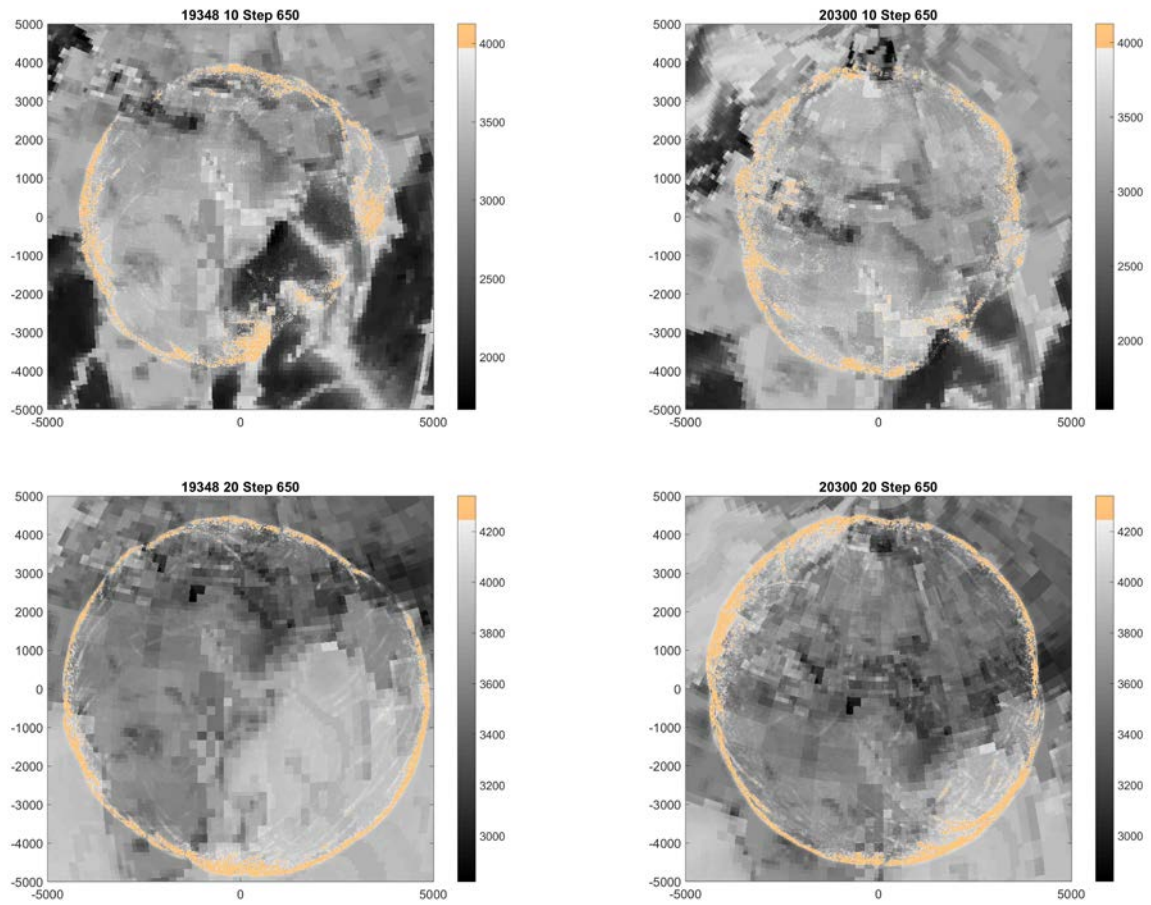


**Figure 39. Surface waves from two events at 10 seconds (top) and 20 seconds (bottom) showing strong diffraction, especially for 10 seconds waves crossing oceanic boundaries.**

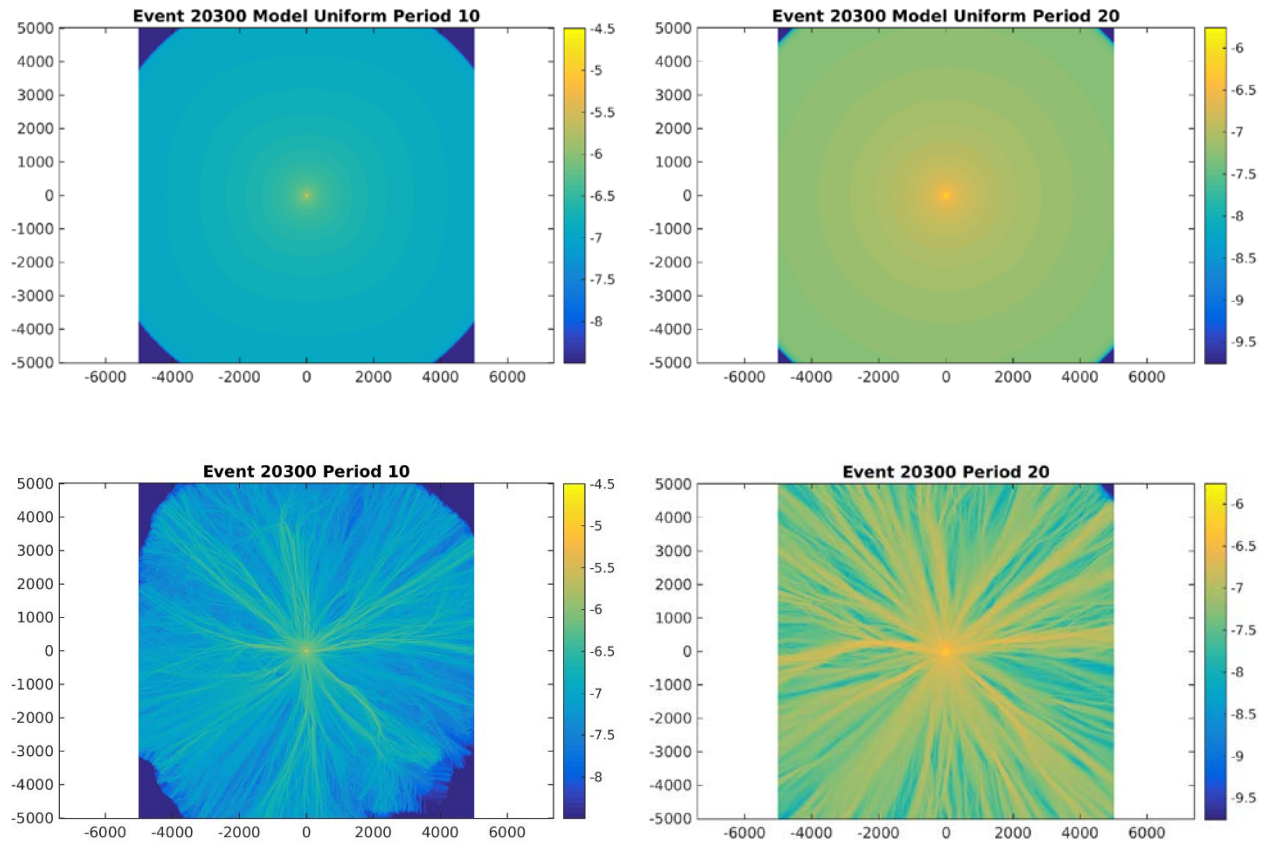


**Figure 40. Log surface wave peak amplitudes at each point for event 20300 at 10 seconds period (left) and 20 seconds (right).**

Figure 41 shows the ratio of the peak amplitudes between the heterogeneous and homogeneous calculations at each point. These “dandelion plots” correspond to the predicted surface wave amplitude correction for each point, and they can be quite large. Unfortunately, they are also very sensitive to earth structure along the path and small changes in earth structure can cause these patterns to shift, substantially changing the amplitude correction at each point.



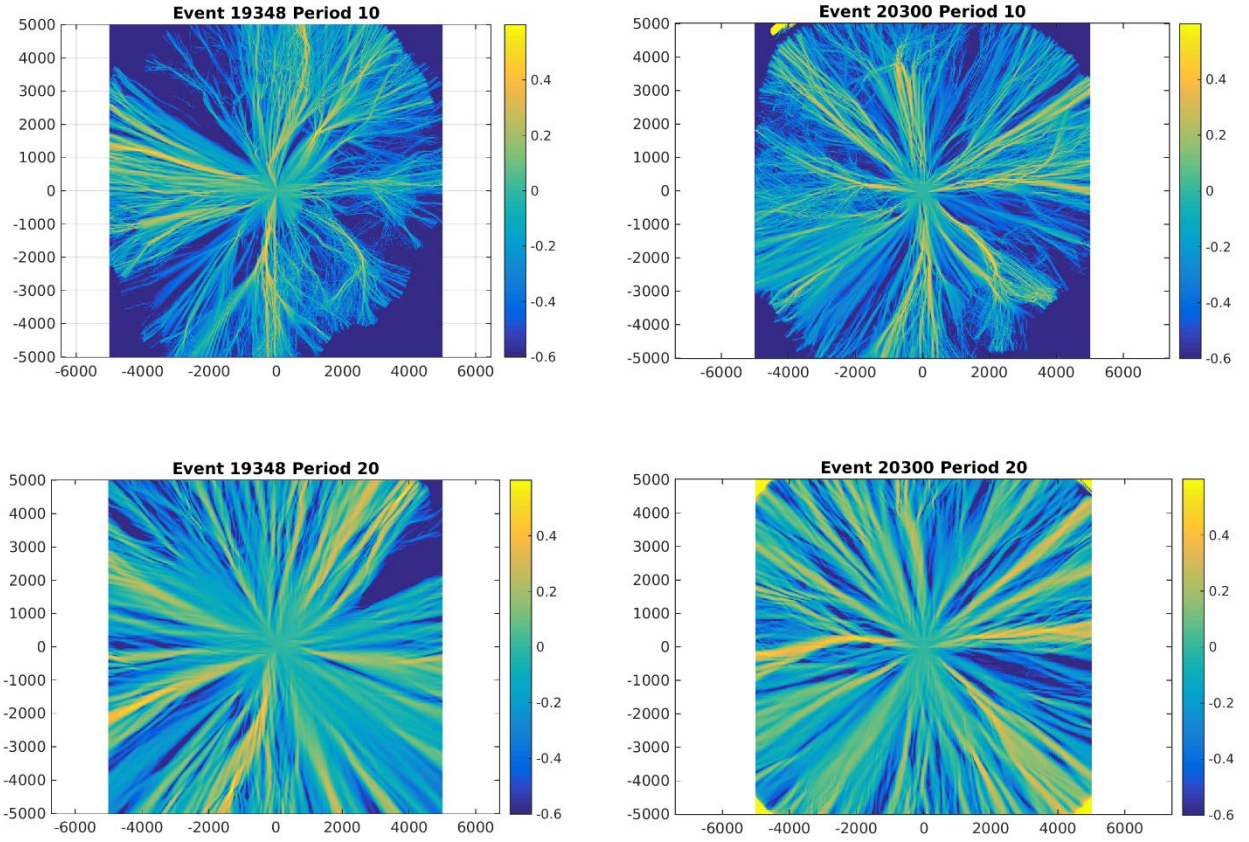


**Figure 41. Log ratio of surface wave amplitudes in heterogeneous to homogeneous structure for the two events shown in Figure 39. Top: 10 seconds. Bottom: 20 seconds.**

#### 4.7.1 $M_s$ Estimation in Heterogeneous Structures

We want to use surface wave membrane calculations to correct for structural variations in amplitude. In this section we perform an uncertainty analysis to determine under what conditions such corrections are likely to improve  $M_s$  measurements. The membrane calculations rely on phase velocity maps acquired through tomographic inversion. The phase velocity maps are then used to calculate the effects of material properties on surface wave propagation. While the calculations can model diffraction and scattering in heterogeneous structures, the results are only as accurate as the underlying Earth model. Any errors in the phase velocity map used to perform the calculation are propagated into the subsequent surface wave magnitude estimate. In the analysis above, calculation of “dandelion” plots that estimate the  $M_s$  corrections from the surface membrane calculations have assumed that the underlying models are approximately valid. Here we examine the effects of phase velocity model uncertainties on the resulting surface waves.

## Simulation Approach & Uncertainty Estimation

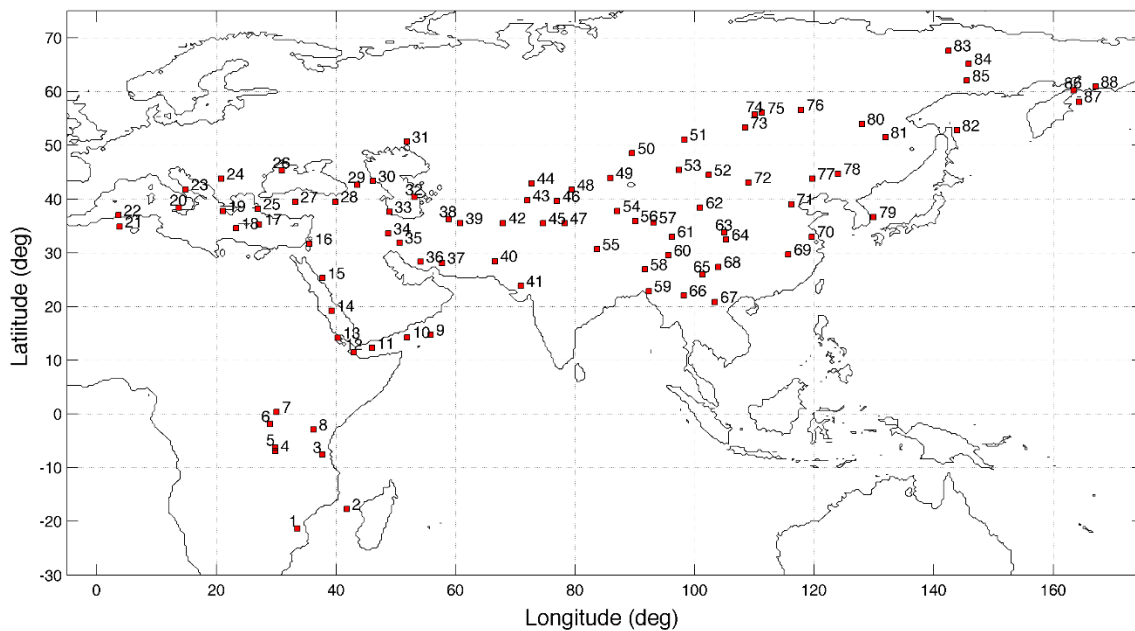


**Figure 42. Source locations for the 88 surface membrane calculations distributed throughout Eurasia and parts of Africa. The numbers near the red squares are an identifying label.**

For the following analysis, we use SurfMembrane to calculate surface wave magnitudes at 20-second period. Although surface wave measurements are performed over a narrow band of frequencies, filtering still contains components from nearby frequencies, so we must account for the subtle differences in phase velocity by generating results by superposition of at least a few phase velocities. To approximately account for the frequency dependence of phase velocity, we combine the results of three separate surface membrane calculations at phase velocities of 19, 20, and 21 seconds. Eighty-eight source locations distributed throughout Eurasia and parts of Africa were tested using an explosion source (Figure 42). Each calculation is centered on the source location, and spans  $\pm 3750$  kilometers distance along the North-South and East-West directions using 2 kilometer grid size and 0.3 seconds per time increment. For the calculations at each source location, the nominal phase velocity map is obtained by projecting the global Leidos 1-degree model to a two-dimensional surface centered on the source location (Figure 43).

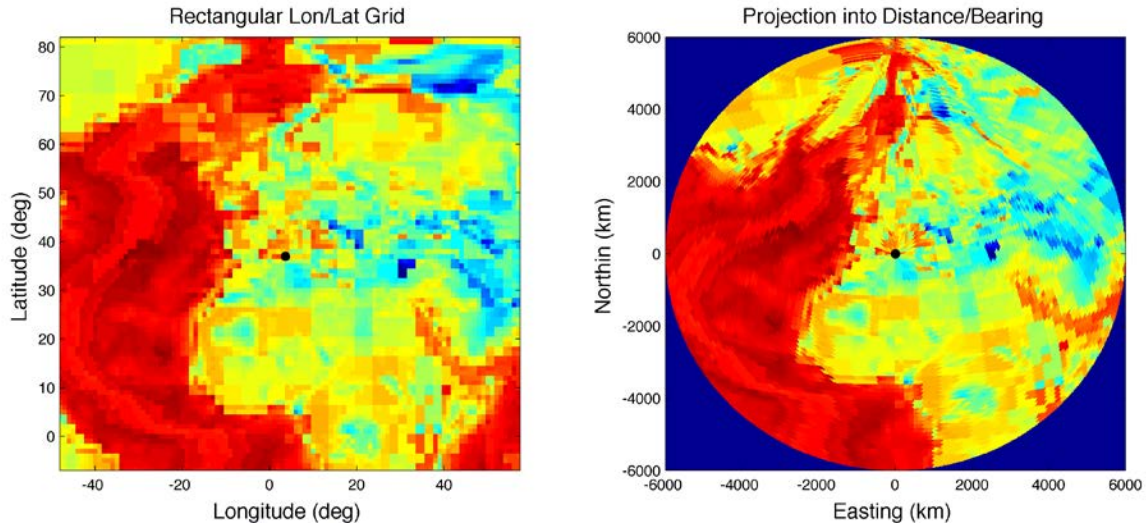


**Figure 43. Left panel: Phase velocity map on a 1-degree grid of longitude and latitude. Right panel: Projection of the map in the left panel to a Northing-Easting (x-y) coordinate system using the local distance/bearing.**

To study the effects of uncertainties in the phase velocity maps on the calculated surface waves, perturbations that are spatially correlated over  $\sim 100$  kilometers and with root-mean-squared fractional amplitude of 2.6% are added to the nominal phase velocity maps. The spatial scale and amplitude of the perturbations were estimated by comparing phase velocity maps for the Western United States from the University of Colorado (Shen et al., 2013) to the 1-degree maps developed by Leidos (Stevens et al., 2005) in the same region (Figure 44).

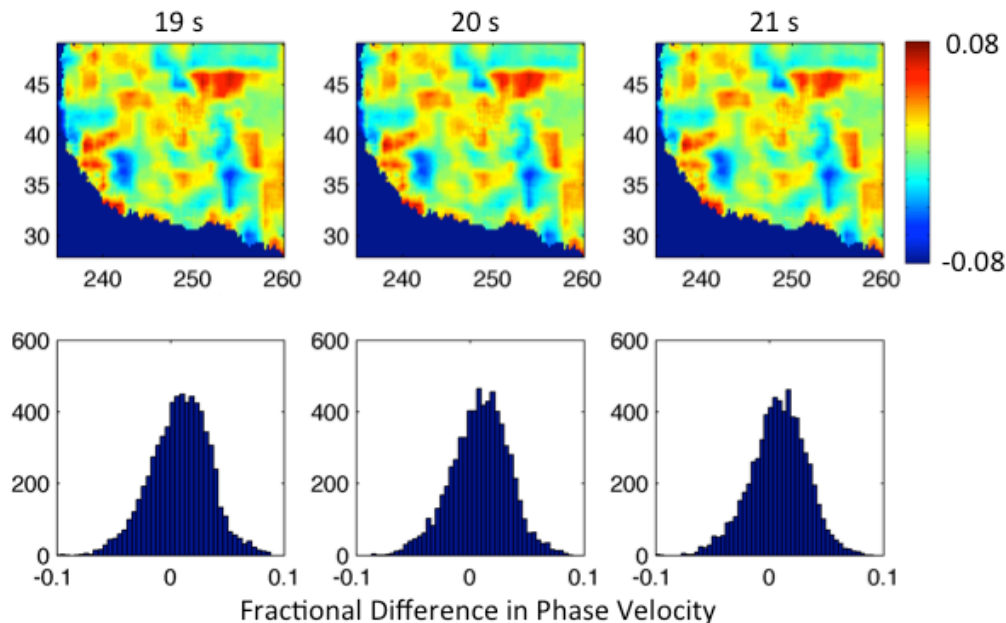


**Figure 44. Top panels: Fractional difference in the WUSA and Leidos phase velocity maps at 19, 20, and 21 s periods. Bottom panels: Distribution of differences, which are approximately Gaussian with standard deviation of about 2.6%.**



For each source location, the nominal Leidos phase velocity model is assumed to be the “correct” phase velocity map. An ensemble of twenty-five instances of perturbation maps is applied to the nominal model, and the surface membrane calculation is run for each instance. An example of an instance of the perturbation map is shown in Figure 45. The same perturbation map is applied to each phase velocity because the comparison of the maps in Figure 44 shows that the differences are consistent across nearby surface wave periods.

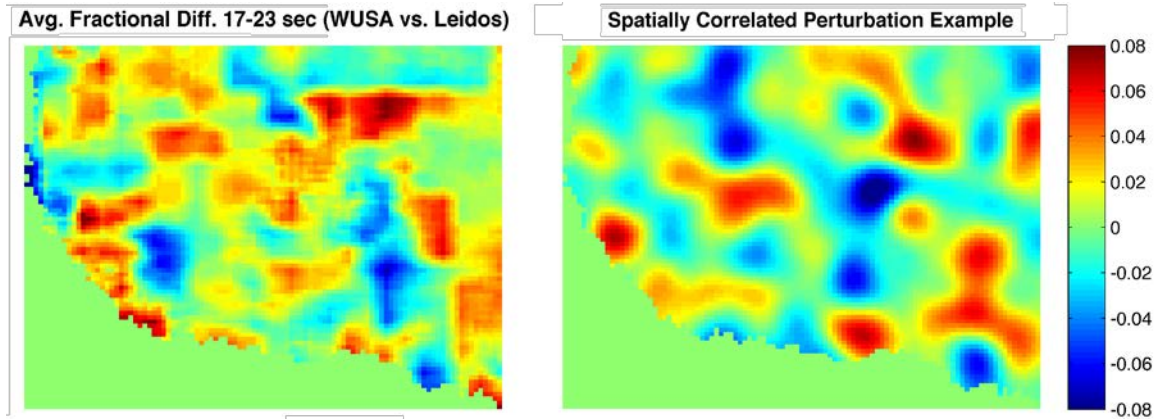


**Figure 45.** Left panel: Average fractional difference in the WUSA and Leidos phase velocity maps in the 17-23 s band. Right panel: Example of phase velocity map fractional perturbation that is applied to the Leidos Earth model.

Each perturbed map, when added to the nominal map, is an instance that theoretically *could have been* obtained given other data used in the inversion (Figure 46). When the underlying phase velocity map changes, the resulting surface wave amplitudes also change (Figure 47). Macroscopic features of the surface wave amplitudes, such as the number and approximate direction of amplification zones, are usually preserved. However, the precise directions where amplification reaches a local maximum or minimum can shift by a few degrees. At long ranges even a small shift in direction will move an amplification zone hundreds of kilometers. In other words, uncertainty in the phase velocity of even a few percent (due to limited data, systematic errors, or for any other potential reason) can move a particular location from a region of amplification to a region of de-amplification. This shows the importance of minimizing errors and uncertainty in the generation of phase velocity maps.

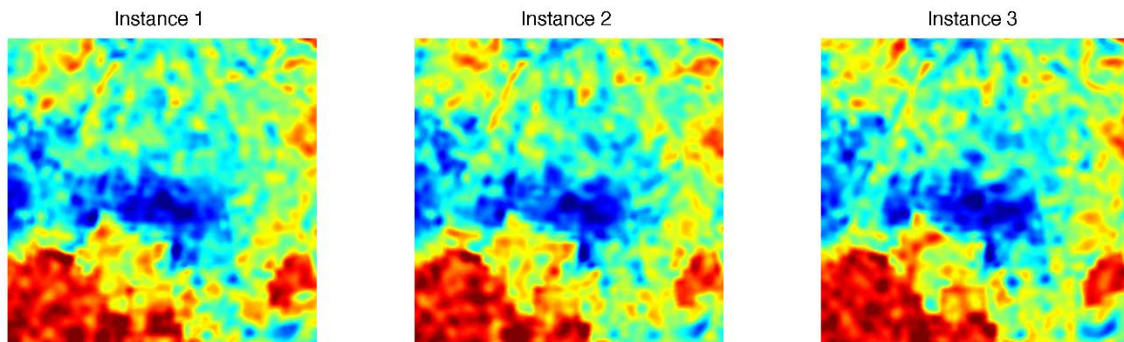


**Figure 46.** Examples of three instances of perturbed phase velocity maps at 20-second period. *The area shown is a 7500 km  $\times$  7500 km region near the Tarim Basin, centered on source #54. Dark blue color is 2800 m/s phase velocity, and dark red color is 4200 m/s phase velocity.*

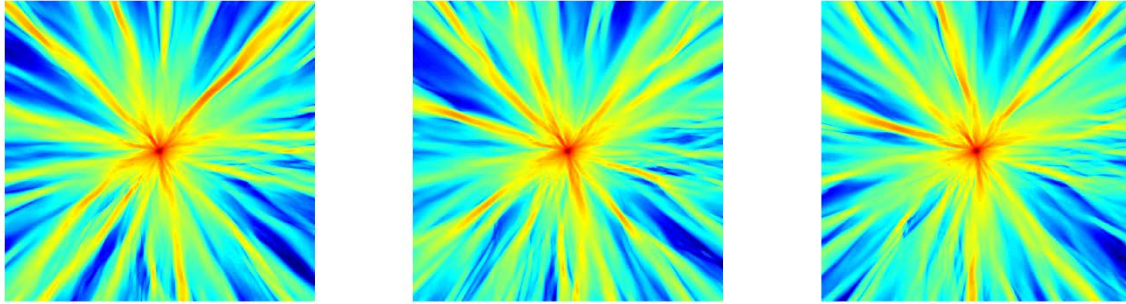


**Figure 47. Examples of surface wave amplitudes (dB) produced by separate perturbation instances applied to the same nominal phase velocity map. The area shown is a 7500 km  $\times$  7500 km. The color scale spans 2.2 dB from high (red) to low (blue) amplification regions. Note, these surface wave amplitudes do not correspond to the perturbation instances shown in Figure 6.**

For each of the 88 source locations, the root-mean-square deviation in the  $M_S$  measurement over the ensemble of 25 perturbation instances is used to estimate the uncertainty in  $M_S$  due to uncertainty in the underlying phase velocity map. Figure 8 shows a representative example of an  $M_S$  uncertainty map.

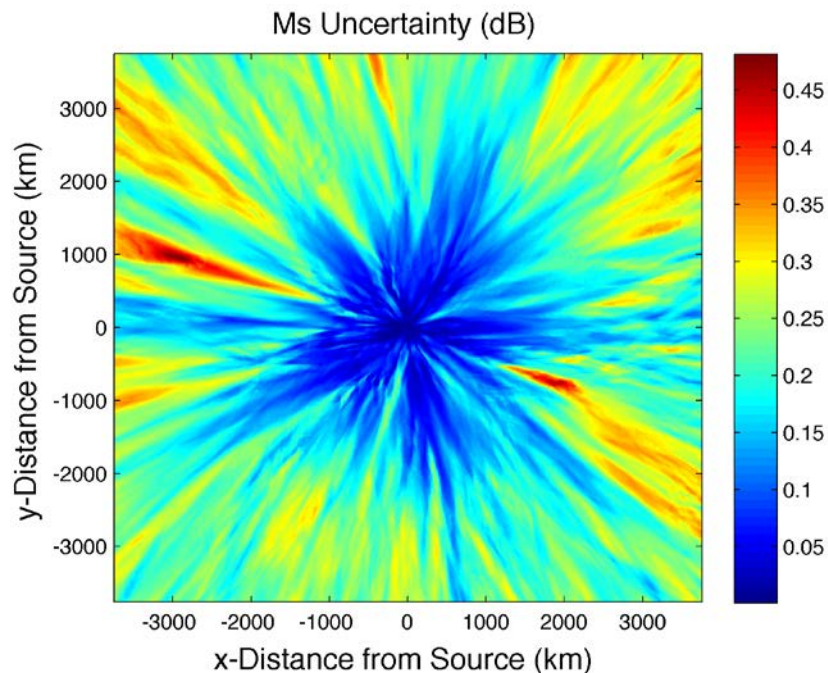


**Figure 48.  $M_S$  uncertainty map generated by calculating the standard deviation of  $M_S$  over an ensemble of 25 perturbation instances. This is from the same source as shown in the example in Figure 47.**

### Surface Wave Magnitude & Uncertainty Analysis

The “correction” to the  $M_S$  estimate due to heterogeneous Earth structure is obtained by subtracting the surface wave magnitude assuming a homogeneous structure from the magnitude generated by heterogeneous structure. Figure 49, Figure 50 and Figure 51 show the  $M_S$  corrections and projected phase velocity maps for the 88 source locations throughout Eurasia and parts of Africa that were shown in Figure 42. Nearby numbers correspond to source locations in proximity to each other (see Figure 42).



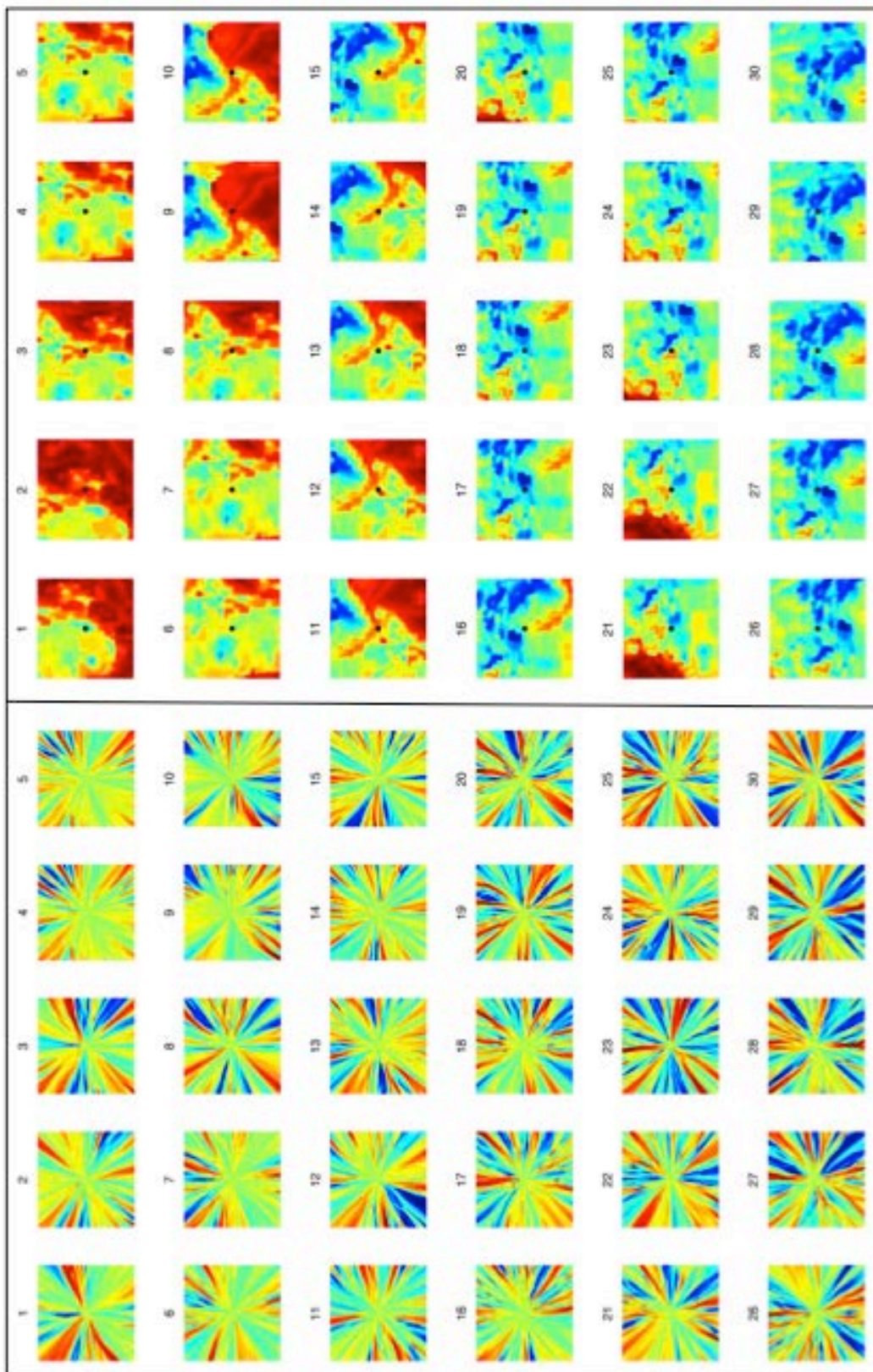


**Figure 49.**  $M_S$  corrections (bottom) and projected nominal 20-second phase velocity maps (top) for source locations 1-30.

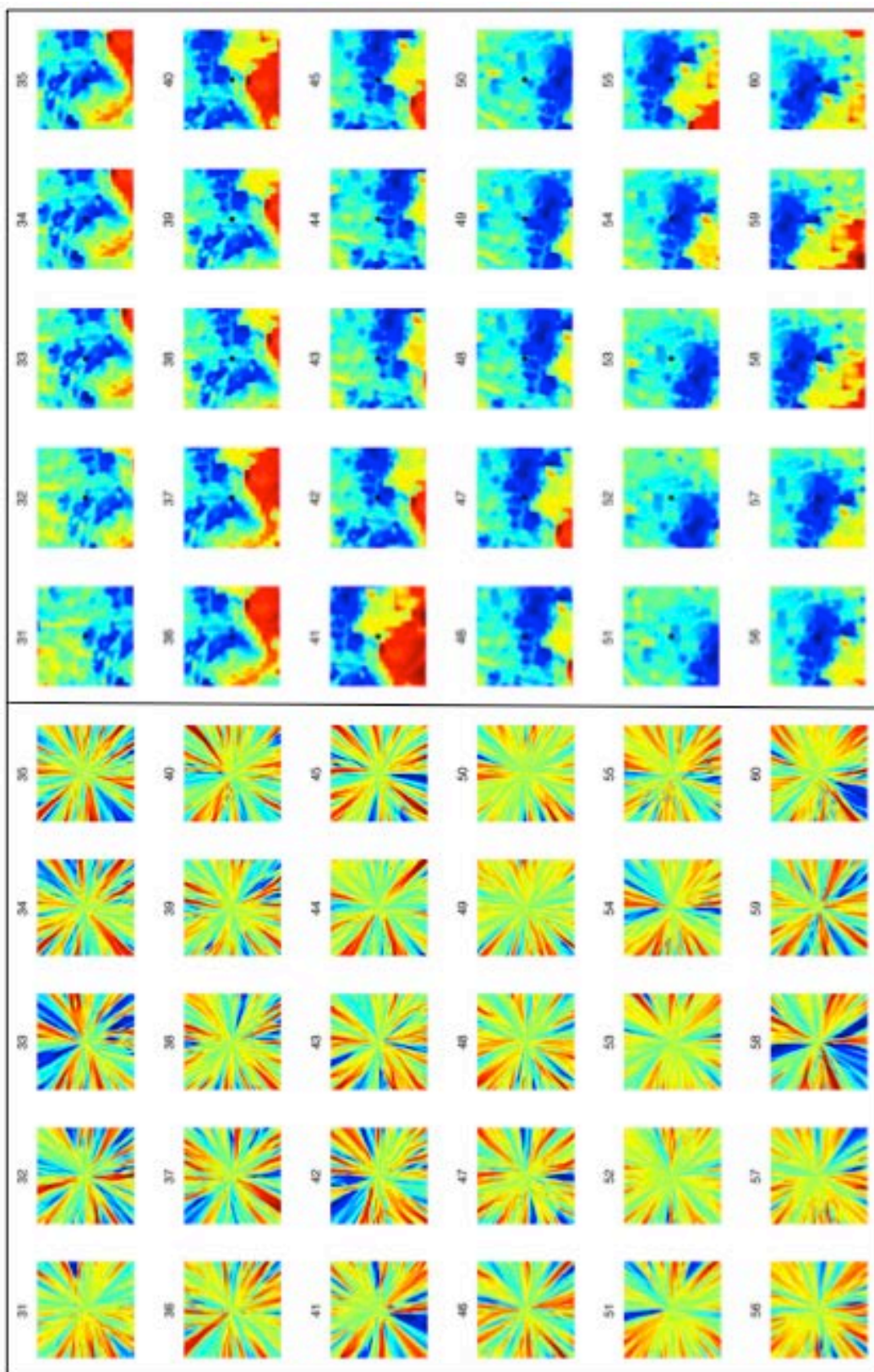


**Figure 50.**  $M_s$  corrections (bottom) and projected nominal 20-second phase velocity maps (top) for source locations 31-60.



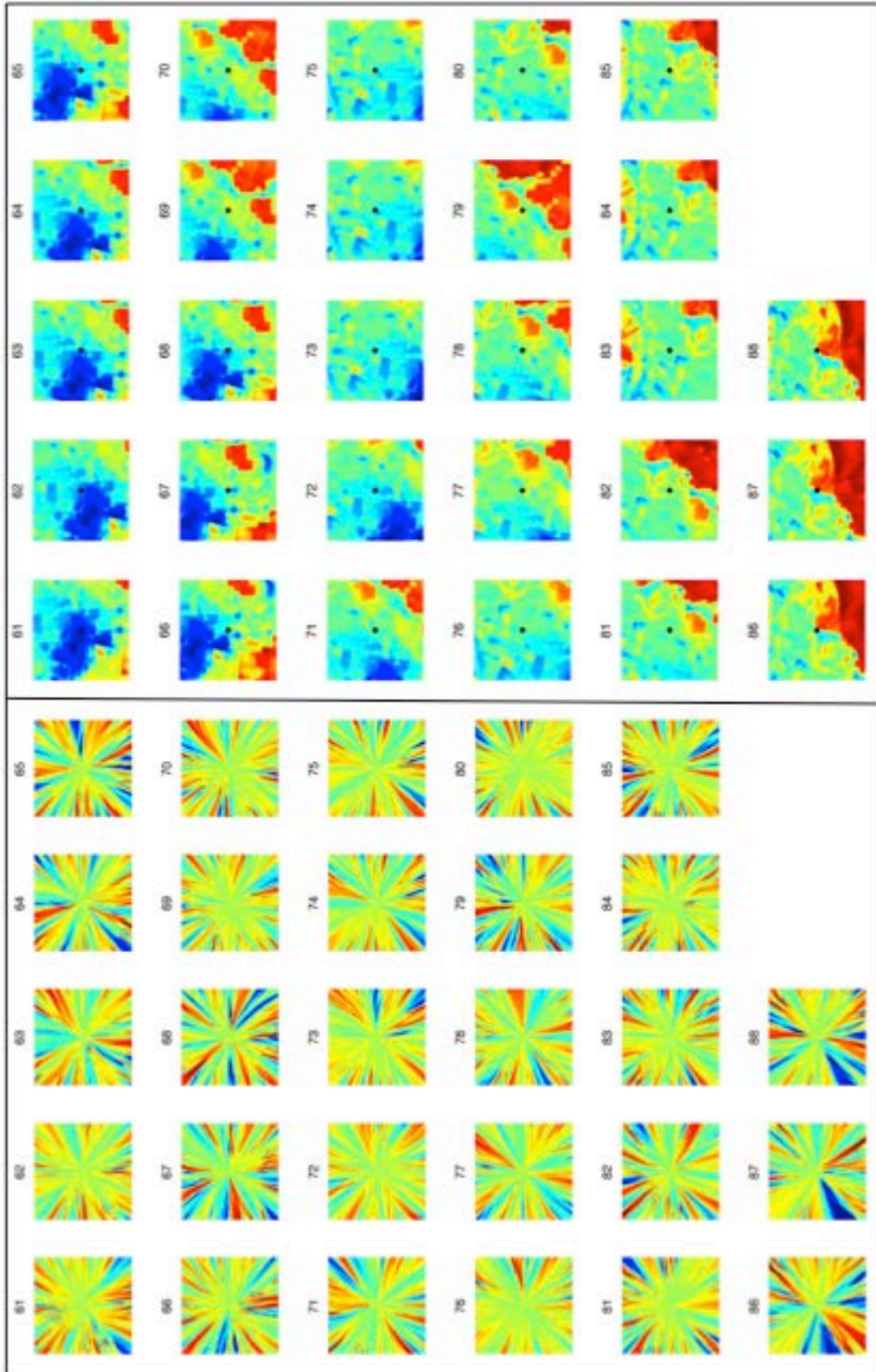


**Figure 51.  $M_s$  corrections (bottom) and projected nominal 20-second phase velocity maps (top) for source locations 61-88.**

The highly nonlinear nature of the resulting surface wave magnitudes makes comparison of the entire population of 88 source locations difficult. One approach taken here is to characterize each source location by the angle-averaged root-mean-square (rms) amplitude of the  $M_S$  corrections (restricted to ranges less than 2000 km, as explained below). For a source embedded in a completely uniform structure with a constant phase velocity, the  $M_S$  correction at all angles and ranges would be zero. Thus, the rms amplitude of the  $M_S$  correction is likely associated with gradients in the phase velocity map.

Figure 52 shows the gradient of the 20-second phase velocity map spanning the 88 source locations. The rms amplitude of the  $M_S$  correction associated with each source location is proportional to the overlaid scatter point. Source locations near Europe (source locations 16-35) are embedded in a region of the Earth with a large degree of structure and variation in phase velocity. As a consequence, the  $M_S$  corrections tend to be larger than most other source locations on the map. On the other hand, source locations in central and northern China tend to exhibit smaller  $M_S$  corrections because changes in phase velocity occur over longer distances, leading to smaller gradients.

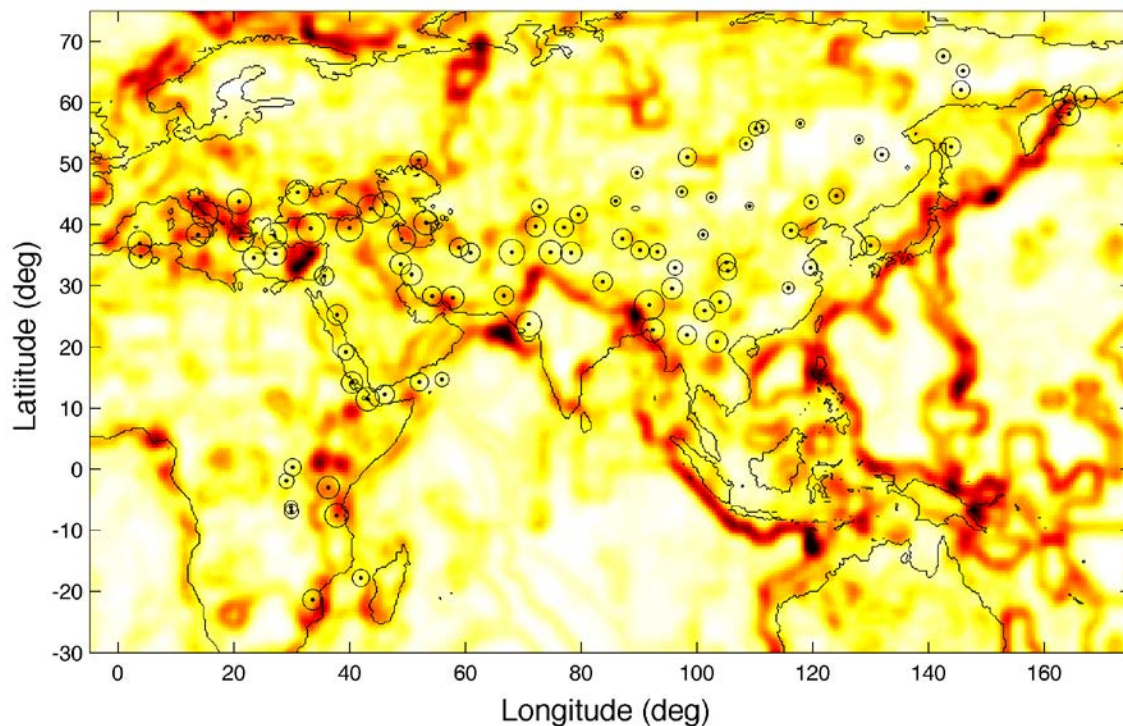


**Figure 52.** Map of the gradient of the 20-second phase velocity spanning Eurasia and most of Africa and Australia. *The overlaid scatter plot contains the simulated explosion source locations, with size of the scatter points proportional to the angle-averaged rms  $M_S$  corrections corresponding to the source location.*

In addition to studying the amplitude of  $M_S$  corrections, it is clearly important to more fully understand the effects of phase velocity uncertainty on our results. For example, when the uncertainty in the  $M_S$  correction (i.e., standard deviation over the ensemble) becomes as large as the magnitude of the correction, 16% of the corrections are of the wrong sign. In other words, when uncertainty is of the same magnitude as the correction itself, applying a  $M_S$  correction will

actually make the surface wave magnitude estimate *worse* than assuming uniform Earth structure in 16% of cases.

Figure 53 shows a comparison of the rms amplitude of  $M_S$  corrections to the uncertainty in the corrections, averaged over the 88 source locations. Because the curves intersect at about 2000 km, we conclude that with uncertainty in the phase velocity of 2-3%, the validity of the “dandelion” plots is out to a range of ~2000 km. Beyond this range, the magnitude of the corrections become comparable to standard deviation over an ensemble of possible true phase velocities.

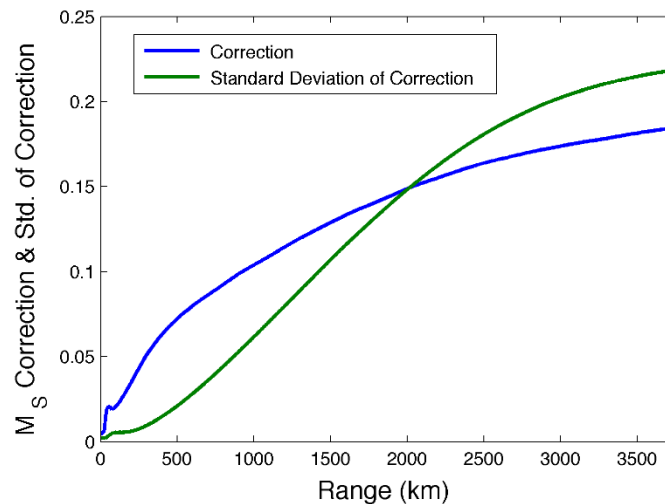


**Figure 53. Blue curve: Root-mean-squared magnitude of the  $M_S$  corrections (dB), averaged over all angles and source locations, as a function of range. Green curve: Average uncertainty in the  $M_S$  corrections, estimated from the standard deviation of the  $M_S$  corrections over an ensemble of 25 trials for each source location.**



### 4.7.2 Comparison of Data and Model Variability in Eurasia

The membrane calculation is an efficient way to model surface-wave propagation in a realistically heterogeneous earth model. Based on the comparisons with finite difference calculations it can reproduce much of the complex amplitude behavior arising from diffraction and multi-pathing. As shown in the study of observations in the western USA, the method predicts amplitude variation on the order of what is observed. However, many factors contribute to the observed amplitudes and it is difficult to isolate each one such that we can sufficiently improve our earth model to better determine the source strength.

Figure 54 (left) shows the phase velocity model for 20 s Rayleigh waves around a source located in Kyrgyzstan. Figure 54 (right) shows the log of ratio of the maximum amplitude of membrane waves propagating in that heterogeneous model to the maximum amplitude of membrane waves propagating in a uniform (homogeneous average) model. Both membrane calculations are for an explosion source to eliminate any effects from radiation pattern. The membrane calculation predicts narrow regions of enhanced and reduced amplitudes with peak-to-peak variations of nearly a magnitude unit. These variations occur over small changes in azimuth.

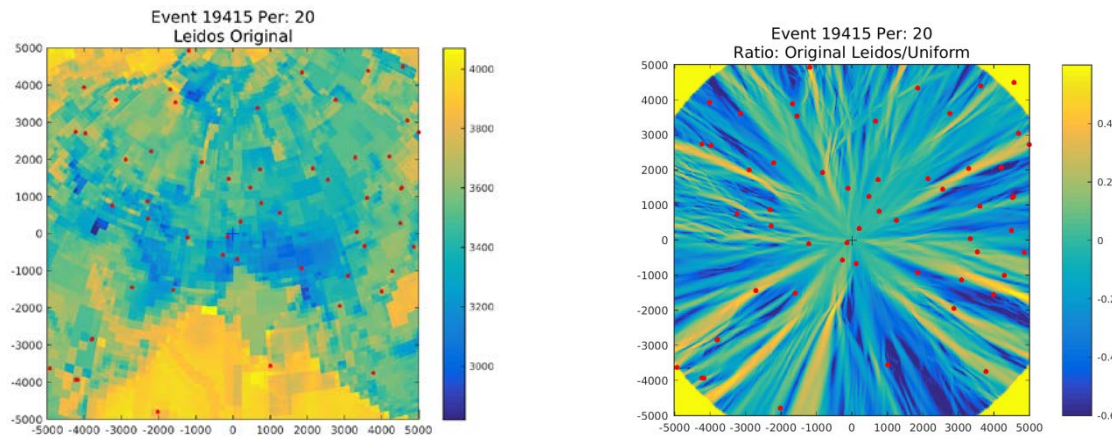


**Figure 54. Left: Map of 20-s Rayleigh wave phase velocity around a source located in Kyrgyzstan. The model is the Leidos model, Stevens et al. (2008). Right: log of the amplitude ratio of the maximum amplitude of the membrane waves computed for an explosion source and the model shown in (a) to the maximum amplitude of the membrane waves computed for an averaged, uniform model. Note the predicted fine structure of strong variation in amplitudes predicted for the Leidos model.**

One contributor to the variation in the calculated amplitudes is the roughness of the phase-velocity model, which in some cases is caused by unrealistic boundaries between grid cells. We learned in our earlier work in the western USA that smoother models reduce the small-scale variation in amplitudes, although the smaller source-receiver distances in that study further reduced the overall amplitude variations. To assess the effects of roughness, we smooth the model and recalculate surface waves. In Figure 55, we derive a smoothed phase-velocity model from the model in Figure 54 and repeat the calculation. As we expected, the smoothed model does reduce the small-scale variation. However the relatively narrow regions of strong amplification persist and the amount of variation is still considerable.



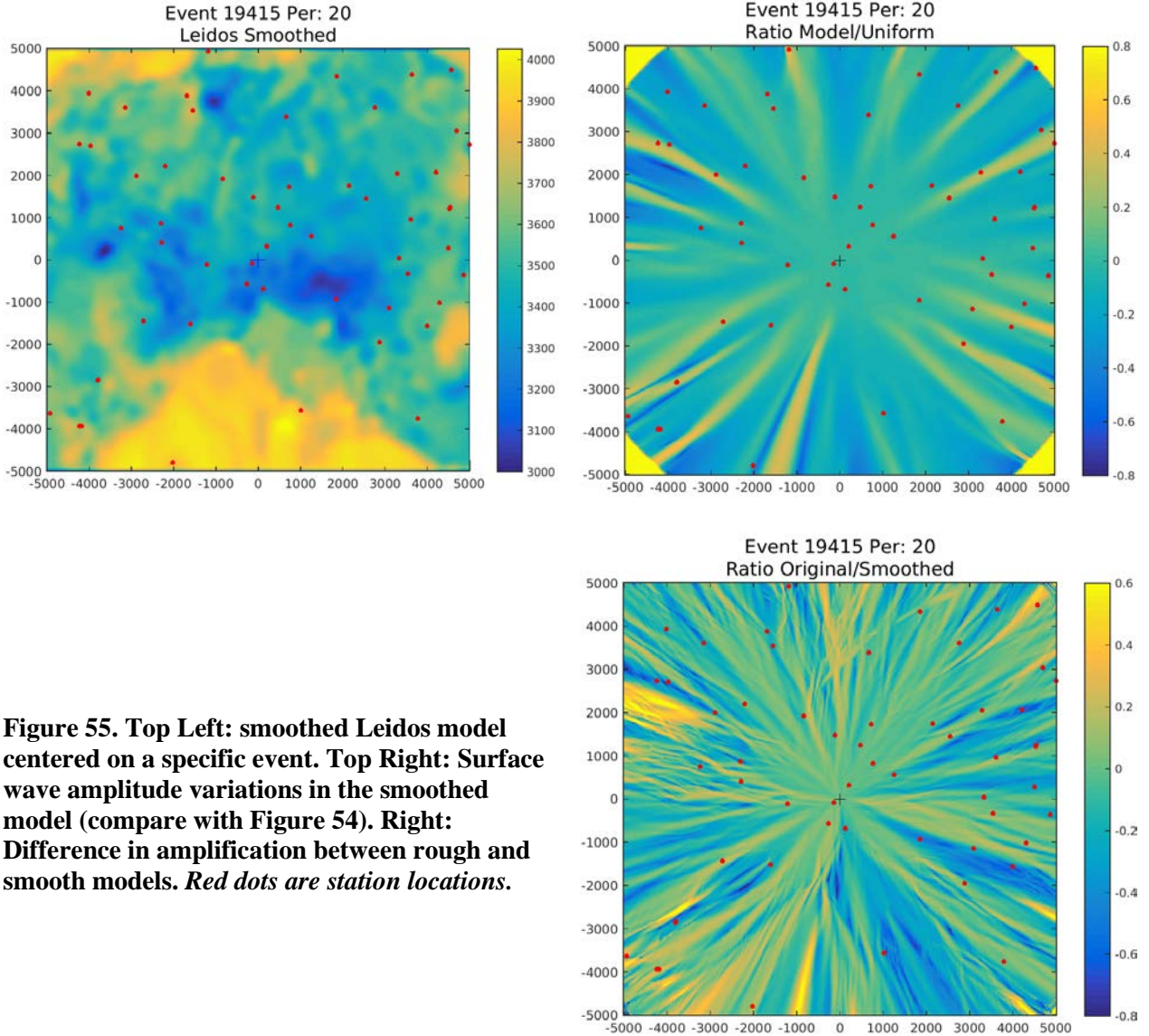


**Figure 55. Top Left: smoothed Leidos model centered on a specific event. Top Right: Surface wave amplitude variations in the smoothed model (compare with Figure 54). Right: Difference in amplification between rough and smooth models. Red dots are station locations.**

Comparing the previous figures, it appears that the dominant regions of amplification/reduction persist. However, the details vary considerably. Also shown in Figure 55 is a comparison of the two models, taking the difference between the initial rougher model and the smoothed model. The rougher model clearly shows much larger variability as expected, but it is also clear that the regions of extreme amplitude variation have also slightly relocated. The predicted amplitude features from similar models predict an amplification pattern that is grossly similar, but that is very different in the details, details directly related to our observational capability.

The kernels used in the Born approximation illustrate, at least qualitatively the issues involved. The kernels for phase delay – i.e., travel time – show that a predicted phase advance at a station is directly correlated with an increase in phase velocity along the path from the source, as one would expect from simple geometry. There are some regions of negative correlation (i.e. the negative side lobes modeled in an earlier section) in which the phase is advanced by a decrease in phase-velocity but these regions are relatively inconsequential. On the other hand the Born amplitude

kernels are narrower with deep symmetric side lobes and show clear sensitivity to the variation, or roughness, of the earth model, perpendicular to the wave propagation path. The tomographic procedure is insensitive to this structure on the necessary scale, so it is not surprising that earth models derived from phase and group delays, and even those incorporating attenuation may not predict the observed amplitude variations.

Figure 56 shows how magnitude differences (more precisely, the log spectral amplitude ratios shown above in Figure 54), vary with distance for the initial and smoothed phase-velocity models for three different events in Eurasia. For each model, the mean and standard deviation of the amplitude ratios are shown for annuli 1000 km wide between 1000 and 5000 km from the source. At 20 s, there is about a 0.1 reduction in standard deviation between the initial Leidos model (e.g., Figure 54) and the smoothed model (e.g. Figure 55). There is some variation with source region and it is more pronounced with the initial Leidos model.

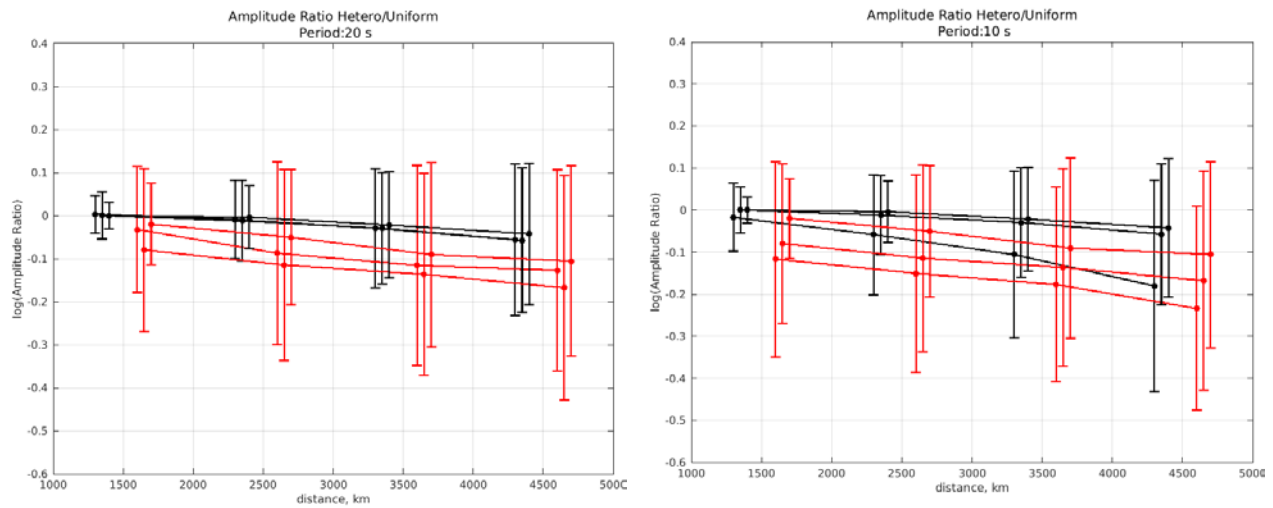


**Figure 56. Log amplitude ratio with numerator the amplitude of an explosion source propagated using the membrane calculation with velocity taken from the Leidos Eurasian earth model and the denominator the amplitude of an explosion source propagated on a uniform membrane. The black symbols are for the smoothed Leidos model; the red symbols are for the unaltered Leidos model. The points represent averages in 1000 km annuli from 1000 to 5000 km and surrounding each of three source locations. Left: 20 s period. Right: 10 s period.**

As expected, the smoothed model reduces the variance in the magnitude measures compared to those from the initial model. It is then of interest to see how well the variance compares with that from actual magnitude measurements.

As described earlier in the report we have measured amplitudes for a large number of Eurasian events using data carefully selected for quality. Of the initial set of over 1600 events, 500 were selected to have enough observational data to make a reasonable estimate of network magnitude. We consider three cases: (1) path equalized amplitudes using path-dependent attenuation resulting from the inversion described above; (2)  $M_S(VMAX)$  magnitudes using the amplitudes from (1) and corrected according to the formula from Russell (2006), and (3)  $M_S(VMAX)$  magnitudes measured from path-equalized synthetics, which include the effects of the radiation pattern of the event. In each case we measure amplitudes in the time-domain using narrow-band Butterworth filters according to the  $M_S(VMAX)$  procedure from Russell. Despite the quality-control screening we applied, there remain observations that appear to be large outliers, much larger than anything

predicted above. To reduce the influence of these measurements we calculate the network magnitude for each event using the median. The standard deviation is then approximated by the median absolute deviation, or MAD, between each observation and its associated network magnitude. Figure 57 shows how the magnitude measures vary with distance with the measurements partitioned as described in Figure 56. The MAD is corrected to be a proxy for the standard deviation, so the vertical axes are directly comparable. The synthetic case shows how the source radiation pattern affects the variation of the magnitude measurements. The radiation pattern is significant but is not obviously the dominant contribution. Note also for this data set, the corrections used to compute  $M_S(VMAX)$  appear to under correct the magnitude at distance ranges less than 2000km. The higher attenuation derived from the Q inversion discussed earlier provides a better distance correction.

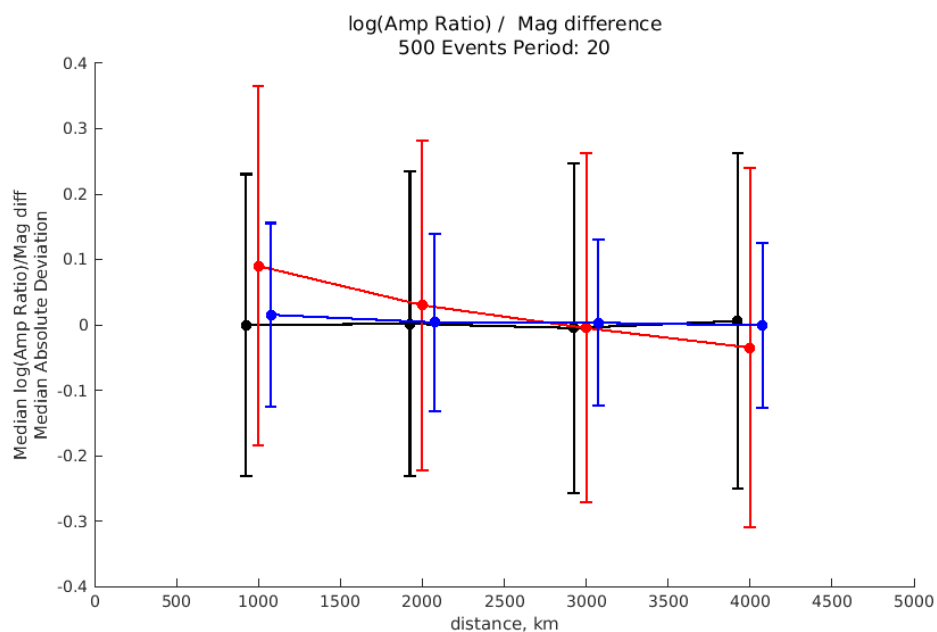


**Figure 57.** Variation of magnitude measurements relative to their associated network averaged magnitude. *Distance bins are 1000 km wide from 1000 to 5000 km. Black symbols are path equalized, attenuation corrected amplitudes. Red are magnitudes corrected using the correction formula in Russell, 2006. Blue symbols are for path equalized synthetic data, which removes everything but the radiation pattern.*

## 5. Conclusions

The main tasks of this project are:

1. Development and testing of a membrane surface wave code (SurfMembrane)
2. Collection of US Array data and earth models in the area covered by the US Array to test the membrane surface wave technique in an area with dense coverage and well-developed earth models.
3. Collection of Eurasian and North African surface wave data and earth models.
4. Inversion of Eurasian and North African surface wave data for  $Q$  and development of path dependent attenuation maps.

All of these tasks have been completed. SurfMembrane was developed during year 1, and during year 2 it was improved and the capability to calculate finite frequency kernels was added. SurfMembrane 3.0 is being delivered together with this report. The data sets of both US Array data and Eurasian/African data were retrieved from IRIS. Centroid Moment Tensor (CMT) solutions were found for as many events as possible during the time period of interest, and locations and depths were updated with ISC solutions for the same events.

We inverted a large Eurasian and northern African data set for  $Q$  structure. The data set retrieved from IRIS consisted of 59,000 waveforms from 1850 Eurasian and African earthquakes, all with CMT solutions. These were added to the smaller data set used in the Stevens et al (2008) study. Both the new and the old data sets were subjected to an intensive quality control procedure to remove bad or questionable data, deep events and events with inaccurate CMT solutions. The final data set contained 23,148 waveforms from 998 events. Inversion results are similar to the 2008 study and cover a larger region of Eurasia. There is a band of high attenuation stretching across the Middle East from the Mediterranean Sea to India.

To validate SurfMembrane, calculations were compared with the results of a 3D finite difference calculation corresponding to the complex region between Lop Nor and KNET (Stevens et al, 2008). SurfMembrane was run for each frequency and compared with results from the 3D calculation filtered in approximately the same frequency band. The SurfMembrane corrections significantly improved the consistency of the results, which shows that if the source and structure are well-defined, SurfMembrane can be used to generate structural amplitude corrections.

We ran SurfMembrane for 73 events with CMT solutions within the US Array and compared calculated and observed amplitude variations. This was less successful for two reasons: 1) the structure is not known exactly; 2) radiation pattern effects were strong enough to dominate over the structural variations. Because radiation pattern effects are so strong, small errors in the CMT solution swamp the variations due to the structural effects that we are trying to model. Although the SurfMembrane corrections derived with an explosion source had a small positive effect, the improvement is not very significant.

We applied SurfMembrane to events in the Eurasian/North African region. Although the data density is not as high as for the US Array, the paths are much longer and so both structural effects and anelastic attenuation are considerably larger. We ran SurfMembrane calculations for 88 well-distributed earthquakes from the Eurasian data set and compared the results with data. We find that the SurfMembrane calculations can be used to correct  $M_s$  for diffraction out to distances of about 2000 km, however at greater distances diffraction is too sensitive to small variations in earth

structure to allow reliable predictions for typical variations and uncertainties in phase velocity maps.

A large contributor to the observed amplitude variation in the surface waves is the ‘roughness’ in the spatial variation of the earth model. The scatter in the observed amplitudes, or equivalently, magnitude corrections, can, therefore, help us specify smoothness constraints on our earth models, which is an input to the tomographic inversion. The overall scatter we observe in the magnitudes is consistent with predictions based on the spatial variation seen in the Leidos 1-degree earth model and smoother models predict much smaller amplitude scatter, especially at the nearer distances. But there remains substantial uncertainty in how radiation pattern is affecting the scatter, even with CMT solutions. Careful study of multiple nearby events using joint inversion methods would help further isolate the effect of propagation and provide a more realistic estimate of the scatter in amplitudes due to propagation effects. For example, the relative homogeneity of the Leidos model for large areas of Asia as manifest in Figure 52 predicts that scatter in amplitudes due to propagation should be relatively small in this region. Further study including the effects of the source could verify this prediction. The SurfMembrane approach provides an efficient way to incorporate amplitude constraints into inversion studies and make realistic predictions from the results.

## References

- Chen, P., T. H. Jordan, and L. Zhao (2007), "Full three-dimensional tomography: a comparison between the scattering-integral and adjoint-wavefield methods," *Geophys. J. Int.*, **170**, pp. 175-181.
- Clayton, R. and B. Engquist (1977), "Absorbing boundary conditions for acoustic and elastic wave equations," *Bull. Seism. Soc. of Am.* **67**, No. 6, pp. 1529-1540.
- Harkrider, D. G., J. L. Stevens, and C. B. Archambeau (1994), "Theoretical Rayleigh and Love Waves from an explosion in prestressed source regions," *Bull. Seism. Soc. Am.*, v. **84**, No. 5, pp 1410-1442.
- Lou, Xiaoting and Suzan van der Lee (2014), "Observed and predicted North American teleseismic delay times," *Earth and Planetary Science Letters*, **402**, pp. 6-15, doi:10.1016/j.epsl.2013.11.056.
- Nolet, G. (1987), "Seismic Wave Propagation and Seismic Tomography," in *Seismic Tomography with Applications In Global Seismology and Exploration Geophysics*, G. Nolet, ed., D. Reidel Publishing, Dordrecht, Holland.
- Peter, D., C. Tape, L. Boschi, and J. H. Woodhouse, (2007), "Surface wave tomography: global membrane waves and adjoint methods," *Geophys. J. Int.*, **171**, p. 1098-1117.
- Russell, D.R., (2006), "Development of a time-domain, variable-period surface wave magnitude measurement procedure for application at regional and teleseismic distances. Part I—Theory," *Bull. Seism. Soc. Am.*, 96, pp. 665-677.
- Shen, W., M. H. Ritzwoller, and V. Schulte-Pelkum (2013), "A 3-D model of the crust and uppermost mantle beneath the central and western US by joint inversion of receiver functions and surface wave dispersion," *J. Geophys. Res.*, doi:10.1029/2012JB009602, **118**, pp. 1-15.
- Stevens, J. L., D. A. Adams, G. E. Baker, M. G. Eneva, and H. Xu (2005), "Improved Surface Wave Dispersion Models, Amplitude Measurements and Azimuth Estimates," SAIC Final Report submitted to AFRL under contract DTRA01-01-C-0082, March.
- Stevens, Jeffry L., Heming Xu, Jeffrey W. Given, and G. Eli Baker (2008), "Development of Surface Wave Dispersion and Attenuation Maps and Improved Methods for Measuring Surface Waves," AFRL-RV-HA-TR-2008-1106, Science Applications International Corporation, San Diego, CA, May.
- Tanimoto, T. (1990), "Modelling curved surface wave paths: membrane surface wave synthetics," *Geophys. J. Int.*, V. **102**, pp 89-100. <http://dx.doi.org/10.1111/j.1365-246X.1990.tb00532.x>.
- Tape, C. H. (2003), "Waves on a spherical membrane," Thesis submitted to the University of Oxford for the Degree of Master of Science by Research.
- Tape, Carl, Qinya Liu, and Jeroen Tromp (2007), "Finite-frequency tomography using adjoint methods—Methodology and examples using membrane surface waves," *Geophys. J. Int.* **168**, pp. 1105-1129 doi: 10.1111/j.1365-246X.2006.03191.x.
- Tromp, J., C. Tape and Q. Liu (2005), "Seismic tomography, adjoint methods, time reversal and banana-doughnut kernels," *Geophys. J. Int.*, 160, pp. 195-216.

## **Appendix A. SurfMembrane Description and User Manual**

### **List of Figures**

Figure A-1. Default forcing function.....	59
Figure A-2. 10 second phase velocity map used in KNET calculation.....	60
Figure A-3. Snapshot of velocity from KNET calculation at 240 seconds.....	61

## Appendix A. SurfMembrane Description and User Manual

### A.1 Input to SurfMembrane

SurfMembrane is written in Fortran 95 with some Fortran 2003 extensions. Input to the membrane surface wave code is in Fortran namelist format using a namelist “MEM\_IN”. The code is executed with the command:

*SurfMembrane NamelistFilename*

where NamelistFilename is the name of a file containing the input namelist.

An example input file is given below for the Lop Nor to KNET calculation at 10 seconds period.

```
&MEM_IN
nx = 678
ny = 858
dx = 2000.
nt = 5000
dt = 0.20
printcycle = 5
idrive = 302
jdrive = 750
drive_type = 2
drivefilename = 'drive/evl.10.drv'
cvelfilename = 'cvel/KNET.10'
outfilename = 'outfile/KNET.10.dat'
stalocfilename = 'staloc/stalist'
stadatafilename = 'outfile/evl.10.stadata'
/
```

#### Definitions:

```
nx = number of points in the X direction
ny = number of points in the Y direction
dx = spacing between points (X and Y spacing is the same)
nt = number of time steps to run
dt = time step (Courant condition applies, must be < 0.7 *
    minimum travel time across a zone. 0.5 recommended)
printcycle = increment between print cycles. 5 will print cycles
    5, 10, 15 ...
idrive = X node location of drive
jdrive = Y node location of drive
drive_type = 0 No drive
             1 Not currently implemented
             2 Specified fixed velocity
             3 Specified velocity added to calculated velocity
drivefilename = drive file name. See Appendix for format
cvelfilename = phase velocity map file name. See Appendix for
    format
outfilename = output filename. See Appendix for format
stalocfilename = station location filename (saved every cycle).
    See Appendix for format
```



stadatafilename = output station time series. See Appendix for format.

**Other namelist parameters not used in the example above, with default values:**

cvel\_in = 1.0. Constant phase velocity value used if cvelfilename is not input.  
 initstatefilename = none. Specify initial wavefield in grid.  
 force\_type = 0. No forcing function  
               = 1. Calculated Gaussian forcing function  
               = 2. Specified forcing function  
 forcefilename = none. Forcing function filename. See Appendix for format.  
 printspacing = 1. Spacing between points on output file (3 means every third point is printed).  
 reverse\_force = 0. If positive, time reverse the input force (used for adjoint calculations).  
 isrc = 0. X location of forcing function  
 jsrc = 0. Y location of forcing function  
 Forcing function variables (see below)  
     tau = 20.0  
     tau0 = 2.628  
     tstart = 48.  
 input\_only = 0. If positive, print out input, and then stop without running the calculation.

The calculated forcing function is illustrated in Figure A-1 and defined by:

$$\alpha = \frac{2\tau_0}{\tau}$$

$$A = \frac{-2\alpha^3}{\sqrt{\pi}}$$

$$t = \text{time} - tstart$$

$$F(t) = At^2 \exp\left(-(\alpha t)^2\right)$$

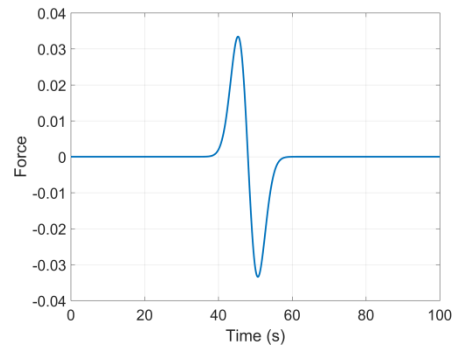


**Figure A-1. Default forcing function.**

**Input variables for calculation of sensitivity kernels:**

kernel\_from\_stadata = 0. If positive, calculate kernel from stadata file.  
 kernelfilename = 'none'. Output kernel file.  
 sourcememfilename = 'none'. Input file, results of previous membrane calculation. Not needed if kernel\_from\_stadata>0. In that case outfilename is used as input for kernel calc.

## A.2 SurfMembrane File Formats

In this appendix we describe the formats needed for reading and writing the files used by SurfMembrane. Error checking in the open and read/write statements has been removed for clarity. In the examples in this appendix, the X axis has been chosen to be north and the Y axis east, because these were the coordinates used in the earlier 3D KNET calculation. This is not a requirement and X and Y can be chosen to be east and north as long as coordinates are consistent in all input files. Note that data on binary files are stored in column order, so all rows are read sequentially by column for each matrix.

### A.2.1 Phase Velocity File (input) `cvelfilename`. Fortran direct access binary file.

Opened with:

```
open(VELFILE,file=cvelfilename,form='unformatted',access='direct',status='old',recl=nx*ny*4)
```

Read with:

```
read(VELFILE,rec=1) cvel(1:nx,1:ny)
```

The image in Figure A-2 was made with the following Matlab commands:

```
FILE=fopen(cvelfilename,'r');  
cvel=fread(FILE,[nx ny],'float32');  
fclose(FILE);  
imagesc(y,x,cvel);  
axis equal; set(gca,'Ydir','Normal');
```

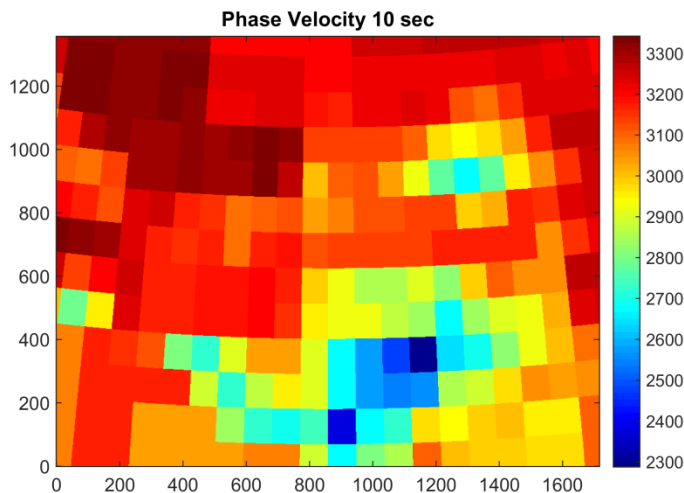


**Figure A-2. 10 second phase velocity map used in KNET calculation.**

### A.2.2 Output File outfile (output). Fortran direct access binary file.

Opened with:

```
open(OUTFILE,file=outfilename,form='unformatted',access='direct',status='replace',  
      recl=( nx+2)*(ny+2)*4 )
```

Note that one additional row and column are added to each of the sides, top and bottom, so the dimensions of the output file are nx+2 and ny+2 instead of nx,ny

Written with (in time loop):

```
if( mod(it,printcycle) == 0) then  
  write(OUTFILE,rec=it/printcycle) ut(0:nx+1,0:ny+1)  
endif
```

The image in Figure A-3 was made with the following Matlab commands, where nt was chosen to be the number of saved states corresponding to 240 seconds.

```
xx=0:2:nx*2;  
yy=0:2:ny*2;  
for i=1:nt  
  Z=fread(FILE,[nx+2 ny+2], 'float32');  
end  
xs=302;ys=750; %Source location  
Z(xs-4:xs+6,ys-4:ys+6)=0; %Blank out source region  
imagesc(yy,xx,Z);  
axis equal;colorbar;  
set(gca,'Ydir','Normal');
```

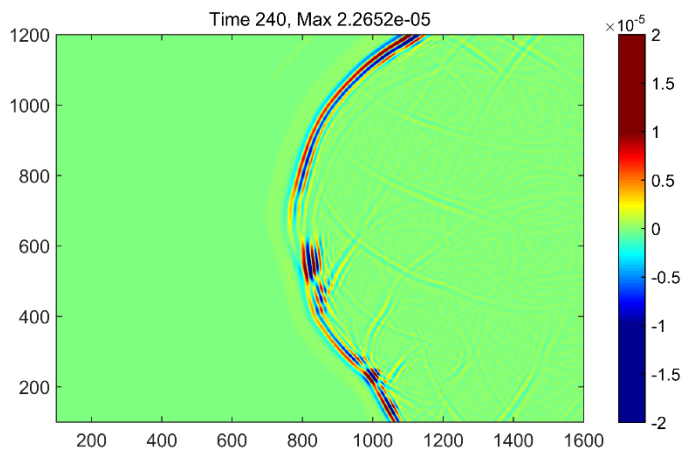


**Figure A-3. Snapshot of velocity from KNET calculation at 240 seconds.**

### **A.2.3 Station Location File (input) stalocfilename. Ascii file.**

Opened with:

```
open(STALOCFILE,file=stalocfilename,form='formatted',status='old')
```

Read with:

```
read(STALOCFILE,*,iostat=ios,iomsg=message) nstation
do ista=1,nstation
    read(STALOCFILE,*) istation(ista),jstation(ista)
end
```

Here is an example of a station location file from the KNET run:

```
14
302 700
302 650
302 600
302 550
302 500
302 450
302 400
302 350
302 300
302 250
302 200
302 150
302 100
302 50
```

#### **A.2.4 Station Data File (output) stadatafilename. Ascii file.**

Opened with:

```
open(STADATAFILE,file=stadatafilename,form='formatted',status='replace')
```

Written with (in time loop, nstation columns in es15.5 format):

```
write(formatstring,'(a1,i2,a)', '(' ,nstation,'es13.5')  
write(STADATAFILE,formatstring) (ut(istation(ista),jstation(ista)),ista=1,nstation)
```

### **A.2.5 Initial State File (input) initstatefilename. Fortran direct access binary file.**

Opened with:

```
open(INITSTATEFILE,file=initstatefilename,form='unformatted',access='direct',status='old',recl=nx*ny*4)
```

Read with:

```
read(INFILE,rec=1) ut(1:nx,1:ny)
```

### **A.2.6 Drive File (input) drivefilename. Ascii file.**

Opened with:

```
open(DFILE,file=filename,form='formatted',status='old')
```

Read with:

```
read(DFILE,*) nxydrive,ntdrive
read(DFILE,*) (tdrive(itdrive),itdrive=1,ntdrive)
do ixydrive=1,nxydrive
  read(DFILE,*) ixdrive(ixydrive),iydrive(ixydrive)
  read(DFILE,*) (drive(itdrive,ixydrive),itdrive=1,ntdrive)
end do
```

### **A.2.7 Forcing File (input) forcefilename. Ascii file**

Opened with:

```
open(FFILE,file=filename,form='formatted',status='old')
```

Read with:

```
read(FFILE,*,iostat=ios,iomsg=message) nforce
do iforce=1,nforce
    read(FFILE,*,iostat=ios,iomsg=message) tforce(iforce),fforce(iforce)
end do
```



### **A.2.8 Sensitivity Kernel (output) File Format**

Opened with:

```
open(KRNFILE,file=kernelfilename,form='unformatted',access='direct',status='replace',  
      recl=(nx+2)*(ny+2)*4, iostat=ios,iomsg=message)
```

Written with:

```
do ista = 1,nstation  
    write(KRNFILE,rec=ista,iostat=ios,iomsg=message) kernelFinal(0:nx+1,0:ny+1)  
end do
```

## Appendix B. SurfMembrane Code and Data Deliverable

### List of Figures

Figure B-1. Phase velocity maps for test case. ....	71
Figure B-2. Drive functions. ....	72
Figure B-3. Spatial plot of velocity at 150 seconds. ....	73
Figure B-4. Waveforms at station #420 (location 854, 271 in the grid).....	74
Figure B-5. Surface wave amplification for heterogeneous relative to uniform structures.....	75

## Appendix B. SurfMembrane Code and Data Deliverable

### B.1 Data Deliverable

The source code, sample results and test data are all included in the file SurfMembrane\_2017-05.tgz which is distributed with this report. To run the test case, untar the file into the desired installation directory and follow the instructions in the README file. The procedure is summarized below:

1. Modify the global Makefiles to have the correct paths to compilers installed on the system (see README for details).
2. Run “make” to compile SurfMembrane. The resulting executable will be src/SurfMembrane.
3. Run “make test” to run the test cases.
4. To make plots, open Matlab from the installation directory, <distdir>, and enter:  

```
addpath <distdir>/matlab  
addpath <distdir>/test/matlab  
cd <distdir>/test  
plot_examples
```
5. This will make a set of png files in directory test/plots that should replicate one-for-one plots in test/refplots. There may be small differences due to differences in fonts on different systems.
6. You can also run movies of the calculation using “plot\_example\_membrane\_movies”.

## B.2 MATLAB Scripts

Several MATLAB functions are provided to simplify data access and to make plots of calculation results. These are summarized below. Do a “help” on the matlab directory after installation for details.

**get\_max\_membrane:** Retrieve maximum amplitudes and amplification for heterogeneous and homogenous membrane calculations.

```
[seis_max,seisuni_max,seisamp]= get_max_membrane(memfile,memfileuni,nx,ny,nt,dt,fc,delf)
```

**get\_membrane:** Retrieve 3D (x,y,time) array of data from membrane calculation.

```
memdata=get_membrane(memfile,nx,ny,nt,tlim)
```

**get\_stadata:** Retrieve all calculated station data from a membrane calculation.

```
[stadata,nsta,nt]=get_stadata(stadatafile,dt,fc,delf)
```

**plot\_drive:** Plot source drive functions.

```
[h,hax] = plot_drive(drivefilename,plotindividual)
```

**plot\_membrane:** Plot images of spatial data retrieved by get\_membrane or get\_max\_membrane.

```
[h,hax] = plot_membrane(memdata,dxy,clim,tpause,tlim,titletext)
```

**plot\_stadata:** Plot calculated time series for an individual station.

```
[h,hax] = plot_stadata(stadata,ista,dt)
```

**plot\_phasevel:** Plot phase velocity map

```
[h,hax] = plot_phasevel(velfile,nx,ny,dxy,xyorigin,axlim,clim)
```

### B.3 Test Case

A Test Case is provided that includes calculations at 10 and 20 seconds for an explosion at 0.5 km depth in two earth structures, corresponding to a source location in northeastern Nevada at latitude 41.150 and longitude -114.870. This is the location of one of the earthquakes (event 17) in the US Array study, and the test case is for an explosion at the same coordinates with receivers at the same US Array locations. Several Matlab scripts are provided to make plots from the test case. See section B.1 for instructions on running the test case.

The Matlab script “plot\_example\_phasevel” plots the phase velocity maps used in the calculation. These are shown in Figure B-1.

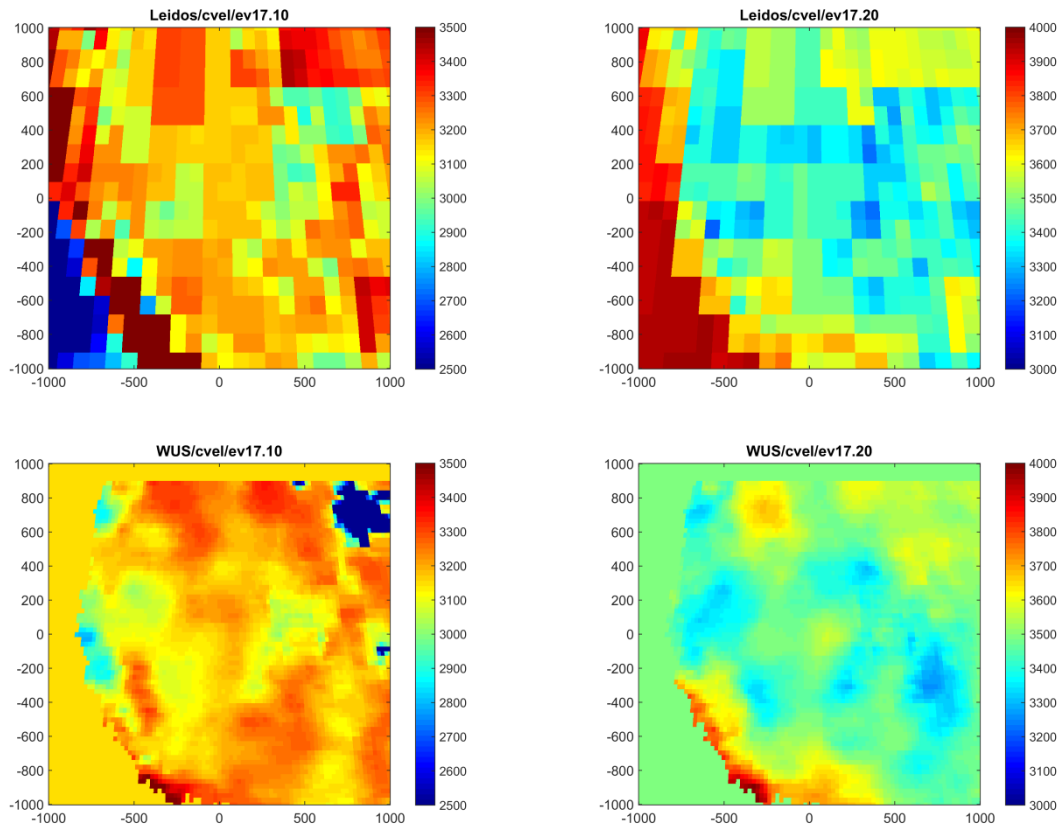


**Figure B-1. Phase velocity maps for test case. Top row Leidos structures, bottom row WUS structures. Left column 10 seconds, right column 20 seconds.**

The Matlab script “plot\_example\_drives” plots the applied source functions. These are shown in Figure B-2. Each figure has 40 curves and although they appear to be nearly the same, the small amount of phase and amplitude difference between the curves is important. Also, notice that the source function amplitudes of the two structures are different, corresponding to the difference in surface wave excitation function for each structure. These functions correspond to the vertical velocity of the fundamental mode surface wave calculated on a closed surface around the origin.

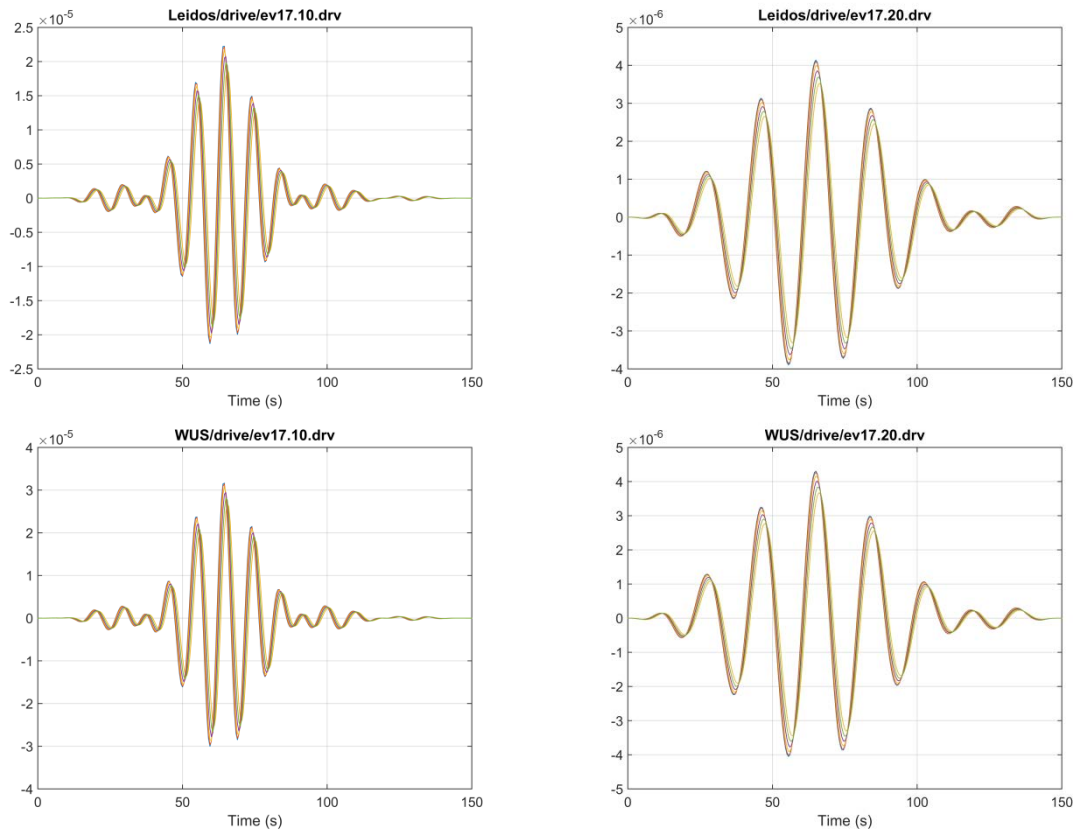


**Figure B-2. Drive functions. Top row Leidos structures, bottom row WUS structures. Left column 10 seconds, right column 20 seconds.**

The script “plot\_example\_membrane” plots the propagation on the grid. The script first runs a movie of each calculation and then makes a plot at 150 seconds. These are shown in Figure B-3.

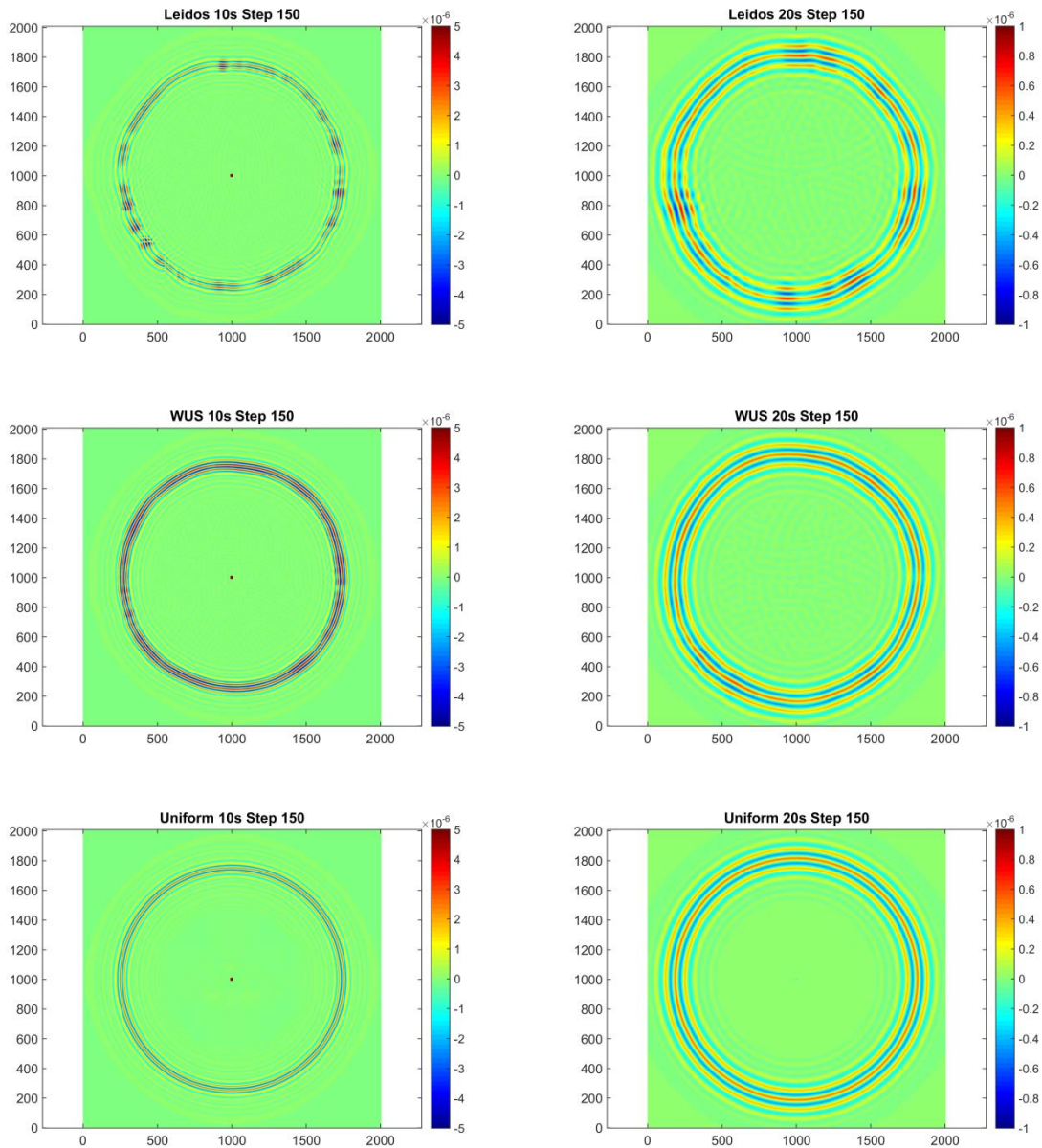


**Figure B-3. Spatial plot of velocity at 150 seconds. Top row Leidos structures, middle row WUS structures, bottom row uniform structures. Left column: 10 seconds, right column 20 seconds.**

The script `plot_example_stations` plots waveforms at selected stations. Note that while the full grid is only saved every 10 time steps (2.0 second intervals), the station data is saved for every time step (0.2 seconds), so the station data has higher time resolution. The plots made by this script are shown in Figure B-4.

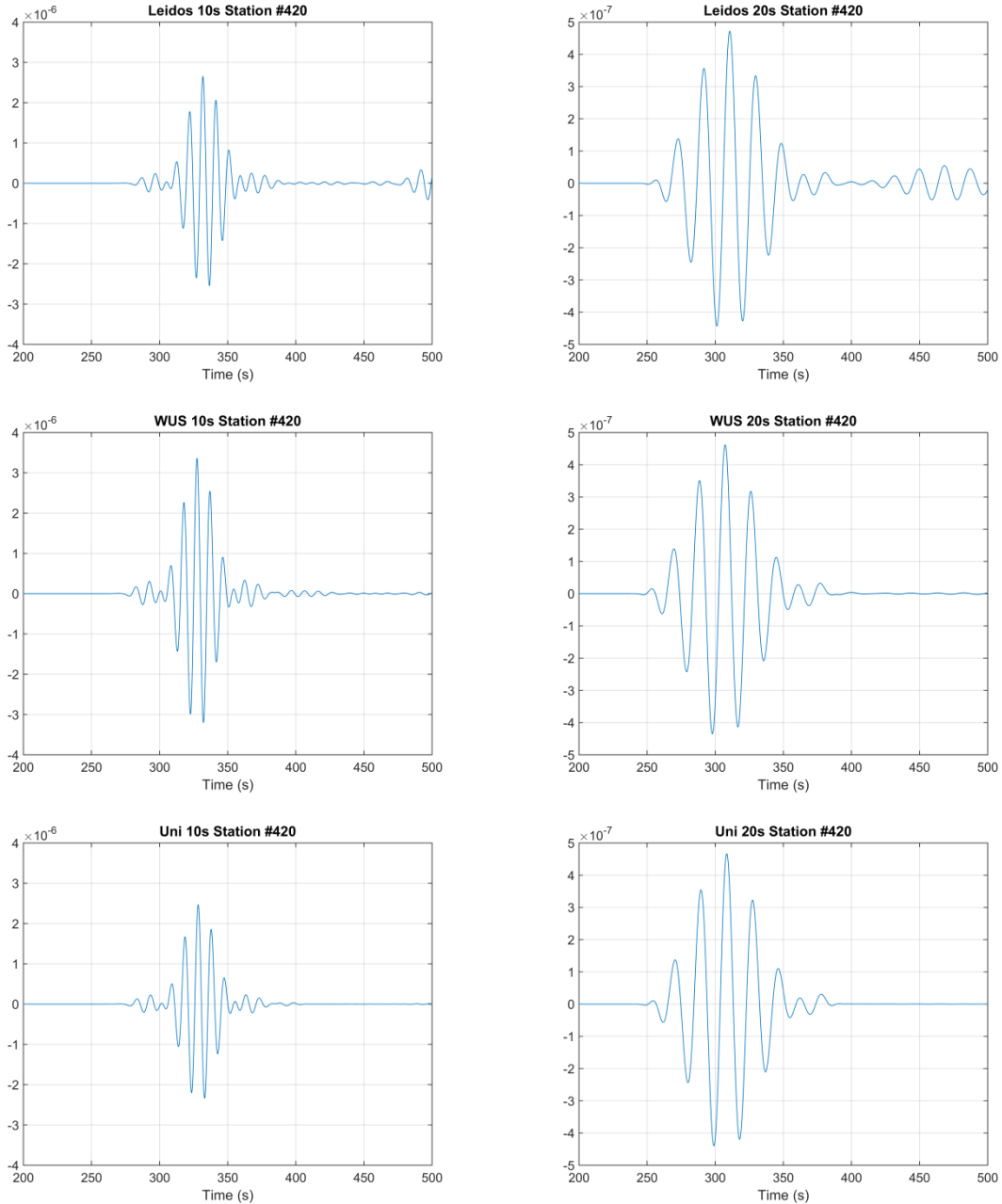


**Figure B-4. Waveforms at station #420 (location 854, 271 in the grid). Top row: *Leidos* structures, middle row: *WUS* structures, bottom row: *uniform* structures. Left: 10 seconds, right: 20 seconds.**



The Matlab script “plot\_example\_membrane\_amp” plots the spatial distribution of amplification (or deamplification) caused by propagation through the earth structures. The plots made by this script are shown in Figure B-5.

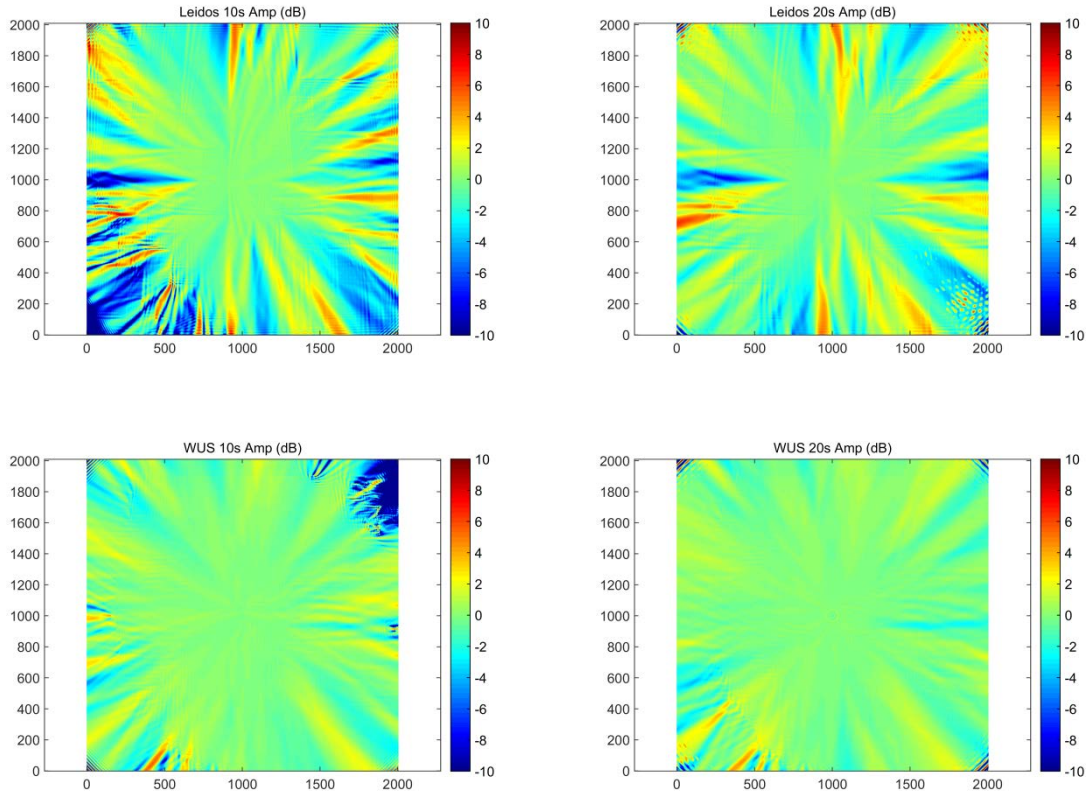


**Figure B-5. Surface wave amplification for heterogeneous relative to uniform structures. Top row: Leidos structures, bottom row WUS structures. Left: 10 seconds, right: 20 seconds. Amplification is in dB.**

## Appendix C. Surface Wave Q Inversion Data Deliverable

This final report is accompanied by a data deliverable consisting of the following files:

**LP\_2017\_May.tar.gz:** This is the complete set of global earth, dispersion and attenuation models. The contents are described in the file “README.models.” It also contains a program compiled under Linux to calculate the dispersion and attenuation between any two points at an input frequency.

**gamma\_data\_new:** These are all of the attenuation measurements used by Leidos during this project. The format of the file is given in the file “dataformat”.

**moments.txt:** This file gives the adjustments to CMT moments found during the Q inversion process as described in Section 4.6 of the report. The columns correspond to event number, natural log of the correction, and value of the correction.

The data given in the datafile are the original measurements derived using CMT moments and should be adjusted using the moment corrections by:

$$\Delta\gamma = -\Delta \ln M_0 / r$$

where r is the source to receiver distance.

## List of Symbols, Abbreviations, and Acronyms

AFRL	Air Force Research Laboratory
AFSPC	Air Force Space Command
CMT	Centroid Moment Tensor
GSN	Global Seismic Network
IRIS	Incorporated Research Institutions for Seismology
KNET	Kyrgyz Seismic Network
WUS	Western United States

## **DISTRIBUTION LIST**

DTIC/OCF	
8725 John J. Kingman Rd, Suite 0944	
Ft Belvoir, VA 22060-6218	1 cy
AFRL/RVIL	
Kirtland AFB, NM 87117-5776	1 cy
Official Record Copy	
AFRL/RVBYE/Dr. Frederick Schult	1 cy